

SECONDARY ION EMISSION FROM SINGLE MASSIVE
GOLD CLUSTER IMPACTS

A Dissertation

by

GEORGE JOSEPH HAGER

Submitted to the Office of Graduate Studies of
Texas A&M University
in partial fulfillment of the requirements for the degree of

DOCTOR OF PHILOSOPHY

May 2007

Major Subject: Chemistry

SECONDARY ION EMISSION FROM SINGLE MASSIVE
GOLD CLUSTER IMPACTS

A Dissertation

by

GEORGE JOSEPH HAGER

Submitted to the Office of Graduate Studies of
Texas A&M University
in partial fulfillment of the requirements for the degree of

DOCTOR OF PHILOSOPHY

Approved by:

Chair of Committee, Emile A. Schweikert

Committee Members, David H. Russell

Gyula Vigh

Robert C. Burghardt

Head of Department, Emile A. Schweikert

May 2007

Major Subject: Chemistry

ABSTRACT

Secondary Ion Emission from Single Massive Gold Cluster Impacts.

(May 2007)

George Joseph. Hager, B.S., Millersville University

Chair of Advisory Committee: Dr. Emile A. Schweikert

Secondary ion mass spectrometry, SIMS, is one of the most versatile surface analytical techniques. The significant parameter determining the performance of SIMS is the secondary ion yield. Atomic projectiles, traditionally used in SIMS, are an inefficient method to desorb and generate secondary ions. The use of poly-atomic projectiles, such as $(\text{CsI})_n\text{Cs}$, Au_3 , SF_5 and C_{60} , has been demonstrated to be an effective means to enhance secondary ion yields. Still larger secondary ion yields can be obtained with massive gold clusters, specifically Au_{400}^{4+} . Secondary ion yields from organic targets approach unity and are in excess of unity for selected inorganic targets. This dissertation is a first study of the secondary ion emission characteristics resulting from surface bombardment of keV Au_{400} .

The enhanced secondary ion yields from these massive clusters resulted in a need to detect isobaric secondary ions. An eight-anode detector was designed, built and implemented to study secondary ion emission resulting from massive projectile impacts. Secondary ion yield enhancements, resulting from use of the multi-anode detector, are reported along with secondary ion distributions for organic and inorganic targets.

Au-adduct ions have been observed in mass spectra resulting from organic and inorganic targets bombarded by Au₄₀₀. Data indicate that these adducts are a result of projectile/surface molecule interactions and not a product of Au implantation.

Secondary ion yields of these adducts are reported. Although these adduct ion yields are an order of magnitude lower than the non-adduct ions, we have demonstrated their potential usefulness in analytical applications, such as examining surface homogeneity.

Finally, these novel projectiles have been used to examine secondary ion emission from targets with different structural properties which have the same stoichiometry. In a comparative study, we have measured a significant difference in secondary ion emission and yields from the two systems, graphite and α -ZrP.

Au₄₀₀, at 136 keV, is effective in terms of secondary ion yield and secondary ion multiplicity enhancement. When used in the event-by-event bombardment/detection mode, the desorption volume has a diameter between 10-20 nm with an emission depth of approximately 5 nm, perturbing less than an attomole of analyte.

DEDICATION

To both
my mother and my wife
for without their love and support
this work would not have been possible

ACKNOWLEDGEMENTS

I am deeply indebted to a great number of people and would like to take this opportunity to thank those who have helped me over the last six years. My most sincere thanks go out to my mentor and advisor, Dr. Schweikert. Your patience and guidance throughout my graduate career are greatly appreciated and I am humbled to have had you as my advisor. I would also like to thank Dr. Verkhoturov for his insight and advice during my many experiments. I would also like to thank you for your many stories of other parts of the world. I found them quite interesting. Many thanks go to Dr. Guillermier for her help with so many things. I have never met a person who developed so many nicknames in such a short period of time, but none as endearing as “my friend”. Dennis James, I would like to thank you for explaining some of the finer points of elemental analysis to me and also for keeping the computers running in the lab, without which my research would have come to a screeching halt. Mike, thanks for the many conversations and the rounds of golf we shared. Too bad we never had the chance for you, Rick, Jay and myself to get together for a foursome. That could have been a blast. Many thanks also go to Charlene; we both know that without you this place would stop in its tracks. There is so much you do around here, from ciphering Dr. Schweikert’s writing to ensuring we have what we need to get our jobs done. Also, many thanks for the conversations ranging from local history to BBQ fixin’s. Zhen, thank you for all the help you have given me over the last few years, from moving Sara (more times than either of us can count!) to your hospitality. You are a good friend and I’m lucky to have

known you. To our newbies, Veronica and Marcus, I wish you both the best of luck here in graduate school. I think you both have great things ahead of you and I'm pulling for you. Someday I may be cool enough to understand your lingo or maybe I'm just finally too old. Just remember, you are never going to learn without mistakes. When you make mistakes, try not to make them expensive ones! Dr. Locklear, thank you for the many interesting and even sometimes stimulating conversations. I actually think I learned how to decipher yes or no out of your ambiguity. It's been a pleasure, and I do truly hope you find happiness in your life. I look forward to an invitation to the wedding with whomever you are marrying. To the good Dr. "Big D" Rickman, there are so many things to thank you for, both personal and professional. I would mostly like to thank you for sharing your family with me and Sara. It is one of the best memories I will take with me from graduate school. We've learned about golf, dressing a deer, cooking brisket, where university cars can go (regardless if they should be there or not) and that one of us is always right together.

Last but by no means least, I would like to thank my favorite group member, my loving wife Sara. The strength and drive I draw from you has made this journey much more bearable and also much more enjoyable. From Sausalito to Orange and back to College Station your dedication was fantastic, and I look forward to finally having our life together. The acknowledgements would not be complete without thanking our family pets, Dutch and Zoie. For those who come after me and read this, while they are an added responsibility, dogs are a great stress reliever. Hours of play after a long day in the lab is a great way to end the day.

TABLE OF CONTENTS

	Page
ABSTRACT	iii
DEDICATION	v
ACKNOWLEDGEMENTS	vi
TABLE OF CONTENTS	viii
LIST OF FIGURES	ix
LIST OF TABLES	xiii
CHAPTER	
I INTRODUCTION	1
II SECONDARY ION EMISSION FROM keV PROJECTILE IMPACTS	7
III INSTRUMENTATION AND ELECTRONICS	18
IV MULTI-ANODE DETECTOR	36
V AU-ANALYTE ADDUCTS RESULTING FROM SINGLE MASSIVE GOLD CLUSTER IMPACTS	61
VI CHARACTERIZATION OF SURFACE STRUCTURE	82
VII CONCLUSIONS	99
REFERENCES	104
VITA	111

LIST OF FIGURES

FIGURE		Page
3-1	Schematic of the LIMS cluster time-of-flight secondary ion mass spectrometer.	19
3-2	Schematic of the Au-Si LIMS (not drawn to scale).	20
3-3	Schematic of the LIMS, lens assembly and wien filter.	21
3-4	Schematic of the field free drift region.	27
3-5	Schematic cross-section of the secondary electron MCP assembly.	32
3-6	Schematic cross-section of the secondary ion MCP assembly.	33
3-7	Signal processing schematic for the LMIS cluster SIMS instrument.	34
4-1	Multiplicity report for phenylalanine bombarded by 27 keV Au ₃ ⁺	37
4-2	Multiplicity report for phenylalanine bombarded by 136 keV Au ₄₀₀ ⁴⁺	38
4-3	Multiplicity report for CsI bombarded by 136 keV Au ₄₀₀ ⁴⁺ . (Relative error < ± 10%)	39
4-4	Diagram of the eight-anode detector. The area in black is where copper plating is located on the assembly. The white area is where the fiberglass board is exposed. The areas marked with dashed lines are where the fiberglass insulator was removed.	43
4-5	Schematic representation of the multi-anode assembly.	45
4-6	Multiplicity plot of I ⁻ and (CsI)I ⁻ of a CsI target bombarded with 34 keV Au ₅ ⁺ . (Relative error < ± 10%)	49
4-7	Multiplicity plot of I ⁻ , (CsI)I ⁻ , (CsI) ₂ I ⁻ and (CsI) ₃ I ⁻ of a CsI target bombarded with 136 keV Au ₄₀₀ ⁴⁺ . (Relative error < ± 10%)	50

FIGURE	Page
4-8	Diagram showing the three possible secondary ion angular distributions resulting from a primary ion impact: (A) trajectory resulting from phase explosion, (B) trajectory resulting from a thermal spike model and (C) trajectory resulting from a shockwave or pressure pulse model. 52
4-9	Schematic representation of the secondary ion leg of the LMIS SIMS instrument and the location and identification of each anode on the multi-anode assembly as seen from the target. 54
4-10	Total secondary ion distribution per anode of CsI. (A) is not centered, (B) is centered. 55
4-11	Diagram of the secondary ion yields (\log_{10} scale) of selected secondary ions detected on each anode as a result of vapor deposited CsI bombarded by Au ₄₀₀ with an energy of 136 keV. 56
4-12	Diagram of the secondary ion yields (linear scale) of selected secondary ions detected on each anode as a result of vapor deposited CsI bombarded by Au ₄₀₀ with an energy of 136 keV. 57
4-13	Diagram of the secondary ion yields of selected secondary ions detected on each anode as a result of vapor deposited C ₆₀ bombarded by Au ₄₀₀ with an energy of 136 keV. 58
5-1	Negative secondary ion mass spectrum of histidine utilizing (a) Au ₅ ⁺ at 34 keV and (b) Au ₄₀₀ ⁴⁺ at 136 keV as primary projectiles. .. 63
5-2	Negative secondary ion mass spectrum of glycine utilizing (a) Au ₅ ⁺ at 34 keV and (b) Au ₄₀₀ ⁴⁺ at 136 keV as primary projectiles. 64
5-3	Negative secondary ion mass spectrum of CsI utilizing 3071 Au ₄₀₀ ⁴⁺ projectiles at 136 keV. 67
5-4	Negative secondary ion mass spectrum from a 50:50 aqueous mixture of CsI and Phe under bombardment from 136 keV Au ₄₀₀ ⁴⁺ 71
5-5	Negative secondary ion mass spectrum of all secondary ions detected in coincidence with (Phe-H) ⁻ from a 50:50 aqueous mixture of CsI and Phe under bombardment from 136 keV Au ₄₀₀ ⁴⁺ 72

FIGURE		Page
5-6	Negative secondary ion mass spectrum of all secondary ions detected in coincidence with $\text{Au}(\text{Phe-H})^-$ from a 50:50 aqueous mixture of CsI and Phe under bombardment from 136 keV Au_{400}^{4+}	74
5-7	Negative secondary ion mass spectrum of a 50:50 mixture of d_8 -Phe and Phe under bombardment from 136 keV Au_{400}^{4+}	76
5-8	Negative secondary ion mass spectrum of a 50:50 mixture of d_8 -Phe and Phe under bombardment from 136 keV Au_{400}^{4+}	77
5-9	Negative secondary ion mass spectrum of all secondary ions detected in coincidence with $(\text{Phe-H})^-$ from a 50:50 mixture of d_8 -Phe and Phe under bombardment from 136 keV Au_{400}^{4+}	79
5-10	Negative secondary ion mass spectrum of all secondary ions detected in coincidence with $\text{Au}(\text{Phe-H})^-$ from a 50:50 mixture of d_8 -Phe and Phe under bombardment from 136 keV Au_{400}^{4+}	80
6-1	Negative secondary ion mass spectrum resulting from bombarding bulk graphite with 136 keV Au_{400}	85
6-2	Negative secondary ion mass spectrum resulting from bombarding AOPG with 136 keV Au_{400}	86
6-3	Negative secondary ion mass spectrum resulting from bombarding bulk graphite with 136 keV Au_{400} . Peak intensities are normalized to the number of primary projectiles.	87
6-4	Negative secondary ion mass spectrum resulting from bombarding AOPG with 136 keV Au_{400} . Peak intensities are normalized to the number of primary projectiles.	88
6-5	Negative secondary ion mass spectrum resulting from bombarding αZrP gel with 136 keV Au_{400} . Secondary ion yields for PO_2 and PO_3 are 0.33 and 0.64 respectively.	93
6-6	Negative secondary ion mass spectrum resulting from bombarding crystalline αZrP with 136 keV Au_{400} . Secondary ion yields for PO_2 and PO_3 are 0.49 and 1.05 respectively.	94

FIGURE		Page
6-7	Negative secondary ion mass spectrum ($180 \leq m/e \leq 350$) resulting from bombarding α ZrP gel with 136 keV Au ₄₀₀	95
6-8	Negative secondary ion mass spectrum ($180 \leq m/e \leq 350$) resulting from bombarding crystalline α ZrP with 136 keV Au ₄₀₀	96

LIST OF TABLES

TABLE		Page
5-1	Secondary ion yields of selected secondary ions utilizing Au_{400}^{4+} primary ions with impact energies of 136 keV. (Relative error $< \pm 8\%$ for amino acid yields, $< \pm 10\%$ for CsI)	66
5-2	Secondary ion yields of selected Au^- and Au-adduct peaks of CsI bombarded by Au_{400}^{4+} at 136 keV as a function of number of primary ion impacts.	68
5-3	Secondary ion yields of selected negative ions detected from a CsI-Phe mix bombarded by 136 keV Au_{400}^{4+} . The 4 th and 5 th columns contain the correlation coefficients with the secondary ion in parenthesis.	73
6-1	Secondary ion yield for C_n ($n = 3-16$) clusters and Au_n ($n = 1-3$). (Relative error $< \pm 12\%$)	89

CHAPTER I

INTRODUCTION

Chemical analysis of solids was for many years mostly concerned with bulk assays. While this type of analysis remains important, increasing emphasis has been placed in recent decades on obtaining spatially refined information, e.g. surface analysis and depth profiling [1]. A large number of analytical techniques have been devised for characterizing atomic/molecular species at or near a surface [1]. These advances reflect the fundamental and technological importance of the domain of solids where physical and chemical properties can differ from those in the bulk.

One of the most versatile surface analytical techniques is secondary ion mass spectrometry, SIMS. SIMS is employed to investigate organic and inorganic samples in a variety of fields such as biological analysis, environmental studies and semiconductor technology [2-7]. This technique uses a beam of primary ions to sputter secondary particles from the surface [8]. The secondary particles are comprised of atomic and polyatomic neutrals, electrons and secondary ions (including atomic, fragment and molecular ions), which are representative of the analyte's surface. The sputtered ions are then accelerated through a potential gradient into a mass analyzer. Mass analysis can be accomplished through several techniques such as ion traps, quadrupole filters, magnetic sectors and time-of-flight. Each of these techniques have distinct advantages and

This dissertation follows the style and format of Applied Surface Science.

disadvantages.

The most significant parameter determining the performance of SIMS is the secondary ion yield. The secondary ion yield is defined as the number of secondary ions detected per primary ion impact. The use of atomic projectiles such as Cs^+ and O^- , with keV energies, result in secondary ion yields ranging from a few hundredths of a percent up to a few percent [8]. As an example, the secondary ion yield of $[\text{Phe-H}]^-$ is 0.37% when bombarded with 20 keV Cs^+ [9]. Hence, it requires 271 Cs^+ ions impacting a phenylalanine target to generate one $[\text{Phe-H}]^-$. The yields of elemental ions and small molecular ions have been enhanced with the use of laser post-source ionization, with nearly 100% efficiency [10]. But unless the laser is specifically tuned to the analyte of interest or other techniques, such as resonance ionization are used, the laser typically fragments the molecular species into its elemental constituents [10]. Becker et al. have used non-resonance ionization to provide chemical information and chemical images of surfaces [11]. The use of clusters as primary ions has been shown by many investigators to be an effective method to increase the secondary ion yields especially those arising from organic targets [12]. Blain et al. used $(\text{CsI})\text{I}^+$ and $(\text{CsI})_2\text{I}^+$ as primary projectiles and measured secondary ion yields that are nearly an order of magnitude greater than those measured when the same surface was bombarded with Cs^+ at equal velocities [13]. This work will be discussed in greater detail in Chapter II.

SIMS is a well suited technique for imagining surfaces. By rastering the primary ion beam across the surface, the location of chemical species can be revealed and an x-y image of selected species is produced. This technique has been effective in examining a

variety of samples. Lechene and Winograd have been able to map different types of biological samples including cells and cross-sections of various organs using SIMS as an ion microprobe [14-20]. The spatial resolution of the secondary ion signal is limited by the ability to focus the primary ion beam when imaging with an ion microprobe, (spatial resolution of an ion microscope is limited by the focusing ability of its secondary ion optics). Hence, if the primary ion beam can be focused to a diameter of 100 nm, then any two secondary ions desorbed from the same primary ion pulse are collocated within 100 nm of one another.

The area of secondary ion desorption from a large cluster impact, such as C_{60} , is approximately 10 nm in diameter [21]. Investigating a surface using SIMS in the event-by-event bombardment detection mode allows one to recognize all secondary ions that arise from a single ion impact. In the event-by-event mode of bombardment and detection, the surface is interrogated using a single primary ion impact (an event) and all secondary ions from that impact are detected prior to the arrival of the next primary ion. In an event where two or more secondary are detected from the same desorption event, they must come from the same desorption volume. Thus, coincidentally emitted secondary ions are collocated spatially within the desorption volume created by a primary ion impact [22,23].

A drawback to using single ion impacts is the low secondary ion yields produced by keV atomic projectiles. Cluster ions, such as Au_3^+ , produce secondary ion yields of a few percent for organic targets such as phenylalanine [24,25]. The impacts of monatomic and small cluster primary ions result in zero secondary ions detected for

most desorption events. The next most probable event would be the detection of one secondary ion per primary ion impact [25]. However, there are rare events where two or more secondary ions are detected. These “super-efficient” events offer insight into the surface’s composition. As noted already, they provide information regarding the surface composition by revealing information about two (or more) chemical species located within the desorption volume. These events occur with atomic projectiles, but their frequency increases as the complexity of the projectile increases. Therefore, to efficiently utilize single projectile impacts as a method for surface interrogation a projectile is needed that generates increased secondary ion emission, including secondary ion yield and the occurrence of “super-efficient” desorption events.

An obvious large projectile is C_{60} . Van Stipdonk et al. have examined the emission characteristics C_{60} versus Cs and Ga primary ions on CsI and phenylalanine targets. Secondary ion yields for the carbon cluster projectiles are in excess of 80 times greater than the monatomic projectiles [26]. Recently the usefulness of a still larger and more massive projectile has been investigated. Large gold clusters emitted from a liquid metal ion source, LMIS, are proving to be an efficient means for studying surfaces [27]. A stable massive cluster which can be produced by the LMIS available at Texas A&M has a $m/z \sim 20,000$ amu ($n/q \sim 100$ Au atoms). Research by Bouneau et al. has shown that these massive clusters contain an average of 400 Au atoms with a charge of $4+$ [28]. Tempez et al. used Au_{400}^{4+} in the investigation of biological compounds such as gramicidin S and dynorphin 1-7 [27]. Protonated molecule yields were enhanced by a factor of 1000 over those obtained with Au^+ . Another finding was that the damage

cross-section to the target was much lower than those observed with Au_5^+ and Au_9^+ [27]. Rickman et al. have reported an increase in the occurrence of “super-efficient” events from targets bombarded by these massive clusters [29]. The average number of secondary ions detected from a phenylalanine target from a Au_3^+ impact is less than one secondary ion per impact. In comparison, an average of 10 secondary ions is detected per event for the same target bombarded by Au_{400} . The detection of 8 secondary ions per event is most probable. The enhanced secondary ion signal resulted in the need to develop a method to detect the increased number of secondary ions desorbed per event. These massive gold projectiles offer the potential to enhance secondary ion signal from a single projectile impact and provide information regarding surface homogeneity down to the nanometric volume of the desorption volume of a single cluster impact.

To investigate single ion impacts of massive gold clusters, the first objective of this research was to modify the mass spectrometer’s secondary ion detector from a single anode design to a multi-anode design. Changing the anode to a multi-collector design permits the detection of multiple secondary ions that have the same m/z per event.

The second objective was to measure the emission characteristics resulting from impacts of massive clusters. Parameters to be examined include secondary ion yields, secondary ion multiplicity (the occurrence of “super-efficient” events) and the occurrence of Au-adduct secondary ions. These parameters should provide insight into the feasibility of using massive Au projectiles as a tool for event-by-event bombardment of a surface for the purpose of imaging.

A further objective was to evaluate the effectiveness of these massive projectiles in understanding the physical characterization of surfaces and how their physical construct compares at the nano-domain level. Amorphous and crystalline compounds having the same stoichiometry along with graphite targets with different degrees of structural order will be examined.

CHAPTER II

SECONDARY ION EMISSION FROM keV PROJECTILE IMPACTS

The purpose of this review is to summarize developments in secondary ion mass spectrometry pertinent to the present study.

Ion beams were first used to interrogate targets in 1949 and are an effective means to extract both chemical and elemental information from a surface [30]. SIMS is a technique where an energetic beam of ions is accelerated towards a surface and the ejected ions are separated by their mass-to-charge ratio (m/z). The primary ion beam ranges in energy from a few hundreds eV to several MeV. The secondary ions are a result of the primary ion impacts which erode/sputter atoms/molecules away from the surface and into the gas phase. The ejecta are sputtered from the uppermost layers of the target, where a certain percentage will be ejected as ions. As a result of ions originating from this region, SIMS is one of most surface sensitive and specific analytical tools known [31]. The secondary ions are analyzed based on their m/z by several methods including: time-of-flight, quadrupole and electric/magnetic mass analyzers. SIMS can be divided into two categories: static and dynamic. In static SIMS the primary ion dose is maintained below the static limit which is $\sim 10^{12}$ primary ions/cm² or approximately 1% of the surface molecules [32]. Maintaining the primary ion dose below the static limit ensures that it is statistically improbable that a primary ion will impact the area already interrogated by a previous primary ion. Static SIMS is considered a non-destructive method due to its low primary ion dose. Dynamic SIMS utilizes a beam of

primary ions which has fluence greater than $\sim 10^{12}$ primary ions/cm². Since the primary ion dose is so high the statistical probability of a primary ion striking the same area probed by a previous primary ion is virtually 100%. Since the target is ablated with such a high dose of primary ions, dynamic SIMS is considered to be a destructive technique.

In addition to primary ion dose, SIMS can be further categorized by its uses: imaging and non-imaging. The first imaging SIMS instrument was reported in 1962 by Casting and Slodzian [33]. This ion microscope permitted surface analysis with a lateral resolution of approximately 1 μm . The sputtered secondary ions were focused and steered to an imaging detector using a series of lenses and a magnetic field. This design was commercially marketed by Cameca a few years later. Scanning ion microprobes are a second type of imaging SIMS instrument. This instrument operates by rastering a primary ion beam across the surface of a target. An image is acquired by correlating the secondary ion signal to the position of the primary ion beam. Imaging of a surface can be performed in either the dynamic or static regime. In 1967 the first commercial non-imaging SIMS instrument was introduced. This instrument was based on the design set forth by Herzog and Viehboeck in 1949 [30]. Primary ions were generated in a gas charged cathode ray tube. Ions formed near the anode were able to escape as canal rays to become primary ions. This ion source was coupled with a single magnetic sector to produce a mass spectrograph. Later instruments included double focusing magnetic sectors. Instruments of this design are operated in either the dynamic or static regime.

All experiments described within this dissertation were performed in the event-by-event bombardment detection mode. Time-of-flight mass spectra are collected by

one of two means. The first is to bombard the target using a continuous beam of primary ions. The secondary ions are accelerated away from the target where they are collected/bunched together and subjected to an external electric field where they are accelerated into a time-of-flight mass analyzer [27]. A second method of performing a time-of-flight experiment is to pulse or chop the primary ion beam so that a small fraction of the beam impacts the sample over a very short period of time [34]. This method allows a smaller amount of the sample to be consumed when compared to a continuous beam. The event-by-event bombardment detection mode is similar to the pulsed beam set-up, with the exception that only a single primary ion impacts the target instead of a group/bunch of primary ions. Single ion impacts offer several advantages. From a fundamental point of view, it allows for investigation into secondary ion yields from single projectiles [35]. It also facilitates more analytically useful information from the primary ion impact site. The volume perturbed from a single primary ion impact, such as C_{60} , has a radius of approximately 5 nm [21]. Therefore, all secondary ions detected in a single event must originate from that desorption volume. Hence, the secondary ions come from surface molecules collocated within that 10 nm diameter volume.

Secondary ion signal is a direct result of a primary ion impact and its subsequent interaction with the atoms/molecules of the target. It is commonly thought that the collision cascade resulting from a primary ion impact is similar to a billiard ball model. In 1969 Sigmund proposed that when a particle with energy in the keV range strikes the surface, it undergoes a series of elastic collisions with the atoms of the solid [36]. The

target atoms set in motion from the primary ion impact will in turn collide with their surrounding atoms in the target creating a series of collisions, or in other words, a collision cascade. The collision cascade sets the atoms of the target into random motion. When an atom/molecule at or near the surface undergoes a collision that gives it momentum in the upward direction away from the surface, with an energy greater than its bonding energy, it is sputtered into the gas phase as either a neutral or ion. Sigmund's theory was adequate for describing the sputter yields for projectiles with a low mass (z), but the theoretical sputter yields were substantially lower than experimental results for high z primary ions such as Xe and Hg. The shortcomings of the linear cascade model for high z and cluster projectiles were later explained by the energy spike model [37]. In this scenario, bombardment of a heavy atom induces several collision cascades which overlap each other near the epicenter of impact. The overlapping cascades create a region where the atoms/molecules of the target have a high energy density causing the enhanced sputter yields observed.

In 1973 Andersen et al. performed a series of experiments to determine the validity of the spike effect model in regards to heavy ion bombardment [38]. The authors bombarded Si, Ag and Au targets using Te^+ , Se^+ and Cl^+ . To increase energy density at the point of impact, the authors also used the diatomic species of the aforementioned primary ions. The energy per constituent atom in the projectile was constant for both experiments. It was found that the sputter yield for the diatomic species showed a nonlinear enhancement over that of the monatomic species. Secondary ion yield enhancement will be defined later in this chapter. The authors discovered that

when the sputter yield per constituent atom of the diatomic projectile was compared to that of the monatomic, there was a yield enhancement in excess of unity in each case. Their data also show that the yield enhancement increases as the mass of the projectile increases. Andersen and Bay continued this study in 1974 to include a broader range of primary ions [39]. This work and the nonlinear enhancements in sputter yield lead to a thermal spike model. Their work was so compelling that Sigmund modified his collision cascade model to account for the thermal spike's influence in the sputtering process [40].

To explain the high sputter yields resulting from polyatomic bombardment, Johar and Thompson introduced the collisional spike model which is a result of the polyatomic projectile disintegrating into its atomic components upon impact [41,42]. Each of these atomic projectiles, with a fraction of the initial kinetic energy of the original polyatomic, initiates their own series of collision cascades. The multiple overlapping collision cascades created by the atoms from the cluster create an area on the surface that is damaged or roughened which can enhance the sputter yield. From an analytical point of view, the greater the yield from a single primary ion impact, the more information that can be gathered in regards to its chemical composition [43].

There are three models used to predict the angular distributions of secondary ions resulting from energetic ions impacting on a surface. The first model is known as "phase explosion"; in this model, the secondary ejecta have a momentum in the X-direction which is opposite from that of the projectile. The secondary ejecta are desorbed via a gas jet from the resulting impact crater [44]. This type of emission

usually occurs with higher energy projectiles such as the fission fragments used in plasma desorption mass spectrometry (PDMS).

The “thermal spike” model results in a secondary ion distribution that has a net normal distribution from the surface. This model takes in account that there is a sharp thermal spike at the impact crater, and there is an evaporation of analyte from a close proximity around the impact area [45,46]. It is important to understand that there is a high density of ejecta in volume in the immediate vicinity of the crater, and there is a high probability of gas phase collisions in this region. The nature of the thermal desorption and the subsequent collisions results in an angular distribution of ejecta near the crater. However, this angular distribution is symmetric around the impact site resulting in a net normal distribution.

The pressure-pulse or shockwave model results in secondary ions with an angular distribution which maintains a fraction of the momentum of the primary projectile, in the X-direction [47]. Ions with this trajectory occur when surface atoms are sputtered from the surface as a result of the shock-wave which is propagated from the primary ion impact.

To better understand the yield enhancement created by polyatomic ion bombardment, a useful quantity is needed for comparing the secondary ion yields of both cluster and monatomic projectiles. One method to compare yields is to calculate the enhancement factor. As noted previously, a polyatomic primary ion disintegrates upon impact into its constituent atoms, where each has a fraction of the original cluster’s kinetic energy, and initiates its own collision cascade. Therefore, the enhancement

factor (ϵ) must take into account the number of atoms in the projectile. Calculations of ϵ are valid only if the secondary ion yields are from experiments where the energy per atom of the projectile (E/n) is constant. The enhancement factor is defined using the following equation:

$$\epsilon = \frac{Y_m n}{Y_n m} \quad (\text{for } m > n)$$

where Y_m is the secondary ion yield resulting from an m -atom projectile and Y_n is the secondary ion yield from an n -atom projectile. For $\epsilon > 1$ there is a secondary ion yield enhancement for the m projectile [13].

Enhanced sputter yields from polyatomic projectiles have been studied since 1960 [48,49]. Most of these studies focused on metal targets such as Cu, Ag, Au and their respective oxide layers in an attempt to gain a fundamental understanding of the sputtering process. In 1987 researchers at Idaho National Laboratory (INEEL) used a molecular beam of SF_6 to interrogate films of Teflon, Mylar, and Acrylic [50]. A neutral beam was employed because these materials are insulators. The use of ions presents the problem of charge accumulating on the sample surface. Appelhans et al. developed a source that delivers a focused beam of neutral molecules to the surface that can also be rastered across the surface. This was performed by subjecting SF_6 gas, which has a high cross-section for electron capture, to a low energy electron flux. Once the SF_6^- ion is formed, it is accelerated from the source, focused and has its trajectory adjusted (for rastering) prior to undergoing autoneutralization to SF_6 . Under conditions of similar impact energies, the authors have determined that the secondary ion yields for the neutral cluster were 3-4 orders of magnitude greater than that of a monatomic projectile

(either ion or neutral). In a later study, Appelhans and Delmore studied the secondary ion yields resulting from projectile impacts of Cs^+ and SF_6 (similar E/amu) [51]. The authors report that the secondary ion yields for the cluster projectile were 9 – 24 times greater than the monatomic projectile. They go on to explain that the enhanced secondary ion yields under cluster bombardment are due to the collective effect of several collision cascades, a mechanism similar to the collisional spike model discussed earlier in this chapter.

Studies performed concurrently with those described above at Texas A&M and the Institute de Physique Nucleaire (IPN) in Orsay, France have produced a series of results in regards to secondary ion yields from both organic and inorganic targets using a variety of projectiles [13,52]. Secondary ion yields from phenylalanine, CsI and gold were reported when bombarded with Cs_mI_n^+ ($m = 1, 2, 3$; $n = m-1$), coronene, coronene dimer and phenylalanine at varying impact energies. The authors cite that supra-linear yield enhancements exist for all three targets when bombarded with Cs_mI_n^+ clusters versus that of the Cs^+ ion. In fact, values of ϵ up to 50 were calculated for the organic target.

Bengueerba et al. examined the secondary ion yields of phenylalanine resulting from bombardment of Au_n^{m+} ($n = 1 - 5$, $m = 1, 2$) [24]. Non-linear effect was identified for all secondary ions ranging from simple fragments such as H^+ up to and including the molecular ion. The enhancement factor was strongest for the more complex secondary ions versus the atomic species. The increasing complexity of the primary ion (increasing n) was the dominant parameter resulting in increased secondary ion yields.

Szymczak and Wittmaack investigated secondary ion emission of CsCl under bombardment from 24-31 keV Xe^- and SF_6^- . The secondary ion yields observed for $(\text{CsCl})_n\text{Cs}^+$ ($n < 10$) showed an enhancement factor up to six for $n > 3$ [53].

Van Stipdonk et al. studied the secondary ion yields from phenylalanine and CsI targets bombarded by C_{60}^+ and $(\text{CsI})_n\text{Cs}^+$ in comparison to Cs^+ and Ga^+ at 20 keV [54]. Ga^+ in the event-by-event mode was not efficient enough to produce significant secondary ion yields for a useful comparison. Therefore, yields resulting from cluster bombardment were compared to those obtained from Cs^+ bombardment. The enhancement factor was not calculated. At 20 keV, the secondary ion yields from the CsI target were between 6-85 times greater from C_{60}^+ than Cs^+ . The secondary ion yield from C_{60}^+ on phenylalanine for $(\text{Phe-H})^-$ was nearly 18 times greater than Cs^+ at the same energy on the same target.

Secondary ion multiplicity is defined as the number of secondary ions detected per desorption event [55]. An event is defined by the impact of a single primary ion resulting in a start signal for data acquisition of subsequent secondary ions resulting from that impact. In 1994, Zubarev et al. measured the multiplicities for several different projectiles at different energies on CsI targets [56]. It is interesting to point out that the authors observed between 95 – 98% of detected secondary ion are not specific to the analyte. The authors deconvoluted the measured multiplicity and were able to determine the number of secondary ions per event detected per primary ion impact. Zubarev concludes that the secondary ion multiplicity increases as the energy of similar

primary projectiles increase, and also increases as the mass of the primary projectile increase for a constant energy [56].

A coincidence experiment involves the detection of several different types of emissions that all originate from a particular event. Nuclear scientists have been using this technique to gain a more accurate understanding of the decay of radioisotopes [57]. In our case, the event is the impact of a primary ion on the target [58]. The subsequent charged ejecta are detected in coincidence with the primary ion impact. To begin any coincidence experiment, it is necessary to detect secondary electrons resulting from the primary ion impact. These two events are the minimum needed for a coincidence experiment, since the output signal generated from the secondary electrons are responsible for the start signal, which begins the ToF measurements. Therefore, any secondary ions detected are in coincidence with the secondary electrons. Instrument design and operation will be covered in the next chapter.

To gain a better understanding of how surfaces are physically assembled it is useful to examine any secondary ions that are detected in coincidence with one another. If ion A and ion B are detected and originate from the same desorption event, then they are colocated within the desorption volume of a single primary ion impact. This information only tells part of the story. The question arises: while these secondary ions originate from the same nano-spot on the surface, to what extent does their coincidental emission correlate with one another? Is their coincidental emission correlated, uncorrelated or anti-correlated? If two coincidental ions are uncorrelated, this means their emission/detection is not dependent on the other and their probability of being co-

emitted is quite simply the product of separate detection probabilities, as the following equation shows:

$$Q_{A,B} = \frac{P(A,B)}{P(A) * P(B)}$$

where Q is the correlation coefficient, P(A,B) is the probability of detecting ion A and ion B in coincidence with each other and P(A) and P(B) are the probabilities of detecting these secondary ions regardless of what else may be detected (other than secondary electrons). Therefore, if Q = 1 the coincidental emission of A and B are independent from one another [58]. If Q > 1, this implies that the emission of A and B are correlated or that the emission of one aids in the emission of the other. For Q < 1 the co-emitted species are anti-correlated. In other words, the emission of one ion prevents/inhibits the emission of the other. Coincidence counting mass spectrometry not only yields information on the location of different species in regards to others, but also provides insight to their interaction with one another during the sputtering process.

CHAPTER III

INSTRUMENTATION AND ELECTRONICS

A schematic of the LMIS cluster SIMS instrument is presented in figure 3-1. This instrument was used in the experiments discussed throughout this dissertation. The instrument is divided into two major regions: the primary ion leg and the secondary ion leg, which intersect at the sample/target. The primary ion leg and secondary ion leg are separated via a gate valve.

The primary ion leg is responsible for primary ion generation and delivering single ions to the target surface, it consists of a gold liquid metal ion source (Au-LIMS, Institute de Physique Nucleaire, Orsay), focusing lenses, Wien filter, and pulsing plates. The primary ion leg is approximately one meter in length, from the LIMS to the target. The vacuum is maintained at approximately 10^{-7} torr by a 60 l/s turbo molecular pump (Pfeiffer Vacuum) which is backed by a 1.5 cfm rotary vane pump (Welch).

The primary ion beam emitted from the LIMS is composed of a mix of ions, Au_n^{m+} where $1 \leq n \leq 1000$ and $1 \leq m \leq 10$. The LMIS consists of a tungsten reservoir, which is tightly wound coil of 0.200 mm tungsten wire consisting of between 8 – 10 turns, filled with a Au-Si eutectic (97% Au – 3% Si by mass). Passing through the center of the reservoir is a straight piece of tungsten wire (the needle) which is anchored to the base of the assembly and its tip extends 1.3 mm above the reservoir. The tip of the needle is etched to a 90° point to facilitate the formation of a Taylor cone during ion extraction (figure 3-2). The needle is approximately 1 mm from an extraction electrode

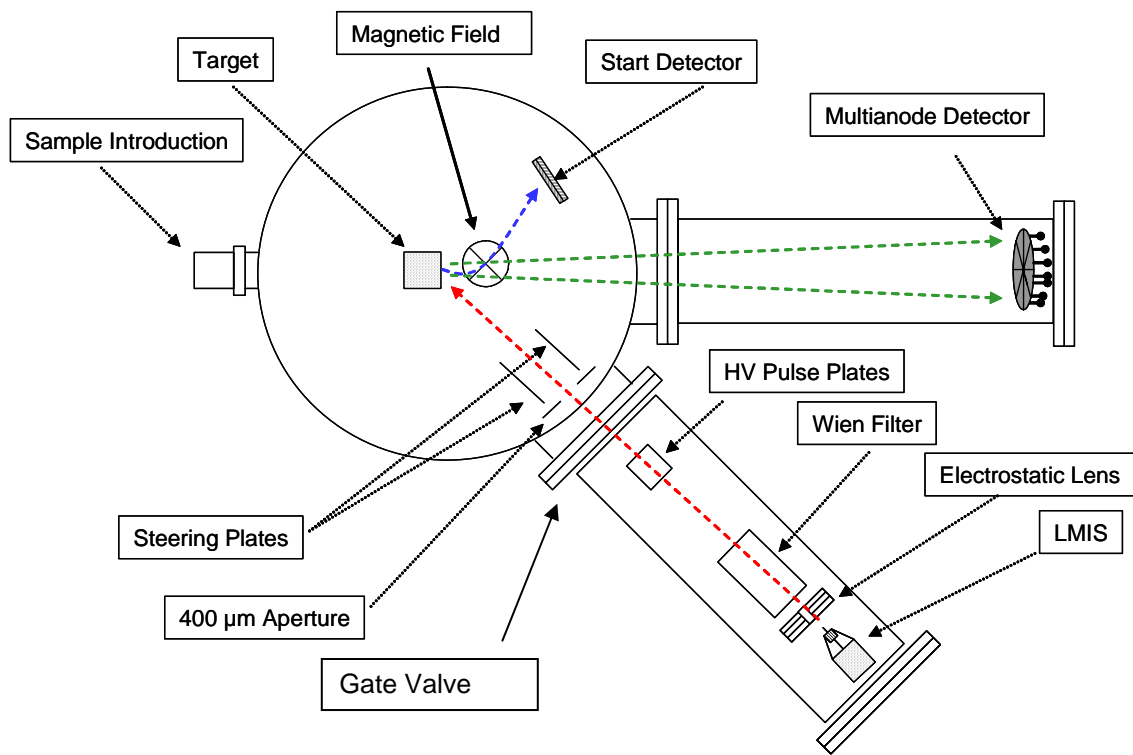


Figure 3-1 Schematic of the LIMS cluster time-of-flight secondary ion mass spectrometer.

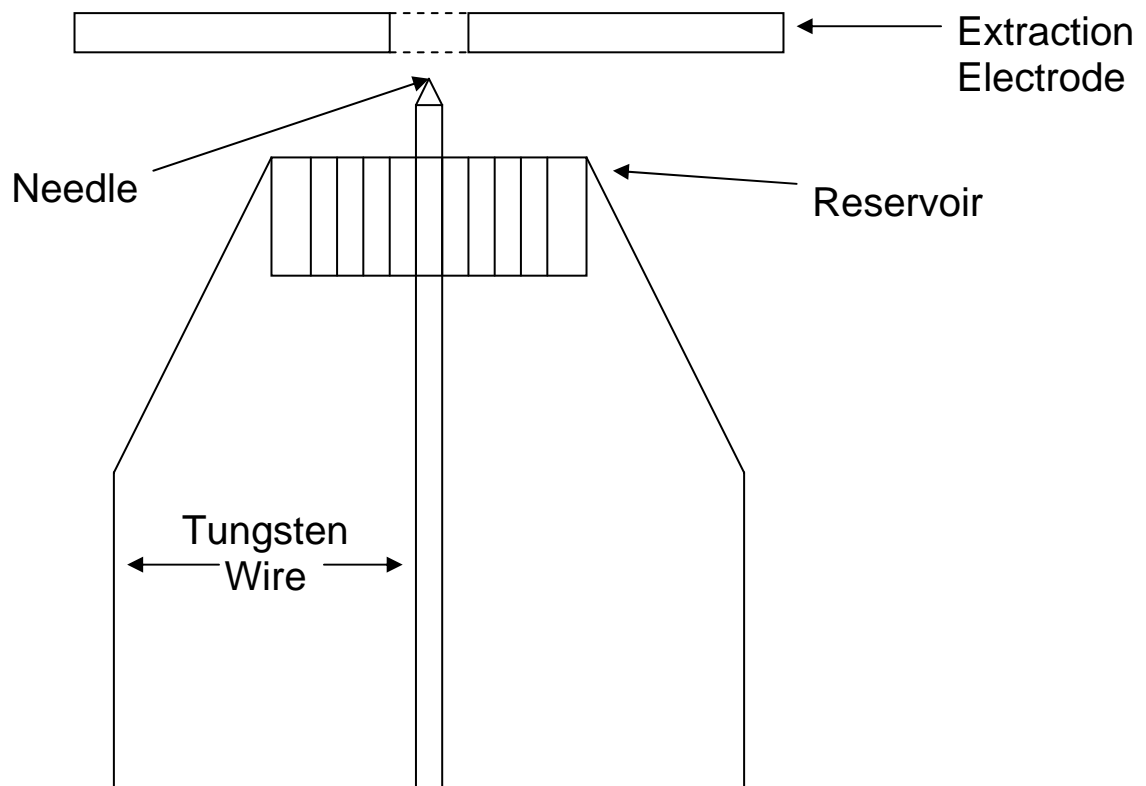


Figure 3-2 Schematic of the Au-Si LIMS (not drawn to scale).

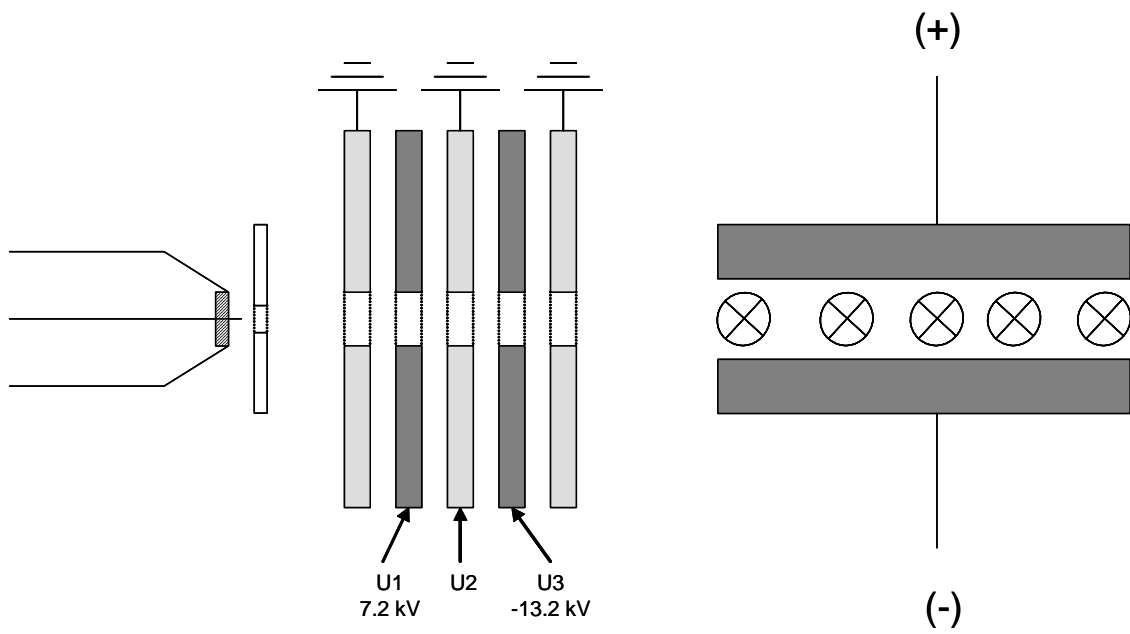


Figure 3-3 Schematic of the LIMS, lens assembly and Wien filter.

which is maintained at -11 kV relative to the needle. A detailed explanation regarding the assembly of the LMIS can be found in reference [43]. Once the LMIS is emitting ions, the emission current is controlled using the extraction potential. The primary ion beam is focused using a series of electrostatic lenses (figure 3-3). Lens U2 is maintained at ground, U1 has a positive potential and U3 is maintained at a negative potential. The potentials on U1 and U3 are adjusted proportionally in regards to primary ion kinetic energy [43].

The focused primary ion beam then passes through a Wien filter where the primary ion of interest is mass selected. A Wien filter uses magnetic and electric fields which are perpendicular to one another. Ions of a specific velocity and charge pass through the Wien filter unperturbed while those which do not possess these specific properties are deflected from the Wien filter's exit orifice. The Wien filter's magnetic field is approximately 0.3 T and is maintained using a constant current power supply (Bertan), at 2 A, powering the electromagnet (Electropreci, Paris, FR). Mass selection is accomplished by varying the filter's electric field using a 0-1 kV power supply (Ortec, Model 935). Individual clusters can be selected with the Wien filter up to and including Au_9^+ . For clusters with more than 9 atoms the filter will allow a range of ions within a specific n/q range. Since the mass selection process is based on the primary ion's velocity, the Wien filter must be adjusted for different energies of primary ions or when the mass of the primary ion of interest has changed. The equation determining the velocity of the primary ion allowed to pass through the Wien filter [59] can be

rearranged and simplified to calculate the required potential needed on both electric plates to permit passage of the desired primary ion:

$$V_{\pm} = k\sqrt{E_{KE}/m}$$

where V_{\pm} is the potential (\pm) applied to each plate (V), E_{KE} is the kinetic energy of the primary ion (eV), m is the mass to charge ratio of the primary ion (amu) and k is an empirical constant for the instrument based upon the physical dimensions of the wien filter, strength of the magnetic field and conversion factors. For this instrument $k \sim 26.109$.

The mass selected beam travels from the outlet of the Wien filter through a set of high voltage pulsing plates. One of the plates, which are parallel to each other, is maintained at ground ground while the other is pulsed from a negative to positive voltage. This high speed switching of potentials is accomplished using a push-pull MOSFET (Belkhe, HTS151-03-GSM, Germany) which can switch from ± 15 kV at a rate of 10 kHz with a rise time of ~ 25 ns. Voltage is supplied to the switch using two 1 kV power supplies (Glassman, EK series, USA). Triggering for the switch is accomplished using a pulse generator (Hewlett Packard, 8005B, USA).

The primary ion beam is pulsed for two reasons. First, it allows for a start signal for the time-of-flight measurement of the primary ions and secondly and most significantly it reduces the primary ion beam intensity to the point where the conditions for single ion impacts are achieved. This type of beam pulsing is known as the differential impulse sweep method (DISM) [34]. The primary ion beam enters the

pulsing region and as the plates are pulsed from negative to positive only ions in the center few millimeters of the pulsing region satisfies the conditions needed to pass through the 400 μm exit aperture. Additionally, only the ions in the exact center of deflection plates during a pulse receive no transverse velocity whatsoever, since the conditions of equal pulsing potentials has been satisfied [34]. The magnitude of the pulsing potentials directly controls the number of ions which can pass through the aperture without any deviation in their velocity, the greater the magnitude of the pulse, the fewer ions which pass through the aperture unperturbed. Primary ion fluence can also be reduced by defocusing the primary ion beam by adjusting the potential on U1 and U3. The use of focusing/defocusing, DISM and the exit aperture reduce the beam intensity to between 0.1 – 0.2 ions per pulse, satisfying conditions for event-by-event measurements.

After exiting the pulsing region, the ions are then steered onto the target using a series of horizontal and vertical steering plates. This function is needed to ensure the primary projectile strikes the target in such a manner that the secondary ion distribution is equal on all eight anodes of the secondary ion detector. The steering plates are powered by two adjustable (± 3 kV) high voltage power supplies (Tennelec, 952A, USA and Fluke, 415B, USA); one horizontal and one vertical. The secondary electrons resulting from the primary ion impact trigger the start for the time-of-flight analysis of the secondary ions also serves as the stop signal for the primary ion time-of-flight measurement. While the primary ion leg is approximately one meter in length, the primary ion time-of-flight length is 50.5 cm.

The target and secondary ion time-of-flight region are housed in a custom manufacturer stainless steel chamber (Kurt J. Lesker, USA) and maintained at $\sim 10^{-7}$ torr using a 760 l/s diffusion pump (Edwards Vacuum Products, USA) which is backed by an 18 cfm rotary vane mechanical pump (Edwards Vacuum Products, USA).

The target is either a stainless steel or brass cube that is 1.5 cm per side. The surface in which the sample is located measures 1.0 cm x 1.5 cm. The target cube is introduced to the instrument utilizing a sample insertion probe (MDC Vacuum, USA) which is connected to the vacuum system via a gate valve and three-way KF tee fitting. Once the sample insertion probe has been attached to the instrument the region is evacuated using a mechanical pump to $< 3 \times 10^{-2}$ torr. When the pressure is below 3×10^{-2} torr the gate valve to the high vacuum region of the instrument is opened and the sample is inserted into sample block holder, which is constructed with Teflon. The sample is then biased to -9 kV using a high voltage power supply (Bertan, 225, USA) and is located 7 mm from a 90% transmission grid at ground. The field gradient is responsible for accelerating the secondary ions and electrons from the target surface.

When a primary ion impacts the target negatively charged secondary ejecta are accelerated to a constant kinetic energy into the time-of-flight region. Approximately 5 cm into this electric field free region the negatively charged ejecta encounter a weak magnetic field, which is produced from a homemade electromagnet. This field is not strong enough to significantly alter the flight path of the secondary ions but, it is strong enough to steer the electrons in to a microchannel plate (MCP) assembly. The output generated from the secondary electrons is used for the start of the time-of-flight

measurement. The secondary ions continue down the 88 cm flight tube where they are separated based on the square root of their mass to charge ratios (figure 3-4). They are detected with a second MCP assembly and their arrival times recorded.

The mass of both primary and secondary ions are determined using time-of-flight (ToF) mass analysis. This is accomplished by measuring the time it takes an ion to travel from its point of formation through an electric field and a field free region. The flight time is measured from a start signal which is triggered from an event that creates the ion, such as a primary ion impact, to the time the (secondary) ion is detected at the stop detector. ToF offers two unique advantages over other mass analyzing techniques such as a quadrupole or sector instruments. The ToF mass analyzer offers the user the ability to detect ions over an unlimited mass to charge (m/z) range, whereas scanning instruments have a well defined m/z range for the ions they can detect. The most significant advantage of ToF is its ability to detect all ions from a desorption event [60]. As compared to a sector or quadrupole instrument where the instrument needs to be scanned across a range of masses and can only detect one specific m/z ion at a time. This is an important advantage because it not only enhances the sensitivity of the measurements, but also allows the investigator to gain detailed chemical information from the volume perturbed by a single primary ion strike, because all ions detected must originate from this volume.

A secondary ion desorbed from the surface passes through an acceleration region into the field free region and then through a deceleration region prior to striking the detector. Therefore, the total amount of time, t_T , required for an ion from creation to

Time-of-Flight

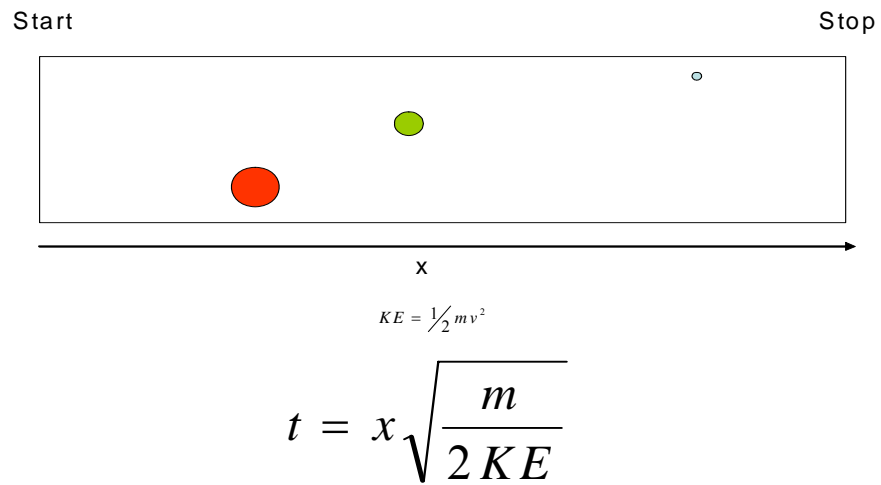


Figure 3-4 Schematic of the field free drift region.

detection is the summation of the amount of time it spends in each area and is represented by the following:

$$t_T = t_s + t_D + t_d$$

where t_s and t_d are the ion's flight times in the source and detector regions and t_D is the ion's time in the field free drift region [61].

ToF measurements are based on the premise that all secondary ions are formed at the surface, or very close to the surface, and accelerated in a manner that they all possess the same kinetic energy. The force acting upon them is proportional to the strength of the electric field in which they are present in accordance with the following relationship:

$$F = ma = qzE$$

where F is the force action upon the ion, m is the ion's mass, a is acceleration, q is the fundamental electric charge, z is the charge on the ion and E is the field strength. Field strength is calculated as volts per unit length:

$$E = U/s$$

where U is the potential difference between the target surface and grid which define the acceleration/deceleration region and s is the length of these regions. The acceleration experienced by the ion is shown as:

$$a = \frac{qzE}{m} = \frac{qzU}{ms} = \frac{dv}{dt}$$

Rearranging the first and last terms above, solving for v and integrating yields:

$$v(t) = a(t) + v_o = \frac{dx}{dt}$$

where v is the velocity at time t while the ion is in the acceleration/deceleration regions, v_0 is the initial velocity of the ion and x is the location of the ion. Rearranging the above and solving for x and integrating gives the following:

$$x(t) = \frac{at^2}{2} + v_0t + x_0$$

where $x(t)$ is the location at time t the ion is in the acceleration/deceleration regions, and x_0 is the location of the ion when it is formed. Secondary ions are formed at the surface, therefore $x_0=0$. Knowing this and solving the above equation for t yields:

$$t_{a/d} = \frac{\sqrt{[v_0^2 + 2ax(t)]} - v_0}{a}$$

While there is a distribution of initial kinetic energies of secondary ions in a SIMS experiment, these ions only possess a few eV of energy initially before being accelerated to 9 keV. Therefore, their initial velocity is much less than their terminal velocity after leaving the source region. Hence, $v_0 \approx 0$ and the above equation reduces to:

$$t_a = \frac{\sqrt{2sa}}{a} = \sqrt{\frac{2ms^2}{qzU}}$$

An ion's flight time is dependent upon its m/z and the potential of the target in the acceleration region.

After the ion leaves the source region it enters the field free drift region and its flight time is simply based on its velocity as it enters the drift region and the length of the drift region, D . All ions leave the source region with the same nominal kinetic energy, KE ; therefore, their velocity is function of their mass as shown in the following relationships:

$$KE = \frac{mv_D^2}{2} = qzE$$

$$v_D = \sqrt{\frac{2qzE}{m}}$$

Solving for flight time in the drift region results in the following:

$$t_D = \frac{D}{v_D} = \sqrt{\frac{D^2 ms^2}{2qzU}}$$

Therefore, the secondary ions total time of flight is shown below:

$$t_T = \sqrt{\frac{2ms^2}{qzU}} + \sqrt{\frac{D^2 ms^2}{2qzU}} + \left[\frac{\sqrt{[v^2 + 2ad]} - v}{a} \right] = t_a + t_D + t_d$$

Secondary electron and secondary ion detection is accomplished by utilizing dual microchannel plate assemblies, MCP (Burle, 30286 (25 mm active area for the secondary electron detector) and 34251 (40 mm active area for the secondary ion detector), USA). MCP are an effective means for ion detection in ToF experiments due to their relatively fast response times and low recovery times needed for these experiments [62], and their efficiency for detecting charged particles [63]. A MCP is an electron multiplier with thousands of separate channels (dynodes) [63]. Each channel has the ability to convert a single particle impact to an output of $\sim 10^3 - 10^4$ electrons. Therefore, a gain of $10^6 - 10^8$ is achieved. The electrons that are emitted from the second MCP are accelerated towards a collector. When they strike the collector a negative voltage pulse is detected registering the arrival of a secondary ion.

Both MCP detector assemblies used in this instrument employ two MCP's parallel to one another in a chevron configuration. Schematics of both the secondary

electron and secondary ion detectors are shown figures 3-5 and 3-6. The secondary ion detector assembly will be covered in greater detail in the following chapter. This configuration has two advantages. First, it allows for a significant enhancement in signal gain over that of two straight channel MCP's. Also, this configuration prevents positive ions sputtered from the anode, due to electron impact, from drifting back into the MCP channels thereby eliminating the potential for spurious pulses following secondary ion detection [63]. Each detector assembly is powered by a high voltage power supply (Tennelec, 952A, USA).

After the electrons exits the second MCP it is accelerated with approximately 200 – 400 eV of energy towards a collector (anode), which in the case of the start detector is a copper plate and the stop detector is an arrangement of eight separate anodes. The eight-anode detector is described in detail in the following chapter. The impact of the electrons creates negative voltage pulse with an amplitude between -50 to -200 mV with a pulse duration between 5 – 10 ns. This output signal is then fed to the input of a constant fraction discriminator, CFD (Tennelec, TC454, USA for the start detector and an Ortec, CF8000, USA for the stop detector). Using a CFD to shape the signal prior to it being sent to the time-to-digital converter, TDC, has two distinct advantages. The CFD's output is a negative one-volt NIM pulse which had a variable pulse width from 5 ns to more than 1 μ s. The square-wave output of the CFD has a constant rise-time and peak height which triggers the TDC regardless of the peak shape of the CFD's input, thereby minimizing peak broadening [64]. Additionally, the CFD allows for threshold discrimination of the anodes output. The discriminator permits the

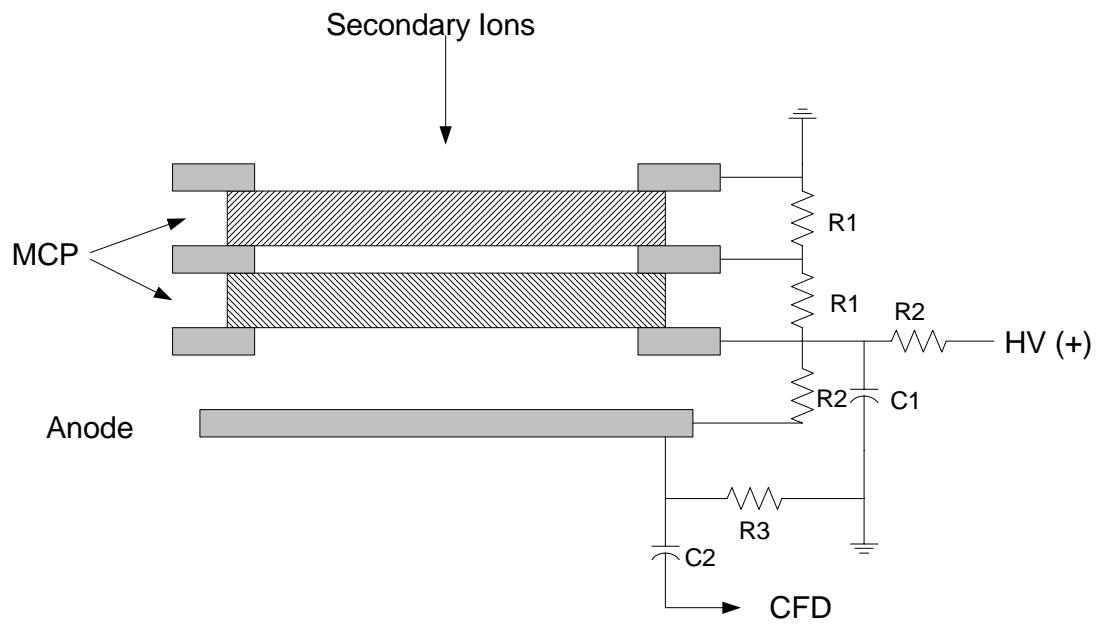


Figure 3-5 Schematic cross-section of the secondary electron MCP assembly.

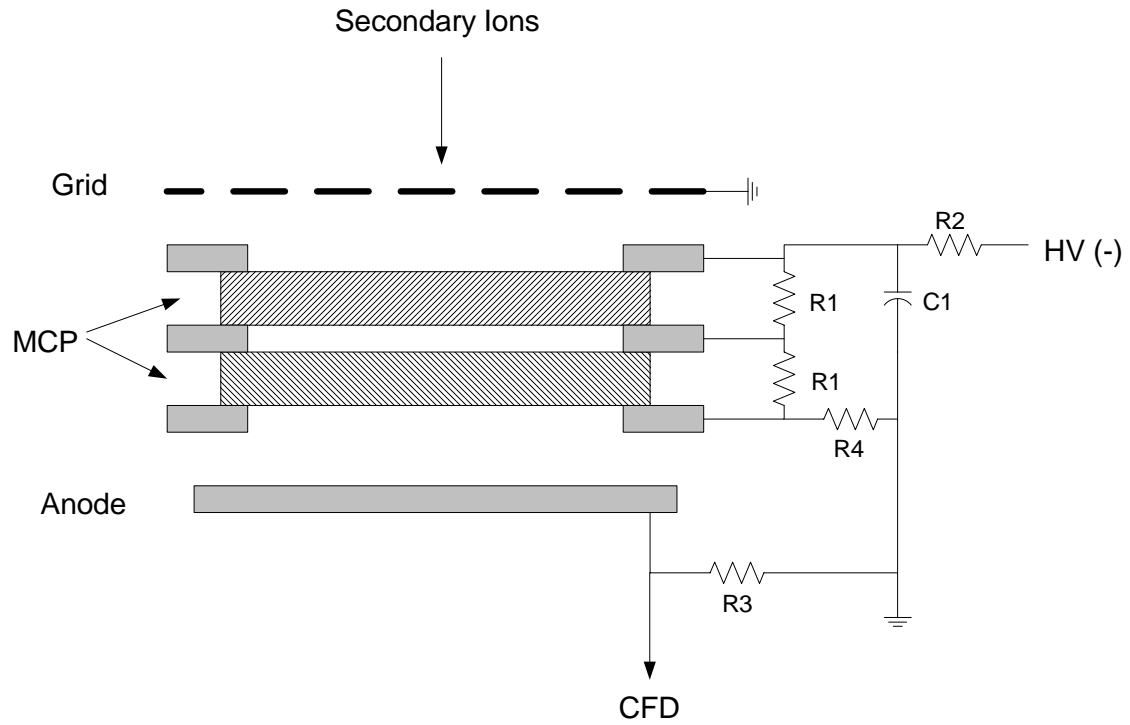


Figure 3-6 Schematic cross-section of the secondary ion MCP assembly.

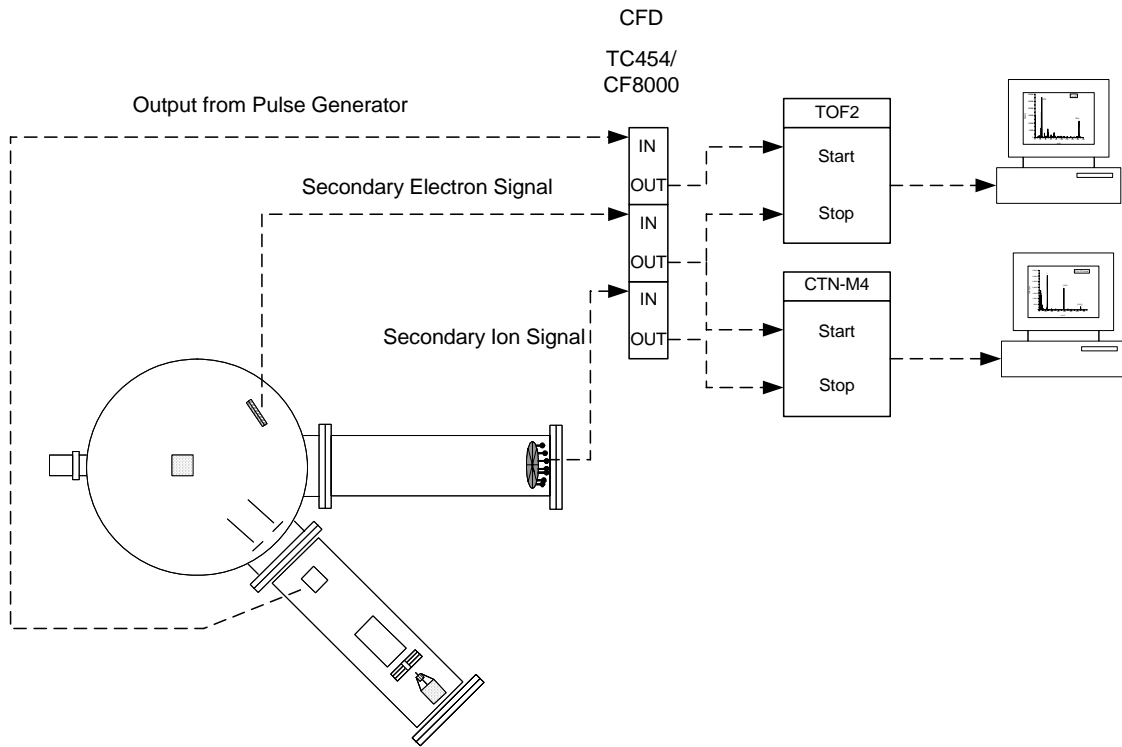


Figure 3-7 Signal processing schematic for the LMIS cluster SIMS instrument.

CFD to ignore pulses that result from instrumental noise and allows pulses originating from ion impacts to be converted to NIM output pulses. The threshold can be adjusted from -5 mV up to values greater than -1 V.

Figure 3-7 shows the signal processing schematic for the LMIS cluster SIMS instrument. The TDC is the stopwatch of ToF experiments. When a start signal is sent to the TDC, either as a trigger from the pulse generator for a ToF measurement for the primary ions or from the CFD which is coupled to the start detector, it will accept all stops correlated with that start for a user-defined amount of time. This information is then passed to a personal computer (PC) for storage and analysis. The TDC used for primary ion ToF analysis is a TOF2 (Schmidt Instruments, USA) which has a resolution of 2.5 ns per channel. This TDC sends its information to the PC in such a manner that the data is summed together and the end result is a histogram of all events. The TDC used for secondary ion analysis is a CTN-M4 manufactured by the Institut de Physique Nucleaire in Orsay, FR. This TDC can be operated in two different modes; program 6 or 8. Program 6 operates in a similar manner as the TOF2, in which it submits the data collected to the PC in a summed format. This program may be preferred since the processing power and memory requirements of the PC are minimized, information gathered as individual events is lost and coincidental ion interrogation of the data is impossible. Program 8 permits full exploitation of data collected in the event-by-event mode. Each event from up to eight distinct stop detectors are stored separately from one another allowing data to be extracted from the matrix in several different ways.

CHAPTER IV

MULTI-ANODE DETECTOR

The use of keV polyatomic/cluster projectiles and their propensity for enhanced secondary ion yield has been noted previously. Coincidental emission of two isobaric ions cannot be detected in a time-of-flight mass spectrometer utilizing pulse counting electronics. Rickman et al. have shown that two chemically similar secondary ions can be detected from a single primary cluster impact [25]. A 50:50 homogeneous mixture of Phe and d₈-Phe was deposited onto a metallic sample support. The target was bombarded with various Au_n⁺ (n = 1-4) ranging in energies from 17 keV to 56 keV. The secondary ion yield of [Phe-H]⁻ resulting from 56 keV Au₃ bombardment was 0.044. The coincidental ion yield of Phe and d₈-Phe was 0.0023. In other words one out of every 444 primary projectiles results in a simultaneous emission/detection of Phe and d₈-Phe secondary ions. The coincidental ion yield for Phe and d₈-Phe resulting from 136 keV Au₄₀₀ bombardment is 0.12, more than 50-times more likely than with Au₃.

The first published data regarding the secondary ion multiplicity resulting from Au₄₀₀ impacts on a Phe target show that the most probable desorption event results in the detection of eight secondary ions as compared to a “null-event”, an event where no secondary ions are detected, for the less complex Au_n (n = 1-9) clusters [65,66]. Figures 4-1 and 4-2 show the probability of detecting 10 secondary ions per event from a Phe target for Au₄₀₀ is 0.06, while the probability for an equally productive event from the same target using Au₉ as a projectile is 3×10^{-5} . The multiplicity plot for a sample

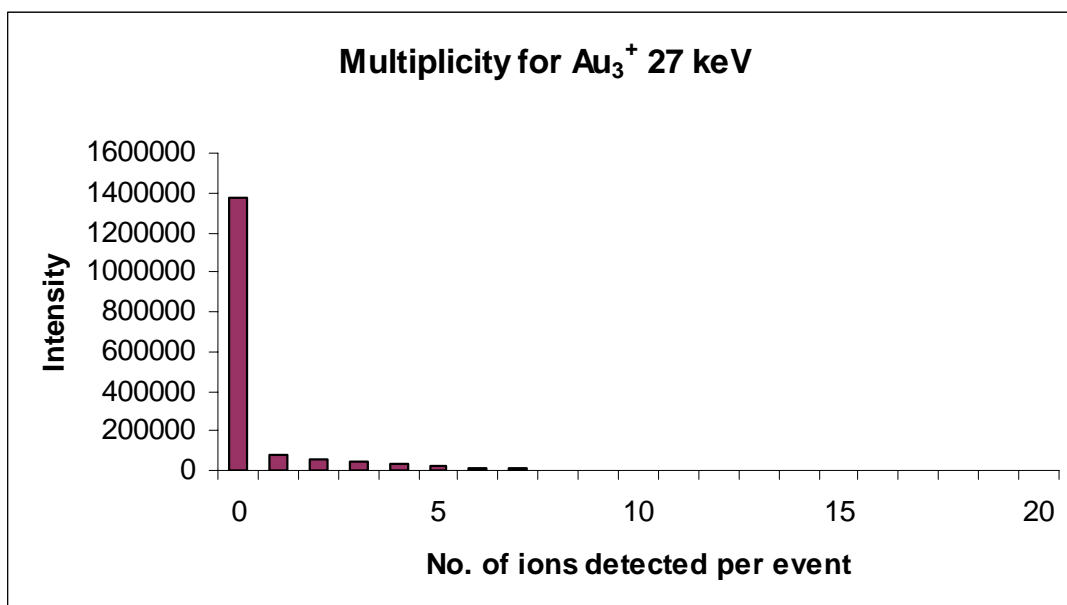


Figure 4-1. Multiplicity report for phenylalanine bombarded by 27 keV Au₃⁺.

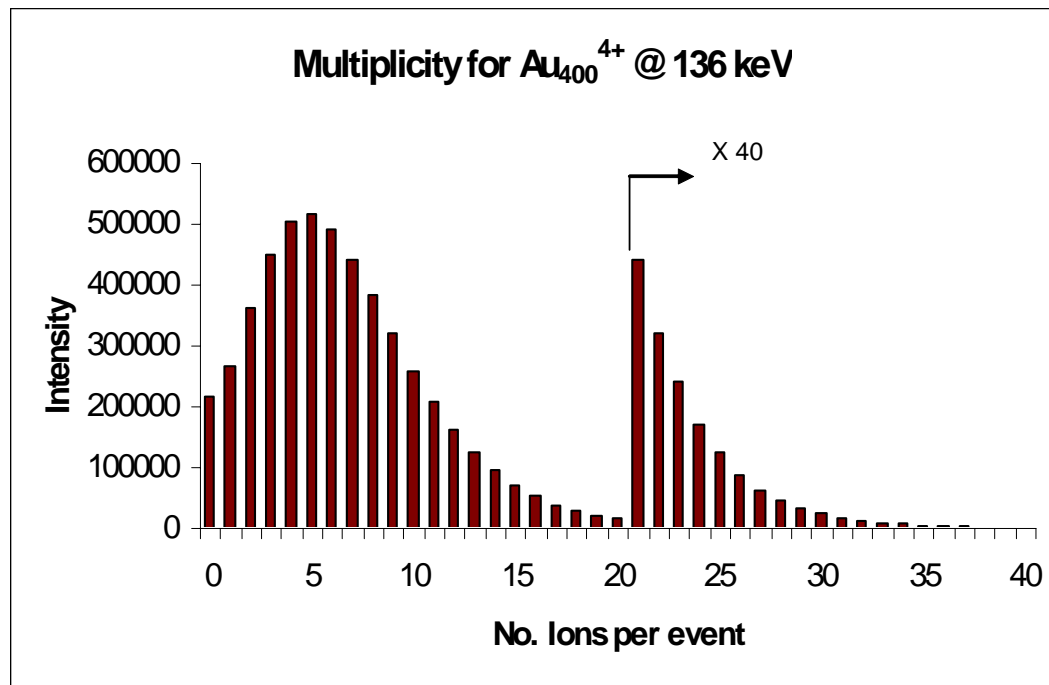


Figure 4-2. Multiplicity report for phenylalanine bombarded by 136 keV Au₄₀₀⁴⁺.

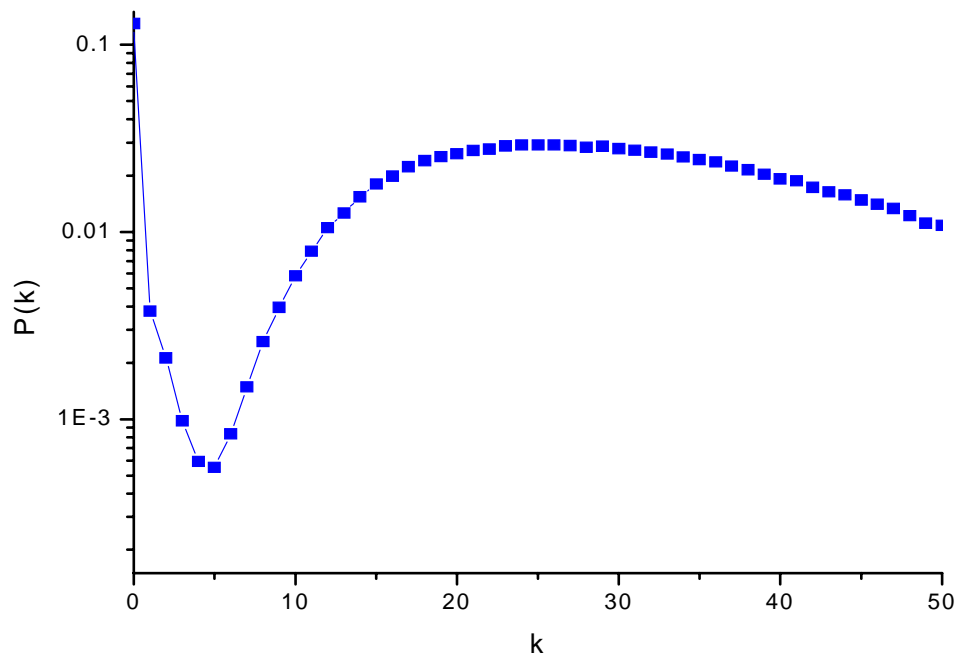


Figure 4-3. Multiplicity report for CsI bombarded by 136 keV Au_{400}^{4+} .
(Relative error $< \pm 10\%$)

which has a higher ionization probability, such as CsI, indicates that the most probable event is one where 30 secondary ions are detected per primary ion impact, as shown in figure 4-3. To fully take advantage of the enhanced secondary ion emission resulting from these massive clusters, versus much smaller poly atomic clusters, a new detection scheme needed to be developed. There are two basic designs that are capable of detecting multiple secondary ions of the same m/z .

One approach is to use an electronics package which makes it possible to use a single anode to detect the simultaneous arrival of secondary ions. This technique uses an electron multiplier such as a set of microchannel plates and a single anode, as described by Deconihout et al. [67]. The output pulse from the microchannel plates is integrated and recorded in its time bin. If two (or three) ions arrive at the detector simultaneously the charge measured at the anode is two (or three) fold greater than that of a single ion and is recorded as the appropriate number of ions in that particular time bin by use of an analog-to-digital converter. There are several drawbacks to this method of secondary ion detection. First, the output/gain from a set of microchannel plates is controlled by two parameters; the bias across the microchannel plates and impact velocity of the secondary particle on an active channel. In a time-of-flight measurement all secondary ions have the same nominal kinetic energy therefore, ions of a greater m/z will have a lower velocity. Hence, secondary ions of a higher m/z will have lower probability of generating secondary electrons resulting in a lower charge output of the MCP for these ions [63]. This situation requires the charge output at each m/z be calibrated in order to obtain an accurate count of similar m/z ions. Utilizing post-source acceleration or

accelerating the secondary ions to higher initial energy can negate this problem.

Microchannel plate performance also degrades over time and usage [63]. This requires that the output of the microchannel plates be calibrated periodically at each m/z over the mass range being examined. A third drawback of this analog method of measurement regards the output current of the MCP or dynode. The output current is converted and amplified to a voltage signal. The inherent noise from the secondary electron multiplier is also recorded and there is no way to discriminate against it. Unlike in pulse counting, where the use of a discriminator is able to filter out this noise [64].

A second method for the detection of identical ions is the use of separate and independent ion detectors. The use of multiple electron multipliers such as those incorporated in magnetic sector instruments such as the Finnigan MAT-261, which is used for elemental isotopic measurements, for the detection of similar m/z secondary ions [68]. This method provides the user with the added expense of maintaining several electron multipliers along with the additional power supplies required to operate them. In addition to these added costs comes the logistics to be able to place them close enough to one another where the dead area between detectors is minimized. The use of a single electron multiplier with multiple anodes, each isolated from the others, overcomes both of these problems since the distance between detectors is limited by the manufacturing process incorporated in building the anodes [69]. Multi-anode detectors have been shown to be effective in instruments that utilize mass spectrometers as a means of ion identification, such as tomographic atom probes [67]. A 256-anode

detector was used in the identification of Au_{400}^{4+} [28]. A 4-anode detector was used to increase the dynamic range of an ESI-ToF-MS by an order of four [70].

The use of a multi-anode detector in conjunction with the current pulse counting electronics allows for single ion counting per anode [69]. The multi-anode detector currently in use on the LMIS cluster SIMS instrument is of an 8-anode design and shown in figure 4-4. It is manufactured from a 1/16" (1.56 mm) thick fiberglass circuit board that is covered by 0.014" (0.336 mm) copper layer that is attached using glue. 0.014" copper corresponds to 1 oz. of copper per square foot of circuit board. The external dimension of the anode assembly is approximately 56.2 mm square. The active area of the anode has a diameter of 42.75 mm, corresponding to a total anode area of 5741 mm². There is an area inside the active circumference that is inactive. The area at the center of the anodes has a diameter 5.59 mm and each anode is separated by 2.02 mm on each side. This combined dead area equals 398 mm² therefore, giving the multi-anode detector a net active area of 5343 mm² or 93.1% active area inside its active circumference.

The multi-anode board was manufactured locally in the dimensions noted above. The layout was printed onto velum paper (UV transparent) using a laser printer which uses ink that is UV opaque. The copper coated fiberglass board is pre-coated with a light sensitive resist. The board and negative are taped together and placed in the UV exposure chamber and exposed to UV light for a period of one-minute. The board is then developed for approximately two-minutes prior to etching with hot ferric chloride

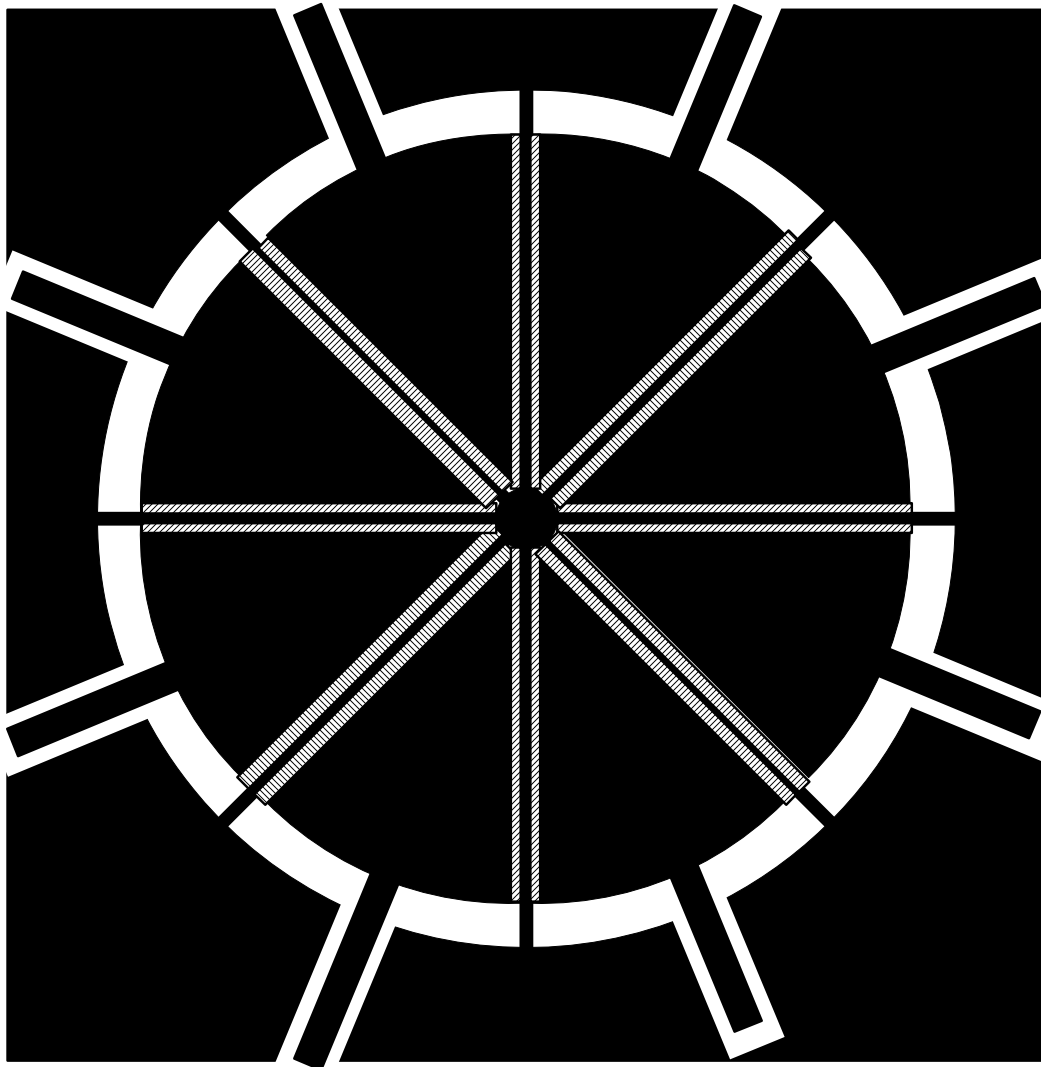


Figure 4-4. Diagram of the eight-anode detector. The area in black is where copper plating is located on the assembly. The white area is where the fiberglass board is exposed. The areas marked with dashed lines are where the fiberglass insulator was removed.

solution. After washing and drying the board it is then electroplated with gold to inhibit corrosion.

The entire multi-anode assembly is placed in back of two microchannel plates (MCP) as shown in Figure 4-5. The distance from the grid to the front MCP is 4 mm. The bias on the front of this MCP is between -2200 and -2400 VDC. The first MCP and second MCP are separated using a 0.60 mm (0.025") thick stainless steel ring. The back of the first MCP and the front of the second MCP are at the same potential, approximately -1400 VDC. The back of the second MCP has an approximate potential of -400 VDC applied and is 2.8 mm from the anodes which are at ground (0 VDC). The value of R1 is 220 k Ω and is used to maintain the anode at ground when the anode's output is not directly connected to the CFD.

As stated earlier each anode is separated by 2 mm on each side from the adjacent anodes. This area includes three regions: two where the copper and fiberglass board have been removed and a region where the copper layer was allowed to remain and is connected directly to the instrument's grounding cable. Each region is approximately 0.67 mm thick. The fiberglass was removed in the areas where the copper was etched away under the active area of the MCP stack. This is done to prevent charging of the insulator between the anodes. Any electrons that pass through this region of the multi-anode assembly are collected via a second anode that is directly coupled to the instrument's grounding cable. The copper region between the anodes is connected to the instrument's ground and is responsible for minimizing crosstalk between adjacent anodes. Crosstalk can occur when there is capacitive coupling between anodes. Any

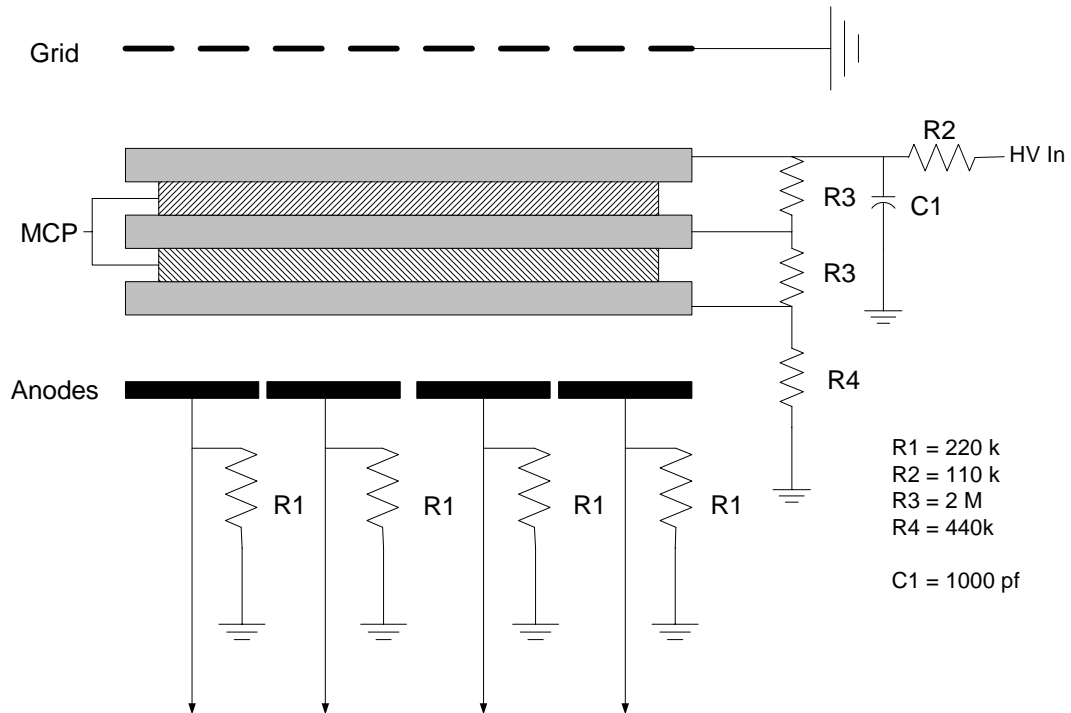


Figure 4-5. Schematic representation of the multi-anode assembly.

signal resulting from capacitive coupling is shunted to ground via the grounded conductor between adjacent anodes.

To test crosstalk a mask was placed between the back MCP and the eight active anodes. The mask shunted the output of the MCP assembly above the even numbered anodes (0, 2, 4 and 6) directly to ground while the output of the MCP's to the odd numbered anodes (1, 3, 5 and 7) was uninterrupted. To calculate percent crosstalk for a specific peak, the number of counts under that peak, on a blanked anode, is divided by the number counts for the same peak on both adjacent anodes and multiplied by 100. Crosstalk levels below 1.0% were considered acceptable. To ensure that all anodes were equally tested, we utilized fission fragments from a Cf fission foil to stochastically bombard a target's surface. The sample target was vapor deposited d_8 -phe on a metal substrate. The average crosstalk for the M-H- peak for all four masked was an average of 0.019%, well below the self-imposed one-percent limit.

The effectiveness of the multi-anode detector was examined with respect to its ability is to enhance the dynamic range of secondary ion detection. Isobaric secondary ion multiplicities were measured. Radial distributions of secondary ions were also examined.

As noted to previously, the secondary ion yields for I^- and $(CsI)I^-$ are well in excess of unity when using massive Au clusters. Comparing the secondary ion yields of I^- and $(CsI)I^-$ of 34 keV Au_5 and 136 keV Au_{400} clusters (6800 eV/atom and 340 eV/atom respectively) bombarding a CsI target the yield for I^- was 4.9 times greater for the massive cluster versus the pentatomic projectile (0.90 and 0.18 respectively) while

the yield for (CsI)I⁻ increased by 6.7 for the same two projectiles (0.88 versus 0.13) as measured on a single anode with the same detection efficiency as the 8-anode detector.

Using the multi-anode detector in conjunction with 34 keV Au₅ results in an increase of the dynamic range of detection by 10% and 8% for I⁻ and (CsI)I⁻ respectively. The secondary yields for I⁻ and (CsI)I⁻ under these bombardment conditions were 0.20 and 0.14 respectively. The secondary ion yields for I⁻ and (CsI)I⁻ when 136 keV Au₄₀₀ was used as a projectile with the multi-anode detector were 3.42 and 2.60 respectively. This corresponds to an increase in dynamic range for these secondary ions of 282% and 194% for I⁻ and (CsI)I⁻. Enhancement in dynamic range for (CsI)₂I⁻ was also recorded and is reported at 31%, the secondary ion yields were 0.55 versus 0.42 for the multi-anode and single anode detectors respectively. The increased enhancement of dynamic range is related to the multiplicity for a specific m/z secondary ion.

Multiplicity is defined as the number of secondary ions detected per primary ion impact. A multiplicity plot is one where the total number of secondary ions detected per event (k) is plotted on the x-axis and the number of events (or probability) where k-number of secondary ions are detected are plotted on the y-axis. Multiplicity can also be described in terms specific secondary ions; k_x where x is the secondary ion of interest, such as CN⁻, (CsI)I⁻. Multiplicity of secondary ion signal is directly related to the complexity of the projectile, energy of the projectile and the target being interrogated. Figure 4-6 shows a plot of the probability of detecting k number of secondary ions, from Au₅ bombardment, of a specific species per desorption event (coincidental ion emission). The most probable event with respect to I⁻ and (CsI)I⁻ is one where neither secondary ion

is detected. The probability of detecting either an Γ or $(\text{CsI})\Gamma$ is slightly more than 0.1. The probability decreases by approximately one order as the number of secondary ions of a specific m/z detected increases by one. From the graph in figure 4-6 there are no events where more than 4 $(\text{CsI})\Gamma$ ions are detected. The same can also be said for the Γ ion, while there are events where 5, 6, and 7 Γ ions are detected per event their probability is low (only one or two events in approximately 500,000 events). This low probability of coincidental ion emission explains why the dynamic range enhancement for the smaller primary ion clusters is not as great as that seen for the massive clusters.

Figure 4-7 shows a multiplicity plot for CsI utilizing 136 keV Au_{400} as primary ions. Examining the plot for both the Γ and $(\text{CsI})\Gamma$, the most noticeable attribute of these plots is that the most probable number of secondary ions per event is not zero, but instead is three for Γ and two for $(\text{CsI})\Gamma$. In other words instead of one secondary ion of a specific species detected per event, the multi-anode detector now makes it possible for up to eight secondary ions per event to be detected, allowing for secondary ion yields in excess of unity. This corresponds to the secondary ion yields of Γ and $(\text{CsI})\Gamma$ of 3.42 and 2.60 respectively. The yield for the more complex CsI cluster $(\text{CsI})_2\Gamma$ is 0.55 and examining the coincidental ion emission of this ion reveals that the most events produce no secondary ions of this complexity. The next most probable outcome is an event where one secondary ion is detected. As the complexity of SI emission increases by one, the probability decreases by approximately an order of magnitude.

Angular distributions of secondary ions have been investigated in the past [71-75]. These studies have used one of two basic schemes to measure the angular

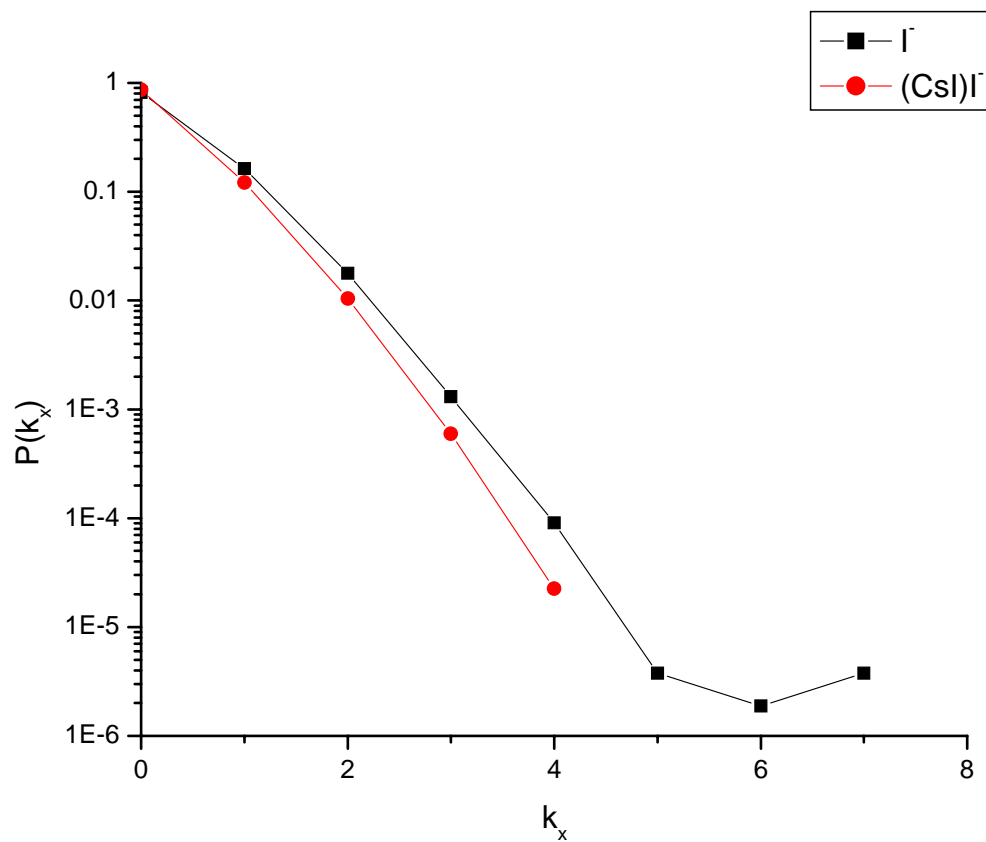


Figure 4-6. Multiplicity plot of Γ and $(\text{CsI})\Gamma$ of a CsI target bombarded with 34 keV Au_5^+ . (Relative error $< \pm 10\%$)

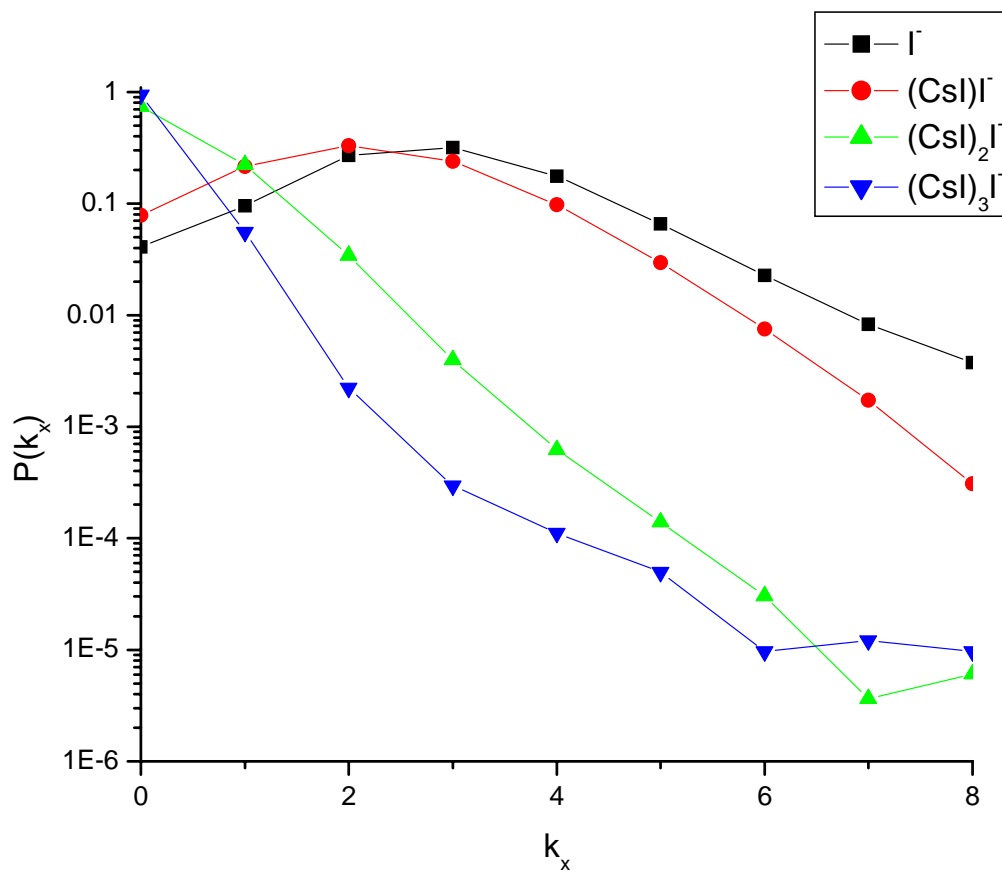


Figure 4-7. Multiplicity plot of Γ , $(\text{CsI})\Gamma$, $(\text{CsI})_2\Gamma$ and $(\text{CsI})_3\Gamma$ of a CsI target bombarded with 136 keV Au_{400}^{4+} . (Relative error $< \pm 10\%$)

distribution of secondary ions sputtered from the surface. The first is a moveable secondary ion detector which is able to rotate around the target in the plane which is comprised the primary ion beam and the ray that is normal to the target at the point where the beam strikes the target [71,72]. The angular distribution of the charged secondary ejecta is determined by rotating the detector around the target and measuring secondary ion intensities at different angles. The means of detection vary from a simple dynode, electric and magnetic sectors and quadrupole mass analyzers. A variant to this technique is one where the secondary ion detector is stationary and the target is rotated [73,74]. A second method is described by Eriksson et al., where a hemispherical series of silicon collectors are arranged around the target on which secondary ions are collected [75]. Each collector is then subjected to two separate analyses: plasma desorption mass spectrometry (PDMS) and atomic absorption (AA) to determine the amount of analyte from the target present on each collector.

The multi-anode detector can also be used to examine angular secondary ion distributions. Bouneau et al. used a 256 multipixel (multi-anode) detector to study the angular distribution of negatively charged Au and Au-cluster ions desorbed from a Au target bombarded by Au and Au-clusters [28]. There are three models used to predict the angular distributions of secondary ions resulting from energetic ions impacting on a surface as discussed in Chapter II. Figure 4-8 shows the three trajectories that can result from ion bombardment. Trajectory A is normally associated with ion desorption resulting from MeV fission fragment bombardment. Given the energy of our primary

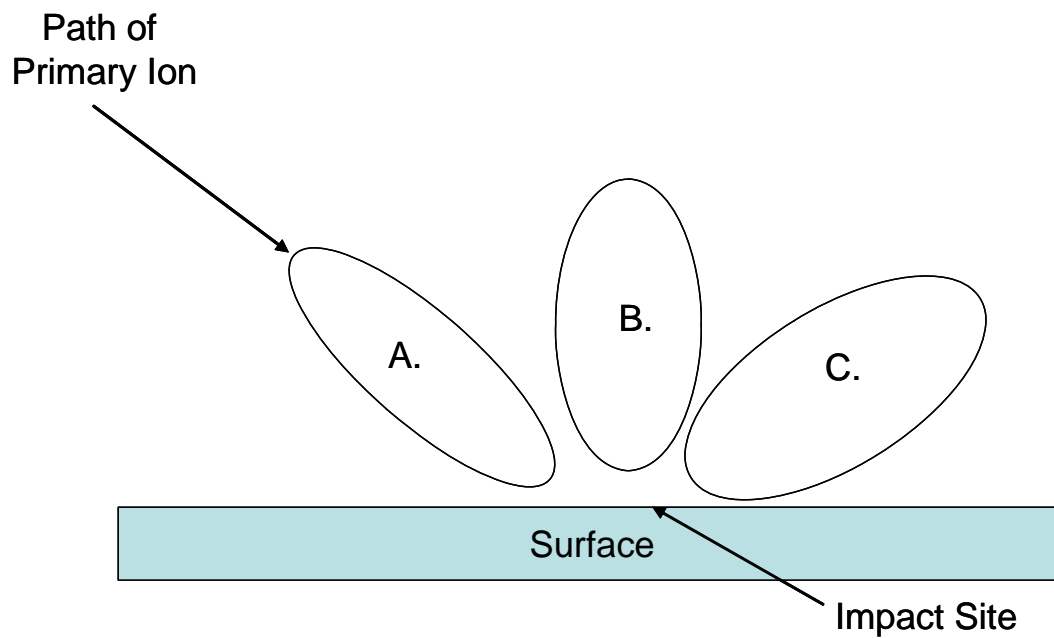


Figure 4-8. Diagram showing the three possible secondary ion angular distributions resulting from a primary ion impact: (A) trajectory resulting from phase explosion, (B) trajectory resulting from a thermal spike model and (C) trajectory resulting from a shockwave or pressure pulse model.

projectile (~ 300 eV / atom), this model seems unlikely. However, this type of emission cannot be ruled out, since little is known of these novel projectiles.

Figure 4-9 show a layout of the secondary ion leg of the instrument and the direction from which the secondary ions approach the target, also shown is a schematic representation of the eight-anode detector and location of each anode along with its identification number as viewed from the target. Plot A of figure 4-10 shows the total secondary ion distribution resulting from CsI being bombarded with 136 keV Au₄₀₀. The anodes with the highest secondary ion yields are anodes 5 and 6, while anodes 1 and 2 have the lowest secondary ion intensity. This non-symmetric distribution is attributed to the primary ions not impacting near the center of the target. By comparison when the primary ion beam is steered to a point on the target where the total secondary ion distributions are “centered” on the multi-anode assembly, the results appear symmetric (plot B). The symmetric secondary ion distributions can also be seen in figure 4-11, which are the secondary ion distributions for of the most predominant secondary ions of CsI resulting from Au₄₀₀ bombardment. The mass spectrum associated with figure 4-11 was collected when the instrumental set-up was configured so that there was an equal distribution of (CsI)₂I⁻ detected on each anode. Figure 4-12 is the same plot except with a linear scale for the secondary ion yield. The distributions show that (CsI)₂I⁻ is well centered amongst the anodes the other ions have a bias towards the upper anodes. I⁻ and (CsI)I⁻ have a bias towards right-hand anodes while H⁻ is biased towards the left. The bias of H⁻ towards the upper anodes is caused by the magnetic field used to steer the secondary electrons to the start detector. While the upwards bias of I⁻ and (CsI)I⁻ cannot

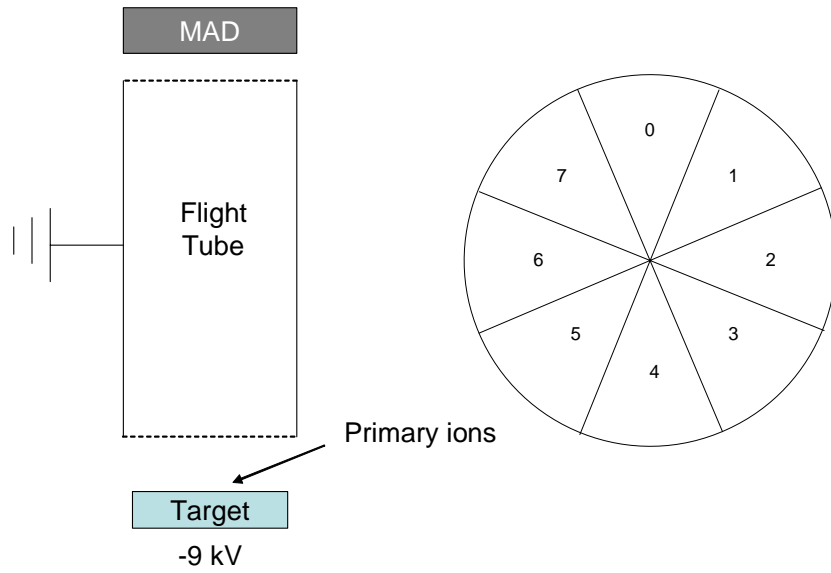


Figure 4-9. Schematic representation of the secondary ion leg of the LMIS SIMS instrument and the location and identification of each anode on the multi-anode assembly as seen from the target.

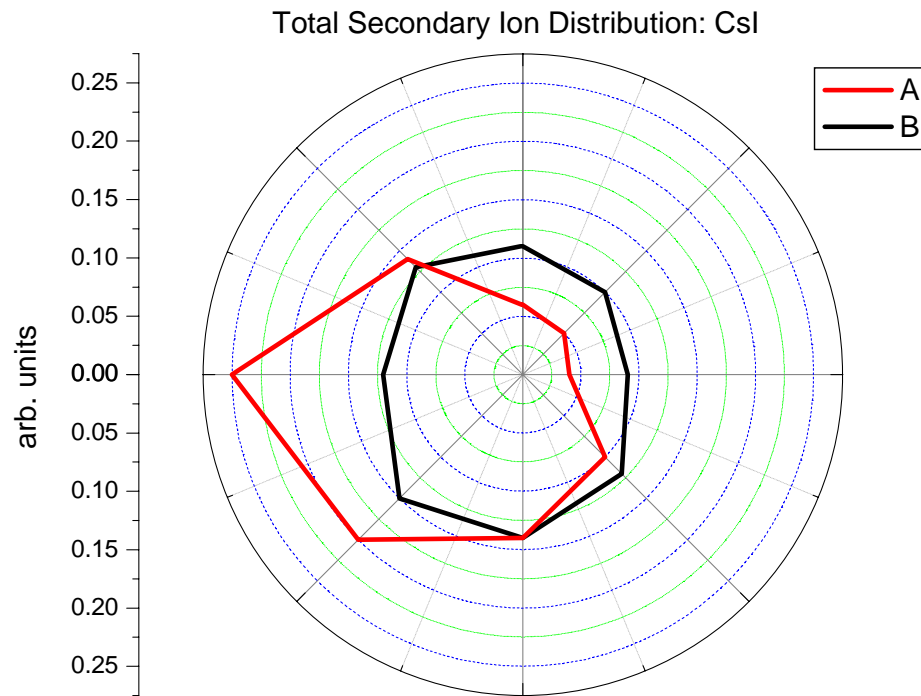


Figure 4-10. Total secondary ion distribution per anode of CsI. (A) is not centered, (B) is centered.

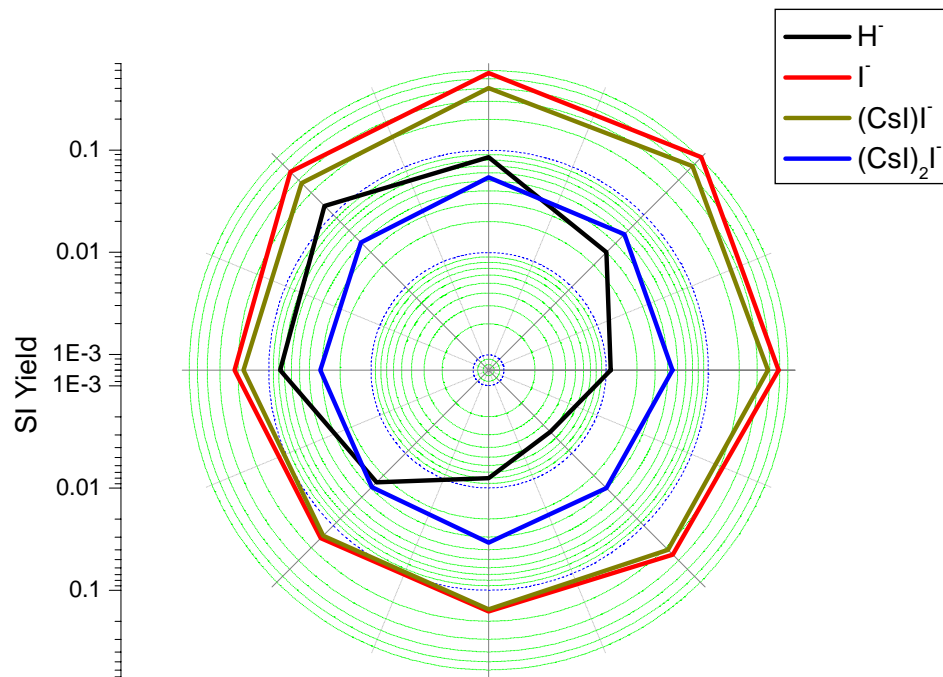


Figure 4-11. Diagram of the secondary ion yields (\log_{10} scale) of selected secondary ions detected on each anode as a result of vapor deposited CsI bombarded by Au_{400} with an energy of 136 keV.

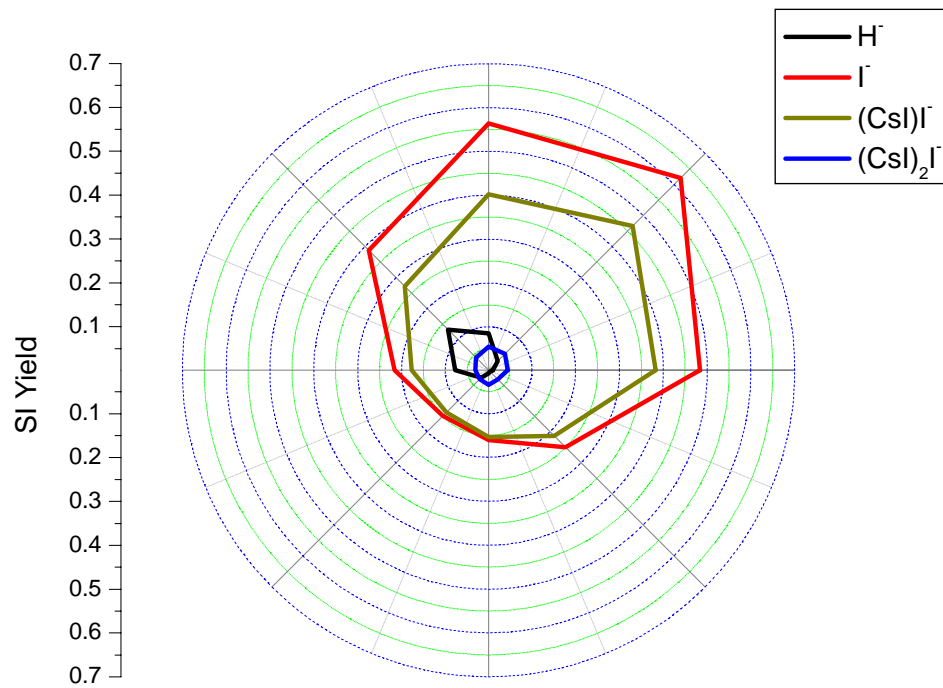


Figure 4-12. Diagram of the secondary ion yields (linear scale) of selected secondary ions detected on each anode as a result of vapor deposited CsI bombarded by Au_{400} with an energy of 136 keV.

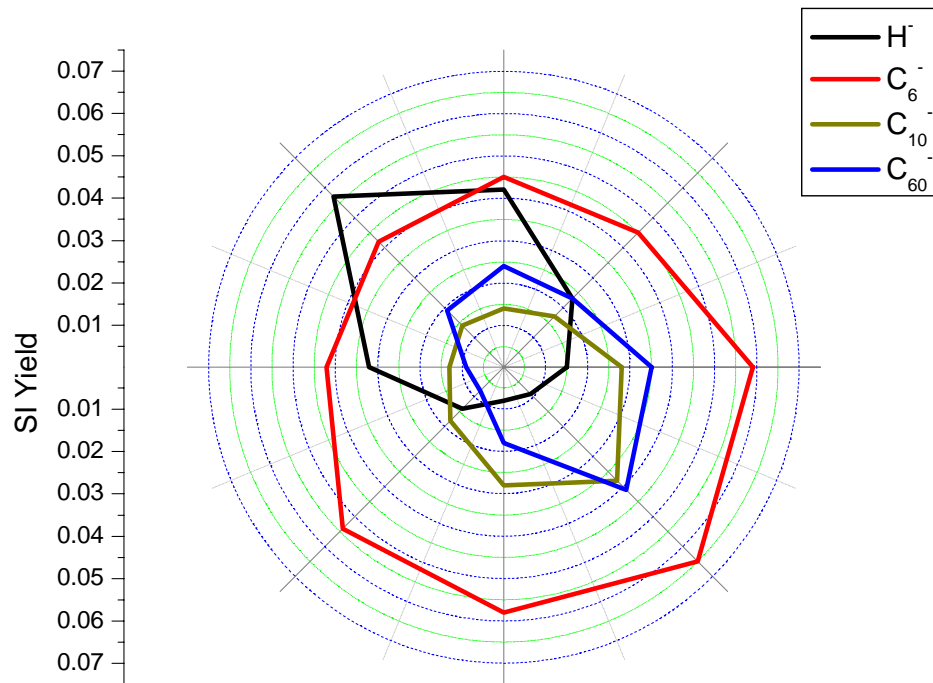


Figure 4-13. Diagram of the secondary ion yields of selected secondary ions detected on each anode as a result of vapor deposited C₆₀ bombarded by Au₄₀₀ with an energy of 136 keV.

be explained, the more significant matter is their bias towards the side of the multi-anode detector away from the primary ion beam.

Figure 4-13 shows the secondary ion distributions of H^- , C_6^- , C_{10}^- and C_{60}^- resulting from 136 keV Au_{400} bombardment of a vapor deposited C_{60} target. The instrument was set-up so that the total secondary ion signal was equal on all eight anodes. It is again apparent that the H^- has an upward bias resulting from the magnetic field used for the start detector. The C_6^- fragment ion exhibits a weak bias towards the right side of the detector, while the C_{10}^- fragment has a stronger bias towards the right. The molecular ion shows the strongest bias towards the right of the detector. All three of these secondary ions favor the side of the detector from which the primary ion beam originates.

The differences in secondary ion distributions from as determined by their relative intensities among anodes on the detector may offer some insight into their mechanism of desorption. In the instrument's current configuration the data obtained cannot be used to directly ascertain the mechanism of desorption. This limitation is a result of being unable to determine the location on the target where the secondary ions are desorbed and its correlation to the center of the detector assembly. The multi-anode detector, however, does provide relative information on the radial distribution of secondary ions in comparison to one another. Carbon cluster ions C_6^- , C_{10}^- and C_{60}^- have greater secondary ion yields on anodes 3 and 4, than the other anodes. By comparison H^- has a higher secondary ion intensity measured on anodes 6 and 7. Therefore, this

result would suggest that the mechanism for desorption of these three carbon clusters is the same.

CHAPTER V

AU-ANALYTE ADDUCTS RESULTING FROM SINGLE MASSIVE GOLD CLUSTER IMPACTS

Adduct ions in mass spectrometry were first reported in 1978 [76]. Adduct ions appear in most methods of mass spectrometry. Matrix adduct ions from matrix assisted desorption ionization for both laser and primary ion beams have been reported [77,78]. Both silver and sodium adducts have been documented with electrospray ionization of analytes [79,80]. Adduct ions can be a useful means for identification of species not readily amenable to ionization. For example, lithium attachment ionization mass spectrometry has been shown as an effective method for atmospheric sampling of various volatile organic compounds [81]. In 2004 Tempez et. al. observed both Au and Au_nCN as secondary ions utilizing Au₄₀₀ primary ions at 80 keV on a dynorphin 1-7 target immediately after irradiation of the surface is commenced [27]. These adducts, unlike the aforementioned adducts, are a direct product resulting Au atoms from the projectile and atoms from the target. These adducts are a product of a new emission process which can occur when a massive projectile impacts a surface.

When a large cluster impacts a solid, it can be scattered or implanted. For impact energies greater than 100 eV per constituent atom of the projectile implantation predominates, accompanied by intense sputtering of the impacted matter and complimentary high yield of secondary ions. The efficient sputtering/emission process is explained by a “collective effect” due to the overlap of the individual trajectories of

the impinging cluster atoms [82,83]. The same effect is also invoked to explain the increased depth of penetration of large and massive clusters [84-86].

We have observed Au adducts such as AuCN^- , AuCN_2^- and AuM^- when bombarding both organic and inorganic solids with Au_{400} carrying a kinetic energy of 340 eV/atom. The massive cluster-solid interaction results in the emission of Au-containing fragment and molecular ions from the target. Most importantly, these emissions occur at the level of single impacts. The novelty in the emission of such adducts is that they must be the result of a two-step process. The projectile's atoms must first reduce their translational energy to undergo adduct synthesis via attractive interaction. In a second step, the adduct ions must acquire translational velocity away from the surface. Such a two-step process has not been predicted theoretically nor has it been observed in molecular dynamic simulations.

Two mass spectra of histidine using Au_5 and Au_{400} respectively as primary projectiles are shown in figures 5-1(a) and 1(b). Figure 5-1a reveals the analytically significant ions of CN^- , $(\text{His-H})^-$ and $(\text{His}_2\text{-H})^-$. In comparison, the mass spectrum in figure 5-1(b) also contains the secondary ions Au^- , AuCN^- , and $\text{Au}(\text{CN})_2^-$ in addition to the secondary ions shown in figure 5-1(a).

Figure 5-2 shows two mass spectra of glycine produced from the aforementioned primary ions. Again, for the smaller clusters such as Au_5 , there are no Au^- or Au-adducts as secondary ions. However, as the complexity of the primary ion increases, e.g. for Au_{400} , the mass spectrum contains both reflected Au^- and Au-adducts as secondary ions. As is evident in Figure 5-2(b), Au-adducts are not limited to fragments of the

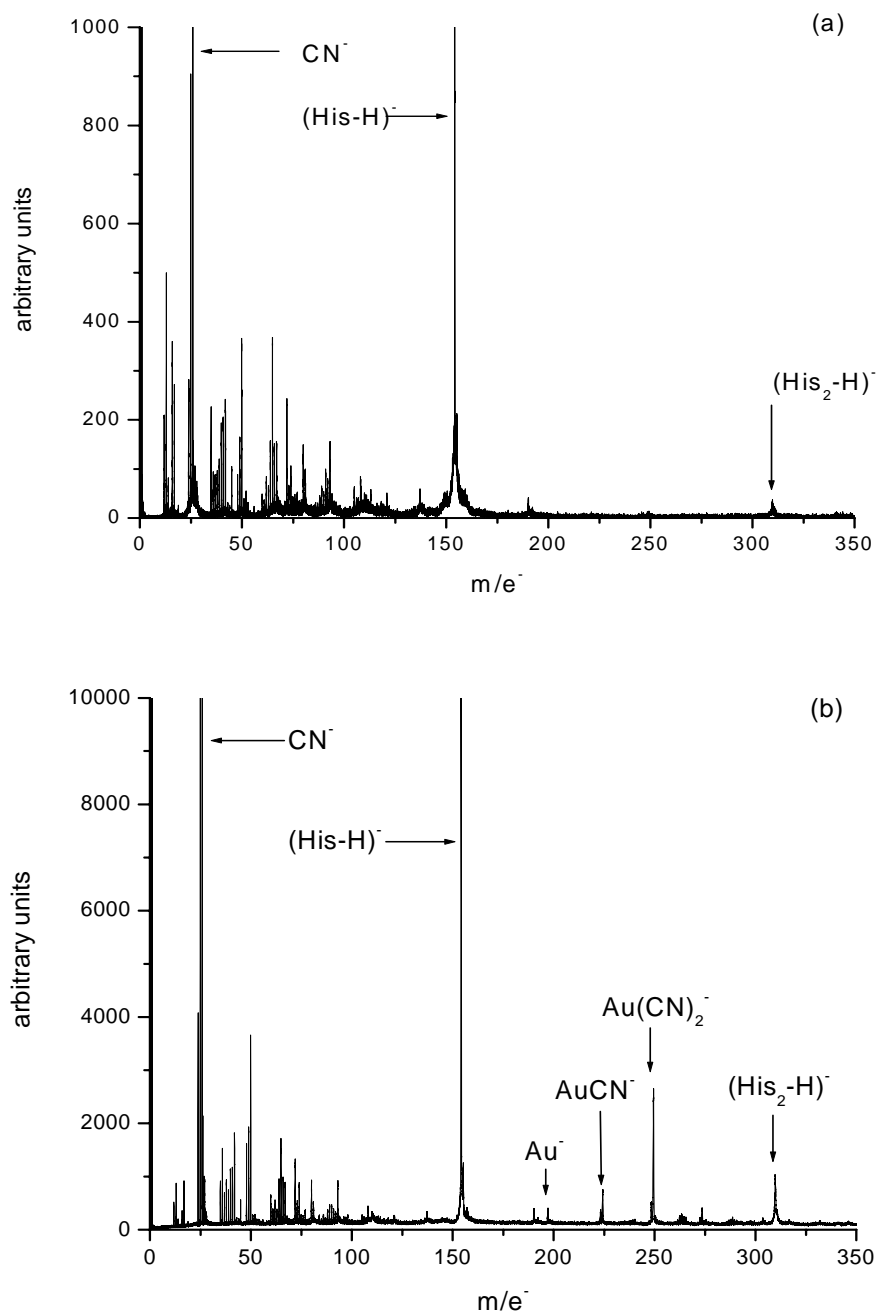


Figure 5-1. Negative secondary ion mass spectrum of histidine utilizing (a) Au_5^+ at 34 keV and (b) Au_{400}^{4+} at 136 keV as primary projectiles.

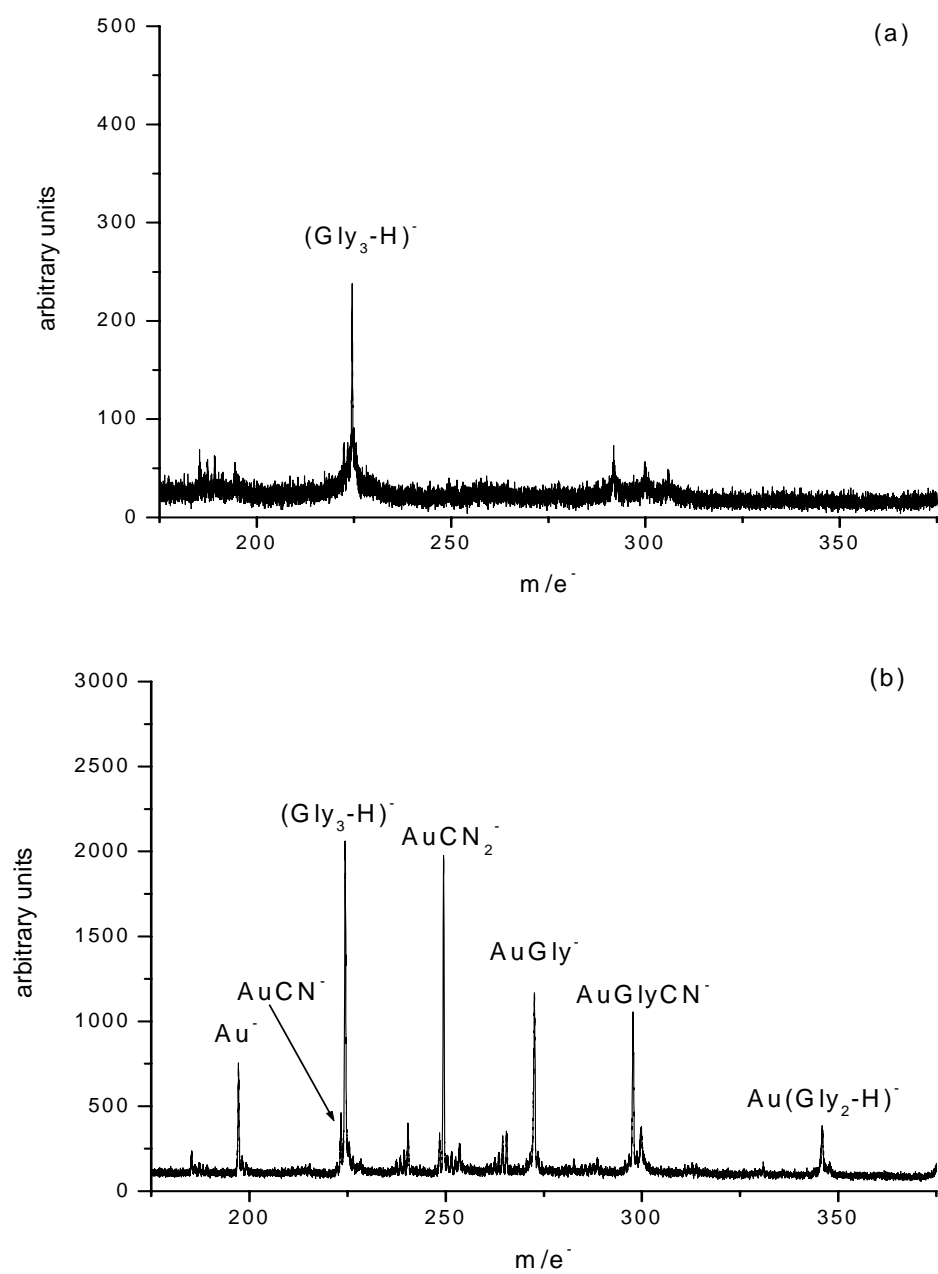


Figure 5-2. Negative secondary ion mass spectrum of glycine utilizing (a) Au_5^+ at 34 keV and (b) Au_{400}^{4+} at 136 keV as primary projectiles.

sample target. Au-adduct secondary ions of varying complexity, $\text{Au}(\text{CN})_2^-$, AuGly^- , $\text{Au}(\text{Gly})\text{CN}^-$ and $\text{Au}(\text{Gly}_2\text{-H})^-$ are observed. Table 5-1 lists the secondary ion yields of Au^- and several Au-adducts generated from organic and inorganic samples.

It may be hypothesized that the emission of adducts is a result of continuous bombardment, where over time the implanted gold can be subjected to the sputtering process initiated by subsequent projectiles; however, this is not the case. The mass spectrum, shown in figure 5-3, was obtained with $\sim 3,000$ Au_{400} projectiles over a 1 mm diameter area from a fresh CsI target. We clearly observe the presence of Au^- , AuI^- , AuI_2^- and AuCsI^- . Examining the yields of Au , AuI_2^- and AuCsI^- , for different numbers of projectiles, shows that they remain relatively constant as a function of implanted gold (table 5-2).

Our experimental data suggest a new type of emission phenomenon i.e., *in situ* emission of adducts generated from the atoms of the projectile and molecules, fragments and atoms from the target. *In situ* emission means that each single impact of a Au cluster, which is a donor of atoms and energy, initiates the synthesis of Au-containing adducts and their emission. The Au_{400} , impacting the surface, has a translational velocity corresponding to the kinetic energy of 340 eV/atom. The emission of adducts could be a two-step process: First, the atoms of the projectile must reduce their translational energies (deceleration) to become involved in the process of adduct synthesis (attractive interaction). Second, the formed adducts must acquire velocity upward or away from the surface. An immediate question regards the condition of the projectile atoms during and after the time of the implantation. Does the projectile

Table 5-1. Secondary ion yields of selected secondary ions utilizing Au_{400}^{4+} primary ions with impact energies of 136 keV. (Relative error $< \pm 8\%$ for amino acid yields, $< \pm 10\%$ for CsI)

	Phe	Gly	His	CsI	
CN	0.51	0.71	1.1	3.45	I
M-H	0.77	1.13	0.83	2.73	(CsI)I
Au	0.035	0.07	0.044	0.168	Au
AuCN	0.023	0.043	0.035	0.115	AuI
Au(CN)₂	0.024	0.13	0.176	0.162	AuCsI
Au(M)	0.031	0.103	0.05	0.182	AuI₂
Au(M₂-H)	0.008	0.105	0.034		
AuMCN	0.014	0.085	0.085		

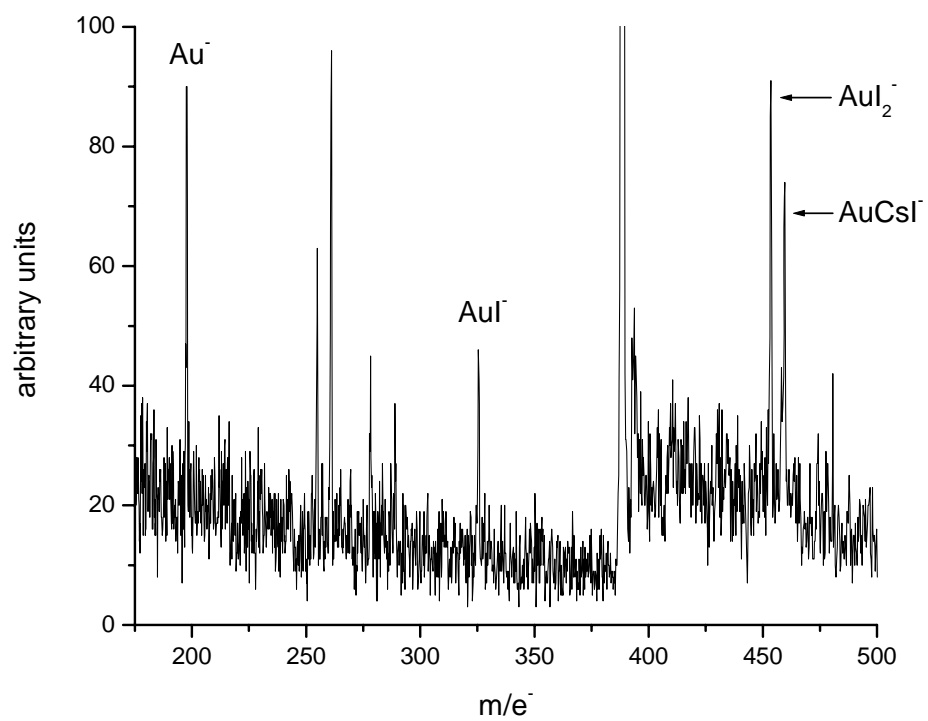


Figure 5-3. Negative secondary ion mass spectrum of CsI utilizing 3071 Au₄₀₀⁴⁺ projectiles at 136 keV.

Table 5-2. Secondary ion yields of selected Au⁻ and Au-adduct peaks of CsI bombarded by Au₄₀₀⁴⁺ at 136 keV as a function of number of primary ion impacts.

No. of events	AuI2	AuCsI	Au
3071	0.149	0.125	0.129
5075	0.153	0.127	0.124
10119	0.162	0.121	0.131
95593	0.156	0.126	0.131

disintegrate (atomize) in the target or does it survive implantation? We consider here a possible mechanism of adduct emission in the case of a light atom target. The interaction of Au₄₀₀ with a graphite target has been examined for the energies ~100 eV/atom [87,88]. Transmission electron spectroscopy and electron diffraction show that the Au₄₀₀ projectiles are implanted virtually intact as nanoparticles [88]. This observation is in agreement with a MD simulation which shows that 100 eV/atom Au₄₀₂ particle stops after ~ 2ps producing a cylindrical crater with the gold cluster implanted at the bottom of this graphite crater [87]. In our case, 340 eV/atom Au₄₀₀ on organic or carbon targets, the scenario of the projectile impact should be similar except for the condition of the Au cluster after impact. One can speculate that, in our case, the larger initial energy causes the partial disintegrations of the Au cluster before stopping. Thus, within a few ps, the projectile generates a crater via displacement of the target atoms. The walls of the crater are amorphized and contain destroyed molecules. The Au cluster residue at the bottom of the crater contains a high density of vibrational energy [87]. This energy could be sufficient to initiate chemical reactions between surviving molecules, near the bottom of crater, and implanted Au cluster residue. The result of these reactions is the synthesis of adducts of the types Au(M), Au(M₂-H), where M indicates the intact molecule. Another possible mechanism of adduct synthesis is a recombination of Au atoms with atoms and small fragments from the target. This process may occur in a high atom/fragment density volume, which may be expected in the final phase of crater formation. This mechanism should be effective for the production of small adducts such as AuCN⁻ and AuI⁻. The most difficult question

concerns the mechanism leading to emission of synthesized adducts. Indeed, synthesis takes time, and during that time the energy dissipates from the impacted volume in which adduct synthesis is supposed to occur thus depriving the adducts of translational energy. The initial shock wave resulting from the primary ion impact propagates from the surface toward the bulk of the target and cannot be recognized as a stimulator for the emission of adduct ions. A possible source of energy which could drive their emission is the one accumulated within the stressed matter (walls and bottom of the cylindrical crater). The collapsing of the crater, due to this accumulated energy, could initiate nano-shock waves which are propagated toward the target surface [89].

While the Au-adducts have significantly lower secondary ion yields than secondary ions which are not adducts, ~ an order of magnitude or more, they can prove useful in examining co-located species on the surface. As mentioned previously, the desorption volume resulting from a single primary ion impact has a radius of approximately 5 nm. As alluded to above, Au-adducts come from a smaller area on the surface, i.e. the crater formed by the Au cluster. This crater and the Au residue at its bottom should have a diameter similar to that of the Au₄₀₀ cluster (~ 2-3 nm). Therefore, instead of secondary ion emission coming from a 10 nm diameter volume the Au-adducts are formed from a volume that is 2-3 nm in diameter.

An aqueous solution containing an equal number of moles of both CsI and Phe were deposited onto a metal substrate via liquid drop deposition. While the CsI has a greater solubility than Phe by an order of magnitude, equimolar amounts were chosen to ensure an equal amount of analyte on the surface. The goal was to examine if these two

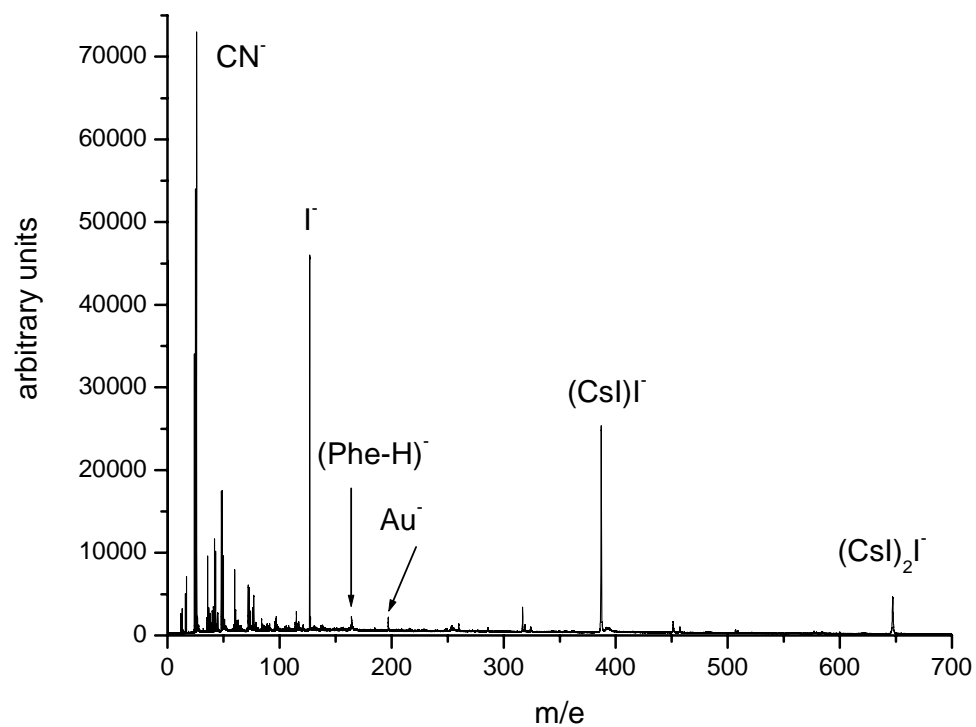


Figure 5-4. Negative secondary ion mass spectrum from a 50:50 aqueous mixture of CsI and Phe under bombardment from 136 keV Au₄₀₀⁴⁺.

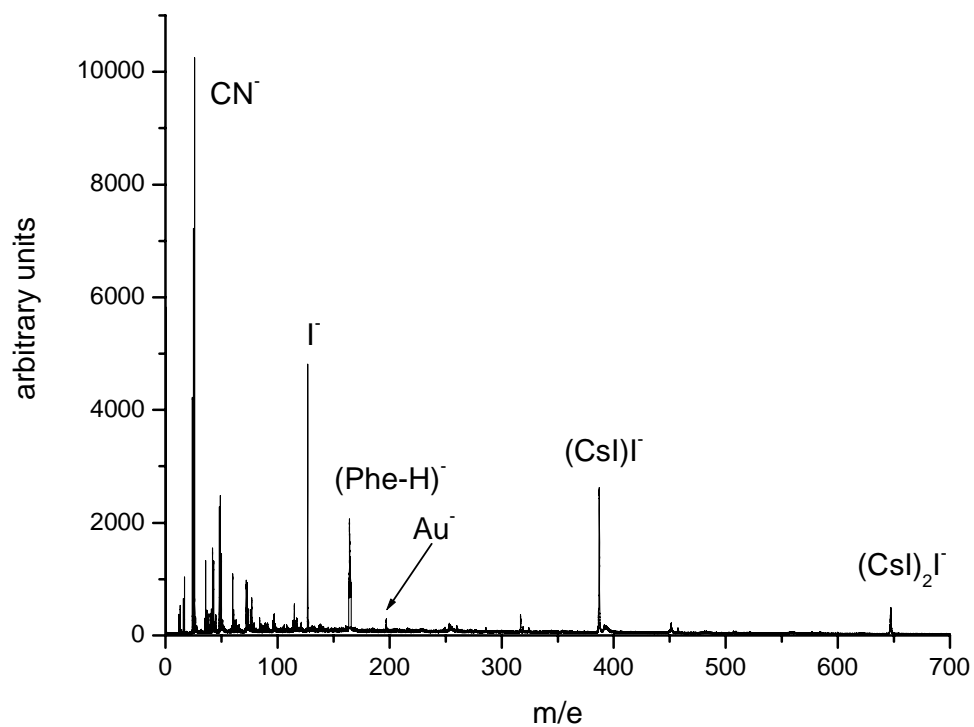


Figure 5-5. Negative secondary ion mass spectrum of all secondary ions detected in coincidence with (Phe-H)⁻ from a 50:50 aqueous mixture of CsI and Phe under bombardment from 136 keV Au₄₀₀⁴⁺.

Table 5-3. Secondary ion yields of selected negative ions detected from a CsI-Phe mix bombarded by 136 keV Au₄₀₀⁴⁺. The 4th and 5th columns contain the correlation coefficients with the secondary ion in parenthesis.

m/z	Ion Label	Yield	Q (Phe-H)	Q (AuPhe-H)	Q (Noise)
26	CN	0.45	1.4017094	1.80392157	1
127	I	0.29	0.8488064	3.10344828	0.890805
164	Phe	0.13		1.05882353	0.769231
317	Phe-I-CN or Au(M-COOH)	0.062	0.6699752	3.41555977	1.612903
361	Au(Phe-H)	0.017	0.7692308		0.637255
387	(CsI)I	0.165	0.7459207	3.42245989	0.656566
451	AuI ₂	0.015	0.974359	5.09803922	0.722222
457	AuCsI	0.001		11.7647059	
507	(CsI)I(M-COOH)	0.012	0.8974359	6.37254902	1.527778
577	Au(CsI)(M-COOH)	0.0055	1.5384615	7.48663102	
647	(CsI) ₂ I	0.039	0.591716	3.16742081	0.405983
711	Au(CsI)I ₂	0.0026		5.88235294	
370	Noise	0.012			

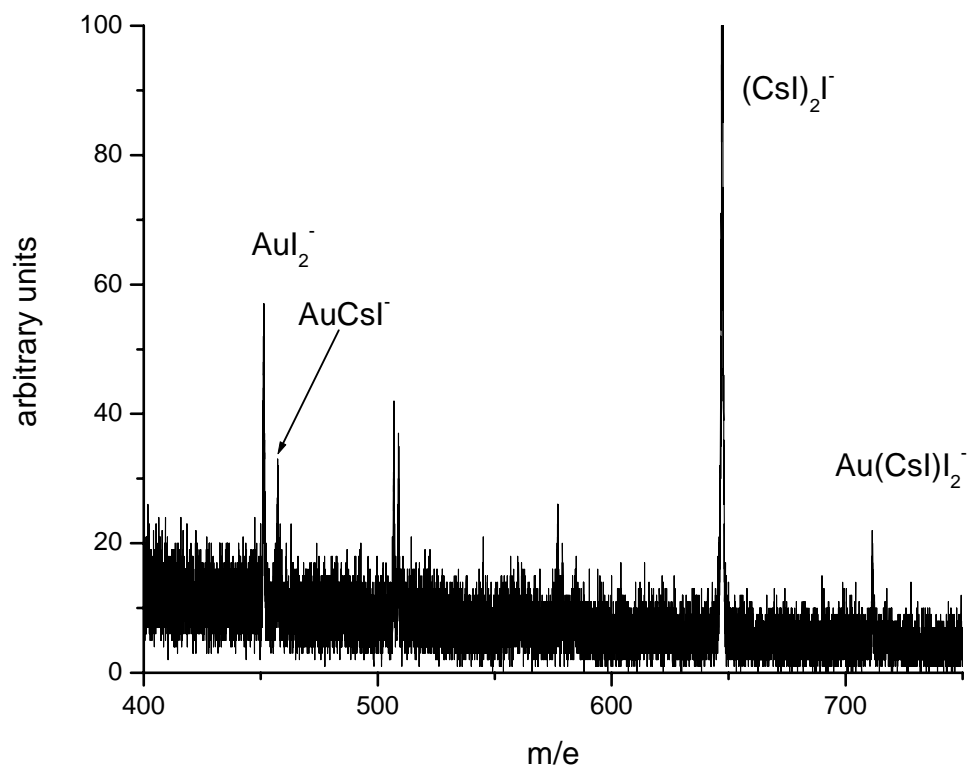


Figure 5-6. Negative secondary ion mass spectrum of all secondary ions detected in coincidence with $\text{Au}(\text{Phe-H})^-$ from a 50:50 aqueous mixture of CsI and Phe under bombardment from 136 keV Au_{400}^{4+} .

dissimilar compounds, upon precipitating out of solution, would form discrete volumes of Phe and CsI at the volume of single ion impacts or if they formed a uniform homogeneous coating. Figure 5-4 is a mass spectrum of this sample. The secondary ion yields are between 10-25 % of those from a homogeneous vapor deposited sample of each analyte. The mass spectrum in figure 5-5 shows all events when $(\text{Phe-H})^-$ ion was detected. It can be seen that for events where the Phe molecular ion was observed, there are also I^- , CsI^- and $(\text{CsI})_2\text{I}^-$ detected. These secondary ions must originate from the volume perturbed from a single Au_{400} impact, thus the two species dried on the substrate are uniformly dispersed on the surface within the spatial resolution of a single projectile impact. The presence of the secondary ion at m/z 317, $[\text{PheICN}]^-$, also presents evidence that both Phe and CsI exist in the volume desorbed by a massive cluster impact.

Correlation coefficients along with secondary ion yields for selected secondary ions are shown in table 5-3. The correlation coefficients for most secondary ions observed in coincidence with $[\text{Phe-H}]^-$ are near or below 1. Implying that the emissions of these secondary ions are either uncorrelated or anti-correlated in regards to the emission of $[\text{Phe-H}]^-$. The question remains can these two compounds form nano-domains that may be smaller than a 10 nm diameter desorption area? Since Au-adduct ions are formed from a much smaller area, looking at Au-adduct ions detected in coincidence with one another can be an effective method of determining the homogeneity of the surface.

Figure 5-6 is a mass spectrum showing all secondary ions detected in coincidence with AuPhe^- , which originates from the 2-3 nm crater. Au-adducts from CsI such as AuI_2^- , AuCsI^- , and $\text{Au}(\text{CsI})_2^-$ are also detected. Correlation coefficients for most secondary

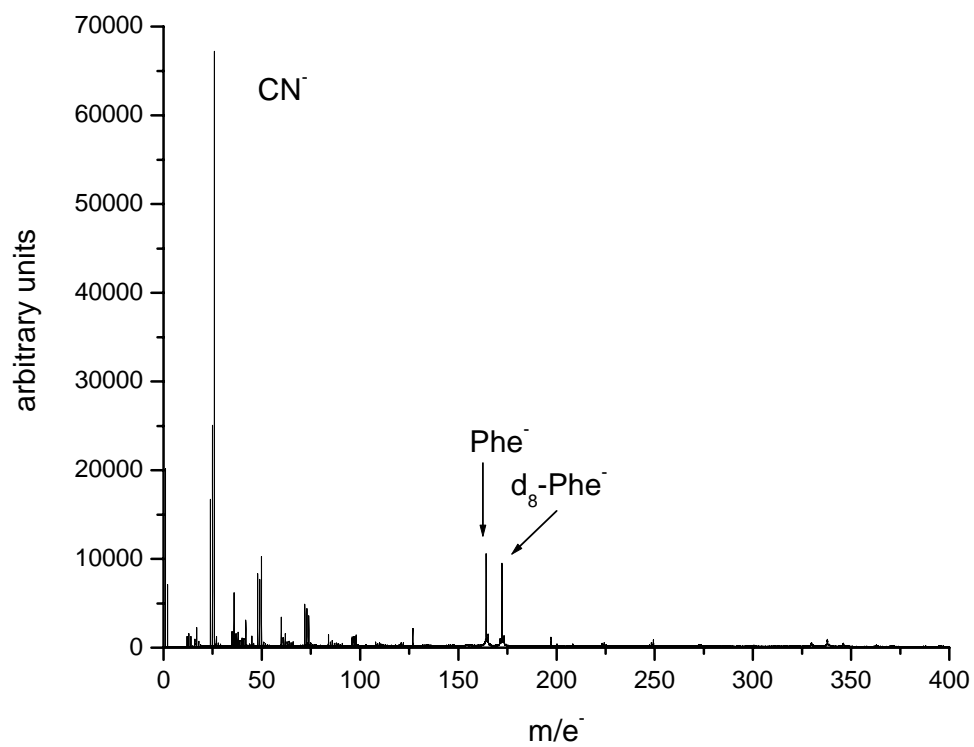


Figure 5-7. Negative secondary ion mass spectrum of a 50:50 mixture of d₈-Phe and Phe under bombardment from 136 keV Au₄₀₀⁴⁺.

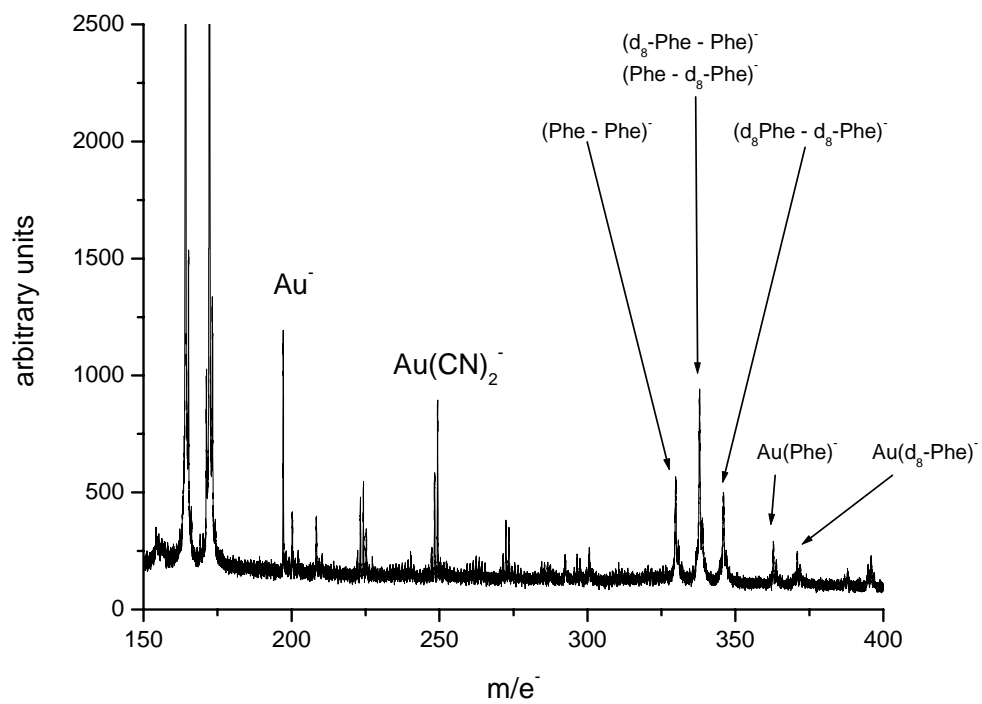


Figure 5-8. Negative secondary ion mass spectrum of a 50:50 mixture of $\text{d}_8\text{-Phe}$ and Phe under bombardment from 136 keV Au_{400}^{4+} .

ions observed in coincidence with $[\text{AuPhe-H}]^-$ were much greater than one. This would indicate that there is a strong correlation between them. In addition to looking at these coincidence ions, the emission of secondary ions with a $m/z = 577$, $[\text{Au}(\text{CsI})(\text{Phe-COOH})]^-$, clearly indicate the presence of Au-adducts containing both analytes. Therefore, when CsI and Phe are applied to a target in an aqueous solution, they form a uniform well dispersed layer on the surface and do not segregate from one another.

Interrogating a surface of Phe and d_8 -Phe by Au_{400} bombardment and examining the coincidental secondary ion emission, we are able to investigate the homogeneity of the target. Shown in figure 5-7 is a mass spectrum of Phe: d_8 -Phe. The sample was prepared by dissolving both species (of equal mole fractions) in boiling water. The solution was then refrigerated and both species precipitate out of solution in what is considered a homogeneous mixture. The Phe mixture was vacuum filtrated and washed with ethanol several times and dried at 90°C for several hours before being vapor deposited onto a metal substrate. The secondary ion yields of both species of Phe are similar, approximately 0.32.

The question arises is a true homogeneous target created during the sample preparation and vapor deposition processes. It can be shown that if one inspects the Phe/ d_8 -Phe dimer as shown in figure 5-8, the surface is a homogeneous mixture because of the binomial distribution of dimer. Also shown in figure 5-8 are the Au-adduct secondary ions with Phe and d_8 -Phe. Another approach to identifying the homogeneity of the surface is to examine coincidental secondary ion yields. Figure 5-9 shows a mass spectrum of all secondary ions detected from the Phe- d_8 -Phe target in coincidence with

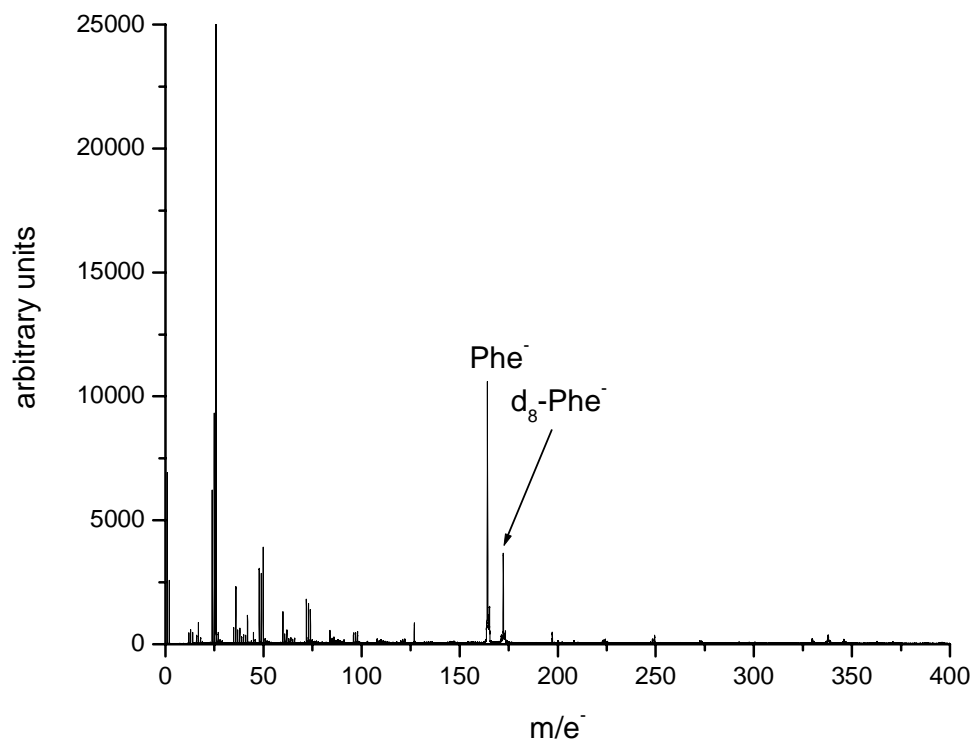


Figure 5-9. Negative secondary ion mass spectrum of all secondary ions detected in coincidence with (Phe-H)⁻ from a 50:50 mixture of d₈-Phe and Phe under bombardment from 136 keV Au₄₀₀⁴⁺.

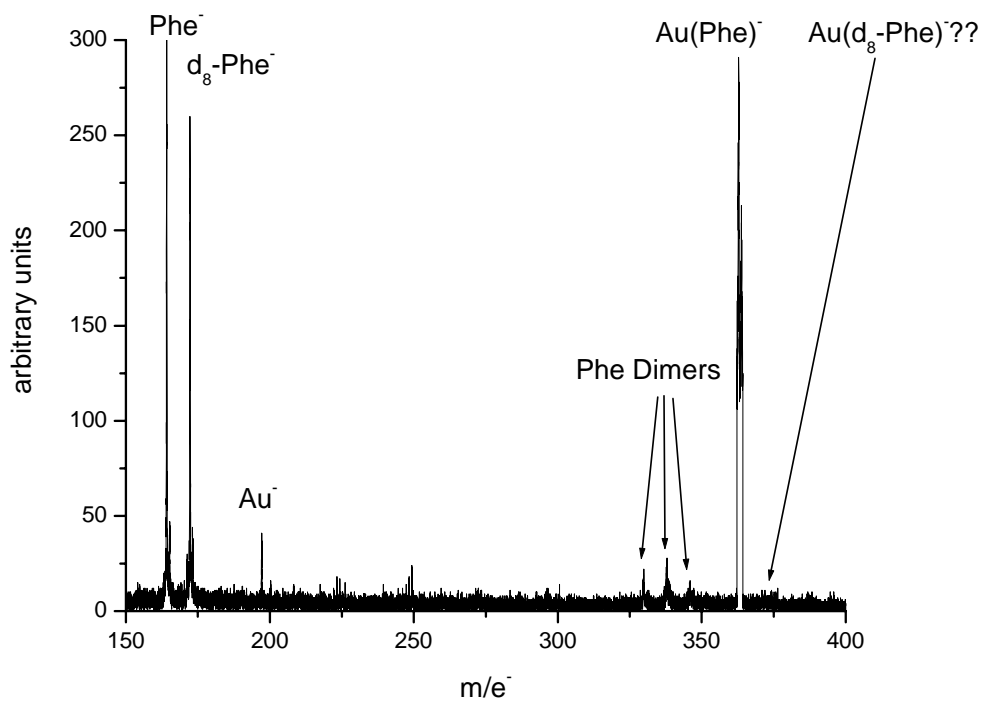


Figure 5-10. Negative secondary ion mass spectrum of all secondary ions detected in coincidence with Au(Phe-H)⁻ from a 50:50 mixture of d₈-Phe and Phe under bombardment from 136 keV Au₄₀₀⁴⁺.

Phe. The deuterated-Phe deprotonated molecule has an ion yield of 0.12. This is a clear indication that the target surface is comprised of a homogeneous mix of Phe and d_8 -Phe down to the volume of desorption, since the coincidental ion yield of d_8 -Phe is equal to the product of the secondary ion yields of Phe and d_8 -Phe ($Q = 1$). To examine if the target is homogeneous down to the 2 nm level we need to examine at coincidental ion emission of Au-adduct ions that originate from the volume of the crater. Figure 5-10 shows a mass spectrum of all secondary ions detected from m/z 150 – 400 in coincidence with Au-Phe. Due to the low secondary ion yields of the Au- M^- (0.006) we were unable to detect the Au(d_8 -Phe) $^-$ ion in coincidence with AuPhe $^-$. Assuming the emission and detection of both Au- M^- ions are independent of one another ($Q = 1$), the estimated coincidental ion yield of Au(d_8 -Phe) in coincidence with AuPhe $^-$ would be approximately 4×10^{-5} ; therefore we are unable to determine the surface homogeneity at the 2 nm level.

CHAPTER VI

CHARACTERIZATION OF SURFACE STRUCTURE

The work presented thus far has focused on the nature of secondary ion emission and on chemical information regarding collocated species on a target surface resulting from massive cluster bombardment. The question arises if these massive clusters are an efficient means for revealing chemical information from these nano-volumes? Also, can they provide insight on the physical structure near the surface of a target?

Static and dynamic SIMS have been used by investigators to examine the morphology of several different polymer blends consisting of both crystalline/semi-crystalline polymers mixed with amorphous polymers [90-93]. In these instances the investigators have been able to determine the location of the crystalline polymer in the amorphous, including its depth. However, these works have studied different polymers, one amorphous and one crystalline or similar polymers with one being labeled with deuterium and the other not labeled. These authors have not used SIMS to study the differences in secondary ion emission between crystalline and amorphous solids. Smith et al. have employed dynamic SIMS to investigate B doped Si [94]. The authors believe that the process of doping turned the crystalline Si to amorphous Si up to a depth of ~140 nm. The amorphous-crystalline interface depth was determined when appreciable charging was noticed on the sample. The charging was a result of the crystalline substrate being unable to remove the charge generated from the (+) ion beam and the (-) secondary ions generated. Kosevich et al. used fast atom bombardment (FAB) to

examine the secondary ion emission resulting from bombarding amorphous solid water (ASW) and crystalline water at different temperatures [95]. Samples were prepared by condensing de-ionized water vapor onto the target substrate which is cooled to ~ 140 K to form ASW. Bombardment of this surface resulted in a mass spectrum which consisted predominately of $(\text{H}_2\text{O})_n\text{H}^+$ ($n = 1 - 10$) ions. As the target was heated up to the point where the solid water transitions from amorphous to crystalline, the secondary ion cluster intensities greatly decreased to the point being nearly undetectable. Once the target temperature was increased to the point where the target was mostly crystalline, the $(\text{H}_2\text{O})_n\text{H}^+$ reappeared with intensities about equal to the ASW. The marked decrease in cluster formation, at the transition temperature, is due to the energy deposited from the bombarding projectiles being used by the ASW to facilitate crystalline water growth, instead of resulting in sputtering and cluster emission. The aforementioned examples have studied the morphology of crystalline/amorphous blends of polymers without examining differences in secondary ion emission characteristics. Secondary ion emission of amorphous and crystalline water was studied, but no appreciable differences were noted between these two targets. We used Au_{400}^{4+} at 136 keV to study two different compounds: graphite and α -zirconium phosphate. For each compound tested we bombarded two samples that are structurally unique but have the same stoichiometry.

Graphite in crystalline form consists of flat layers of hexagonally bonded carbon atoms which are offset from the layer above and below [96]. Bulk graphite consists of small partially ordered polycrystalline structures, only a few units in any direction, which are randomly aligned in the bulk. Pyrolytic graphite is grown by the thermal

decomposition of hydrocarbon gases which are deposited onto a heated substrate. The graphite sheets grown by this method are distributed over a range of angles and can be up to 50 degrees about the normal [96]. Annealed oriented pyrolytic graphite (AOPG) is manufactured with pyrolytic graphite at about 2700 °C under high a compressive stress that is perpendicular to the substrate [96]. This process aligns the sheets of graphite so that they vary no more than a few tenths of a degree from one another. However, the layers do not align themselves in a crystalline manner, but the density is very close to that of a single crystal, both approximately 2.2 g/cm³ [96]. By comparison, the density of the bulk graphite used in this experiment was 1.7 g/cm³.

Figures 6-1 and 6-2 show mass spectra resulting from 136 keV Au₄₀₀ bombardment of bulk graphite and AOPG respectively. Upon initial examination these two spectra appear to be similar in respect to relative peak areas. Figures 6-3 and 6-4 are spectra of the same samples except the intensity (y-axis) is normalized to the number of bombarding projectiles. The base peak ($m/e = 25, C_2H^+$) has a relative intensity of 0.016 for the bulk graphite sample versus 0.039 for the AOPG. The largest carbon cluster observed for the bulk graphite sample is C₁₇, while the largest cluster observed in the AOPG sample is C₁₉. Table 6-1 shows the secondary ion yields for carbon clusters C₃ – C₁₆ for both samples and their relative difference. The yields for the AOPG sample are between 58 – 200% greater than those observed in the bulk graphite sample (table 6-1). The question arises why do the secondary ion yields vary so much between two samples that are chemically identical but differ structurally?

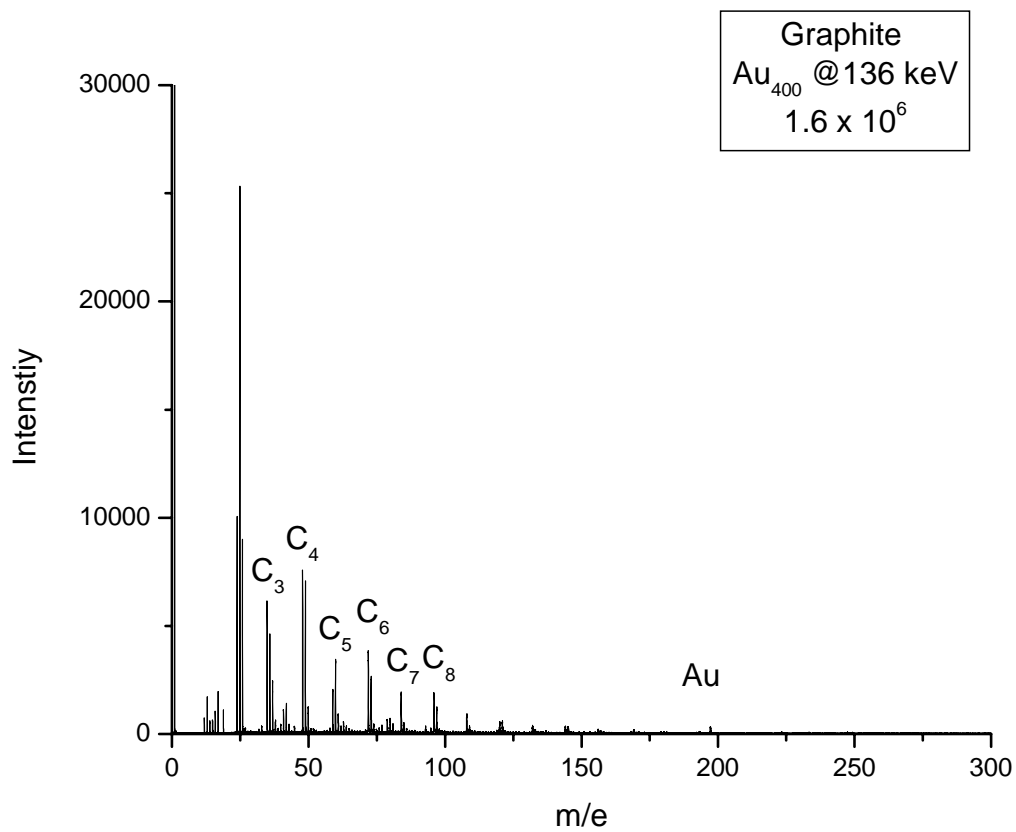


Figure 6-1. Negative secondary ion mass spectrum resulting from bombarding bulk graphite with 136 keV Au₄₀₀.

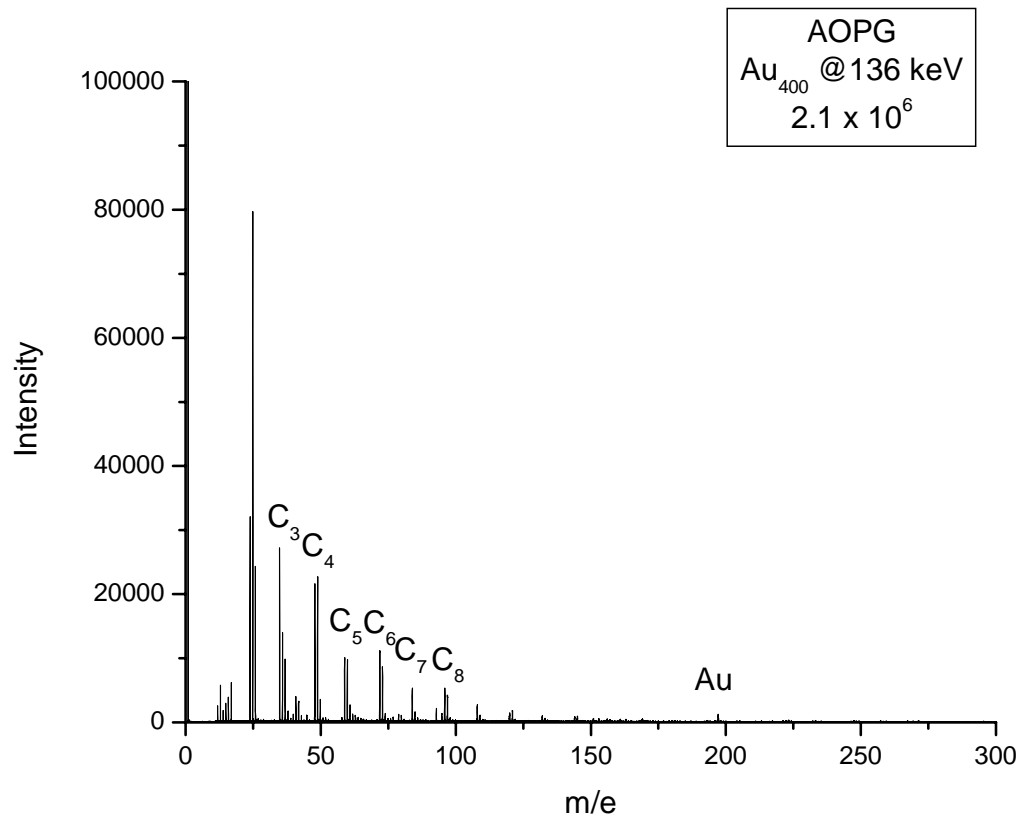


Figure 6-2. Negative secondary ion mass spectrum resulting from bombarding AOPG with 136 keV Au₄₀₀.

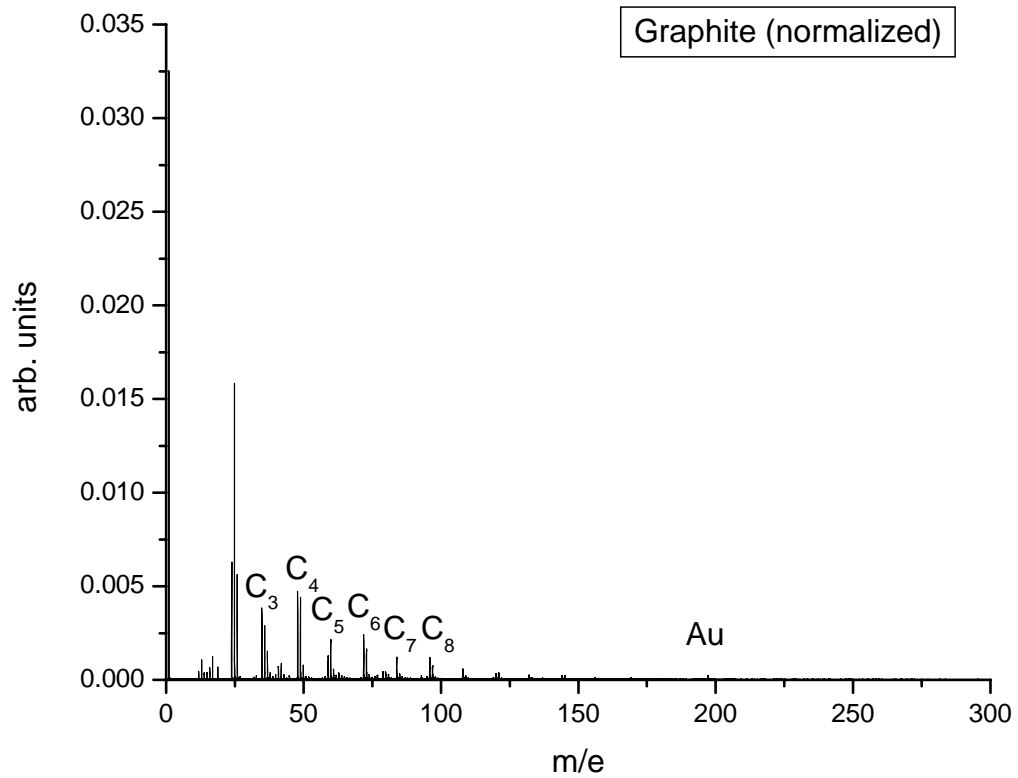


Figure 6-3. Negative secondary ion mass spectrum resulting from bombarding bulk graphite with 136 keV Au₄₀₀. Peak intensities are normalized to the number of primary projectiles.

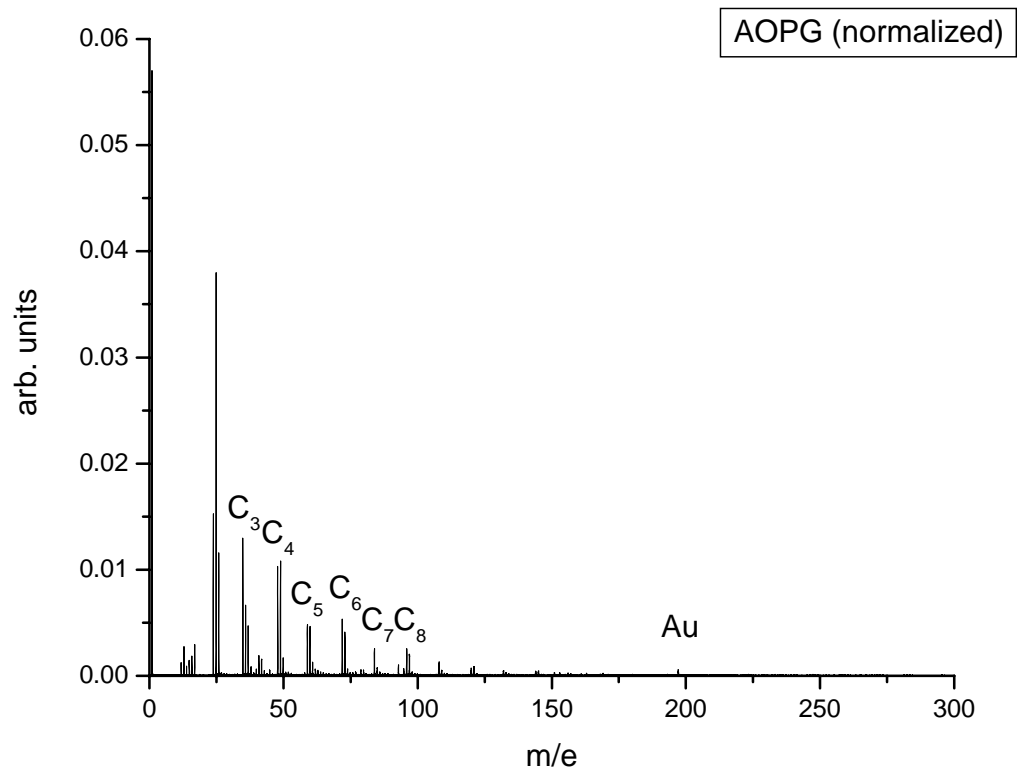


Figure 6-4. Negative secondary ion mass spectrum resulting from bombarding AOPG with 136 keV Au₄₀₀. Peak intensities are normalized to the number of primary projectiles.

Table 6-1. Secondary ion yield for C_n ($n = 3-16$) clusters and Au_n ($n = 1-3$).
(Relative error $< \pm 12\%$)

C_n	Bulk Graphite	AOPG	% Increase
3	0.050	0.089	78.0
4	0.092	0.157	70.7
5	0.053	0.084	58.5
6	0.062	0.108	74.2
7	0.036	0.059	63.9
8	0.038	0.061	60.5
9	0.022	0.039	77.3
10	0.016	0.026	62.5
11	0.011	0.018	63.6
12	0.010	0.019	90.0
13	0.007	0.012	71.4
14	0.004	0.008	100.0
15	0.003	0.006	100.0
16	0.002	0.006	200.0
Au_n			
1	0.0062	0.016	158.1
2	0.00079	0.0026	229.1
3	not observed	0.0014	n/a

A first possible explanation may be the number of secondary ions located in the desorption volume. The density of AOPG is 29% greater than that of the bulk, i.e. there are 29% more carbon atoms in the desorption volume. This increased number of potential secondary ions is not accurately reflected in the secondary ion yields of AOPG. Therefore, another explanation is required to account for this discrepancy. A possible reason for the enhanced secondary ion yields observed in the AOPG sample is the ability of the substrate to better transfer energy away from the impact crater. The shockwaves generated from the primary ion impact more efficiently propagated through-out the target. Given the tighter packing of the target ions in the denser system, there is a shorter distance the energetic atoms need to travel to transfer their kinetic energy to their neighbors and since the atoms are more compact there is a greater probability that they will interact with more of their neighboring atoms. The enhanced collision frequency in conjunction with a larger number of collisionally excited target atoms enhances the probability of secondary ion emission [37,97]. The combination of more densely packed atoms of the oriented target effectively creates a “cluster effect” enhancement of secondary ion yields resulting from the denser target

Another interesting difference between the two samples is the emission of recoiled or backscattered Au^- . Table 6-1 shows the yields for the monatomic, diatomic and triatomic Au ions from both samples resulting from 136 keV Au_{400} bombardment. The yields for Au^- and Au_2^- are 157% and 232% greater from the AOPG target than the bulk graphite target. Why are these reflected ion yields so much greater in the organized target versus the bulk? The first possible explanation is related to the density of the two

targets. Since the AOPG has a higher density than the bulk graphite sample, the projectile does not travel as far into the sample because, it encounters more carbon atoms per unit distance traveled. TRIM calculations indicate that a single Au atom with 340 eV of energy will travel 2.5 nm into a graphite target that has a density of $2.26 \text{ g}\cdot\text{cm}^{-3}$, such as the AOPG, as compared to 3.1 nm for a target which the density is $1.74 \text{ g}\cdot\text{cm}^{-3}$, the bulk graphite [98]. It is assumed that the depth a Au_{400} projectile is certainly greater than these values due to the collective effect of the entire massive cluster [99]. This is also known as the “clearing-the-way” effect [100]. Basically the leading atoms of the cluster interact with the surface atoms of the target moving them out of the way of the cluster atoms behind the leading atoms [101]. This effect reduces the stopping power of the target resulting in an increased penetration of the cluster into the target. As gold atoms are evaporated or boiled off the surface of the cluster they are closer to the surface of the AOPG target versus the bulk graphite therefore, increasing their probability for escape from the crater. Anders and Urbassek have demonstrated that a Au_{402} cluster with an energy of 100 eV/atom penetrates a well ordered graphite target to an average depth of 6 nm, as opposed to 1.6 nm for a single 100 eV Au atom [87,98]. Another possibility for the enhanced emission of remnant ions from the primary projectile could be due to the target’s structure. In the previous chapter it is referenced evidence that a Au_{400} cluster, with an energy of 100 eV/atom, remains at least partially intact in its crater [87,88]. The energy of the cluster projectiles in the experiments described here was 340 eV/atom. The energies considered here are within the same order of magnitude and we may assume that under our experimental conditions the massive cluster also remains

partially intact. Once the cluster has reached its maximum depth there are layers of graphite below the cluster that are compressed and undamaged [87]. The compressed layers then relax to their normal state by releasing the energy in the stressed layers. This release of energy provides translational velocity in the region of the crater, including the gold residue, in the direction towards the surface. The center of mass of the Au cluster reaches its maximum depth in approximately 1.5-2 ps and relaxes to its final depth after ~ 4 ps. Looking at the slope of projectile depth versus time shows a maximum at ~ 890 m/s [87]. Therefore, any Au ions formed at the surface of the vibrationally excited Au residue receive an additional boost of kinetic energy with which to escape the surface. This energy is approximately 1.6 eV/Au atom. Therefore, Au_2^- receives an additional 3.2 eV of energy. A combination of these two effects can account for the strong enhancement in secondary ion signal, of both analyte and projectile specific ions, resulting from the oriented carbon sample versus the bulk sample.

Another example of a compound that exists as an amorphous and crystalline solid is α - zirconium phosphate (α ZrP). Van Stipdonk and Rickman have studied these compounds to determine if SIMS can be used to study the structural differences between these to compounds that have the same stoichiometry [102-104]. Van Stipdonk's study included the bombardment, with MeV fission fragments from ^{252}Cf , of α ZrP samples with varying degrees of crystallinity from amorphous to fully crystalline α ZrP. Rickman studied the amorphous and fully crystalline samples under bombardment by Au_3 . Both investigators examined negative secondary ion emission. The secondary ion yields of PO_2 and PO_3 of the amorphous and crystalline samples remained constant with respect to

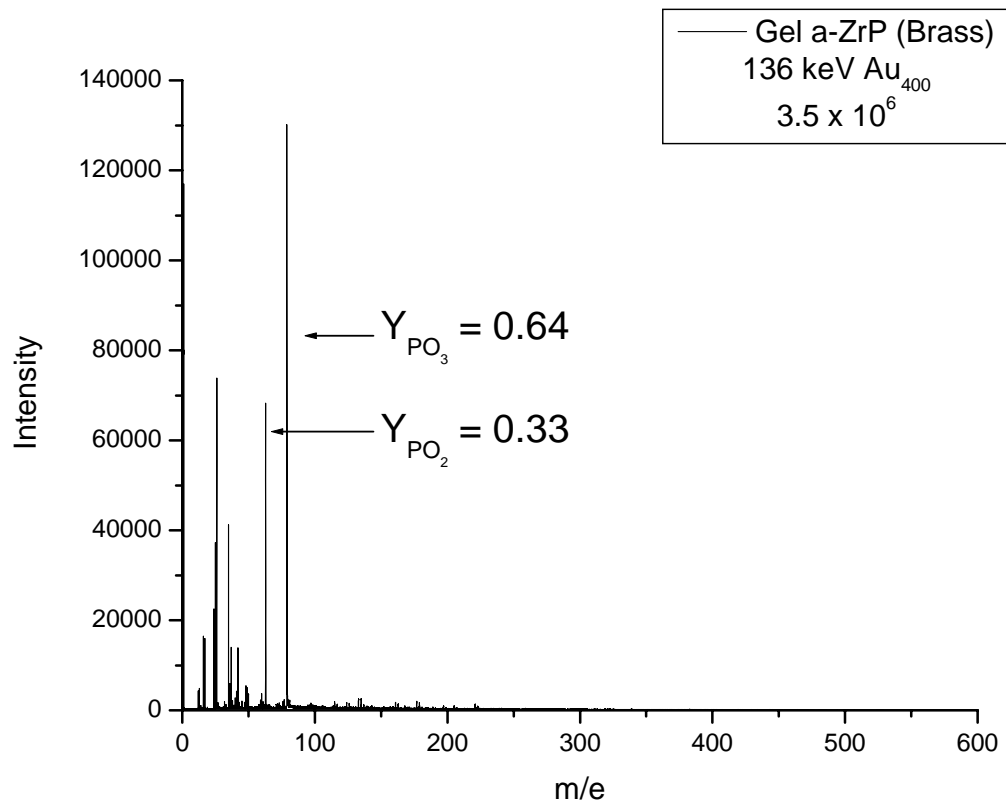


Figure 6-5. Negative secondary ion mass spectrum resulting from bombarding α ZrP gel with 136 keV Au₄₀₀. Secondary ion yields for PO₂ and PO₃ are 0.33 and 0.64 respectively.

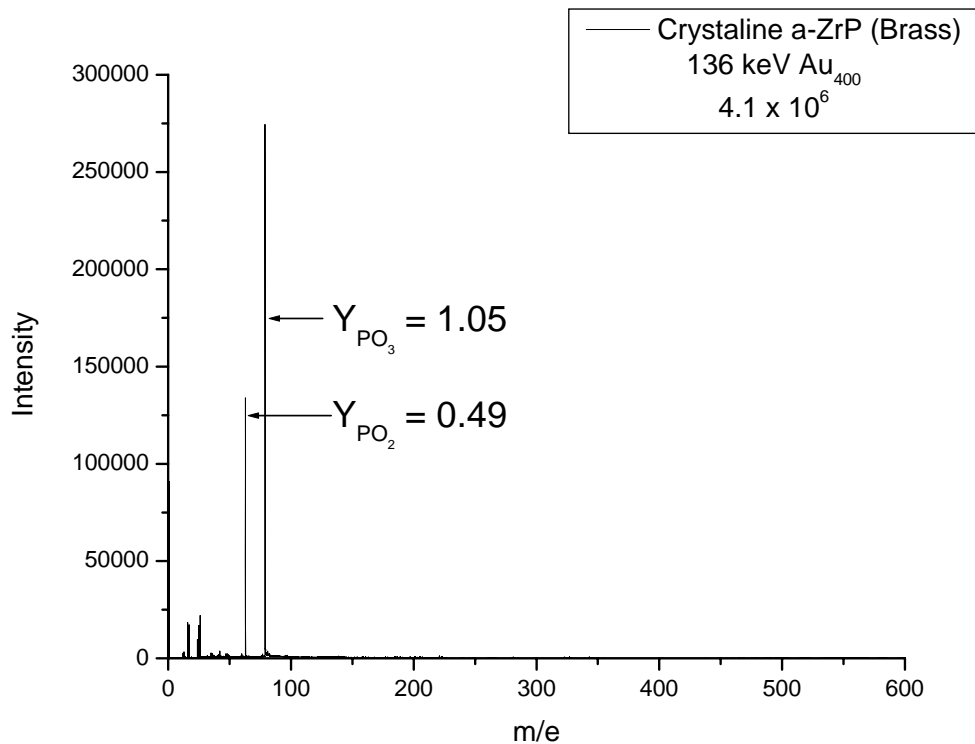


Figure 6-6. Negative secondary ion mass spectrum resulting from bombarding crystalline α ZrP with 136 keV Au₄₀₀. Secondary ion yields for PO₂ and PO₃ are 0.49 and 1.05 respectively.

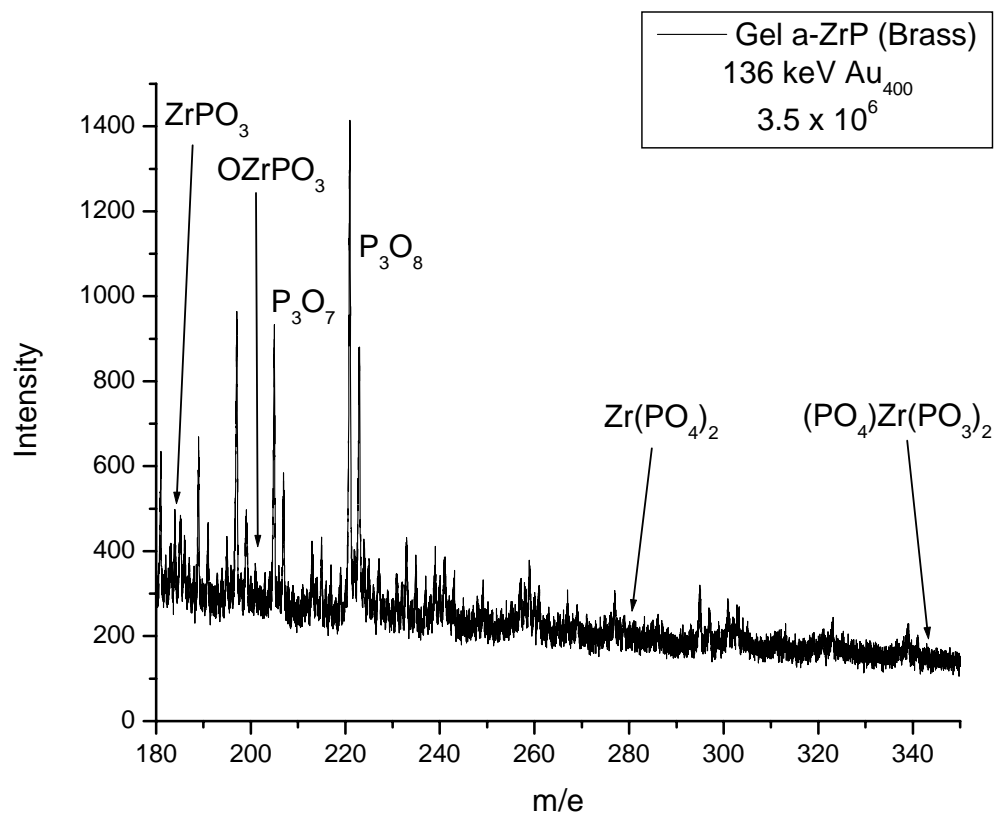


Figure 6-7. Negative secondary ion mass spectrum ($180 \leq m/e \leq 350$) resulting from bombarding α ZrP gel with 136 keV Au₄₀₀.

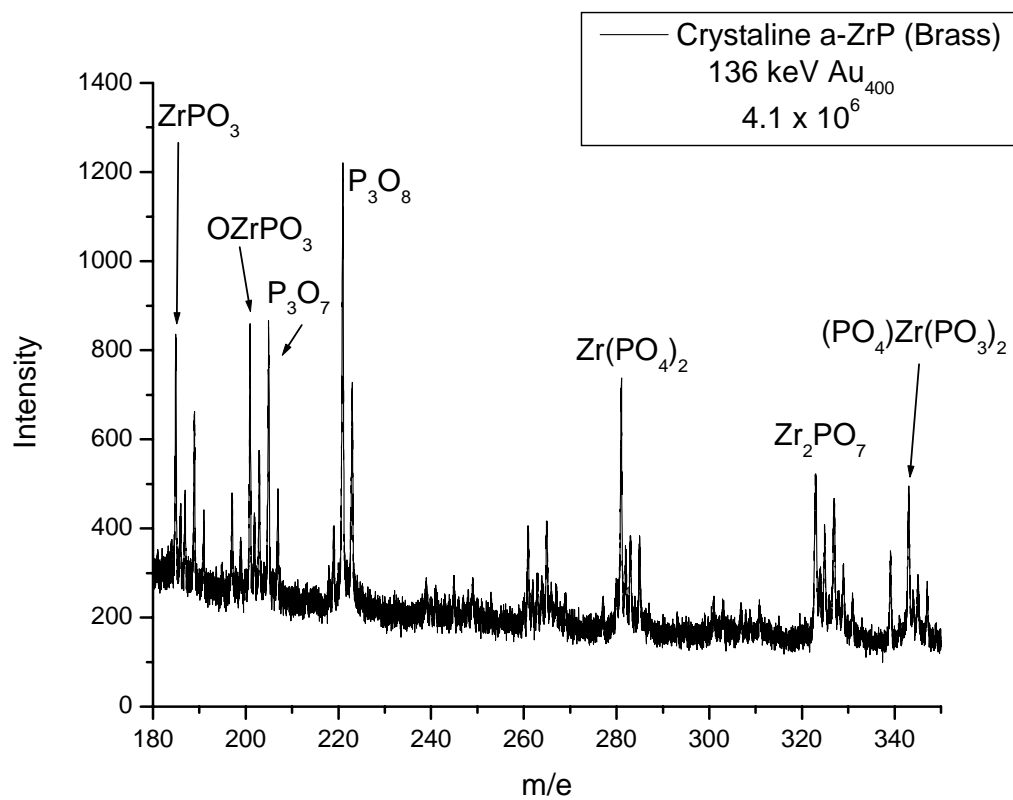


Figure 6-8. Negative secondary ion mass spectrum ($180 \leq m/e \leq 350$) resulting from bombarding crystalline α -ZrP with 136 keV Au₄₀₀.

the primary projectile of interest. They also noted that secondary ion emission is a direct representation of the target surface. The mass spectrum of the crystalline sample reveals higher mass secondary ions, which are representative of the crystalline array that exists near the surface. By comparison the amorphous sample shows none of these higher mass peaks. The higher mass secondary ions cannot be emitted from the amorphous sample because the surface is comprised of ZrP monomer which is not bonded to its neighboring ZrP molecules. Therefore, these higher mass species do not exist in the bulk. In addition, neither author found evidence of recombination of surface species, secondary ions which are not representative of the bulk of the sample.

Figures 6-5 and 6-6 are mass spectra of amorphous and crystalline α ZrP bombarded using Au₄₀₀ at 136 keV. Bombardment by massive clusters reveals secondary ion yield enhancements of 48% and 64% for PO₂ and PO₃ respectively for the crystalline sample versus the amorphous. This observation is a departure from what was observed in the previous two studies. One possible reason for this enhanced fragment ion yield is the well ordered structure of the crystalline α ZrP. This ordered structure orients the α ZrP in a manner that they are tightly bonded near one another. The combination of the substrate being tightly packed and the energy density of the Au₄₀₀ near the surface, when compared to MeV fission fragments and 27 keV Au₃, can explain the enhanced secondary ion yield for PO₂ and PO₃.

The absence of high mass secondary ions in the amorphous sample and their presence in the crystalline sample is observed under bombardment with massive clusters as seen in figures 6-7 and 6-8. The presence of Zr(PO₄)₂, PO₃ZrOZrPO₃, and

$\text{PO}_4\text{Zr}(\text{PO}_3)_2$ as secondary ions in the crystalline sample, and not in the amorphous, is further evidence that these species exist on the surface as part of the crystalline network and do not exist in the amorphous sample. These results are consistent with those obtained by Rickman and Van Stipdonk [103,104].

The presence of peaks $m/z = 205$ and 221 in both samples show a result not seen in the previous two studies. These peaks correspond to P_3O_7 and P_3O_8 and do not exist as part of the bulk sample. Therefore, they are a result of primary ion bombardment with Au_{400} at the aforementioned energy. The basic structure of αZrP is $-\text{O}-\text{P}(\text{O}_2)-\text{O}-\text{Zr}-\text{O}-\text{P}(\text{O}_2)-\text{O}-\text{Zr}-$. Each of the O in the PO_2 is also bonded to Zr, creating a crystalline network. Hence, P_3O_7 and P_3O_8 do not exist in the crystalline form. Similarly, the amorphous sample does not contain structures containing three atoms of phosphorous.

Recombination from target atoms into secondary ions which are not representative of the target has also been observed by Van Stipdonk examining NaBF_4 under MeV fission fragment bombardment [105]. The energy transfer from the primary ion impact into the surface creates a pressure and temperature spike which fragments/atomizes the analyte in and near the crater which facilitates recombination. Ions formed via recombination may not be representative of the target's original stoichiometry and retain no memory of the target's original structure. In comparison, secondary ions sputtered directly from the surface are representative of both the analyte's stoichiometry and structure.

CHAPTER VII

CONCLUSIONS

While there has been growing recognition in recent years that massive projectiles enhance the performance of SIMS, almost all efforts have centered on C_{60} . The present study shows that a still more massive “solid” nanoparticle as a projectile allows us to achieve further enhanced detection sensitivity, improved spatially resolved analysis and opens the possibility of structural characterization.

Early experiments with Au_{400} have shown the need for a secondary ion detection scheme that permits the detection of more than one isobaric secondary ion per event using pulse-counting electronics. We chose a multi-anode design where each anode would have equal surface area and would be symmetric around a center-point for an equal probability of secondary ion detection. The multi-anode assembly is an eight segmented design where all anodes have equal surface area and are arranged in a pie-wedge configuration around a null center-point. Au_{400} bombardment at 136 keV of a vapor-deposited CsI target result in a secondary ion yields of 3.42 and 2.60 for I^- and $(CsI)I^-$ respectively using the eight-anode assembly. This is an increase of 282% and 194%, respectively, in dynamic range for the multi-anode detector versus a single anode. The most probable event is one where 3 I^- are detected per event from a CsI target bombarded by 136 keV Au_{400} . Under the same conditions, detecting 2 $(CsI)I^-$ per event is most probable. The multi-anode detector also permits the investigation of secondary ion distributions over the detector array. The secondary ion distributions for selected

ions are shown for CsI and C₆₀ bombarded by 136 keV Au₄₀₀. The difference in the secondary ion distributions of specific m/z ions can yield insight to their desorption mechanism. However, such studies will require multi-anode detectors with more anodes in a smaller area to enhance the detection of isobaric ion emission.

Au-analyte adduct ions were observed, for the first time, in mass spectra of CsI, phenylalanine, histidine, and glycine. These adducts are not a result of accumulated gold in the target from continuous bombardment, but instead are a product resulting from the massive cluster that initiates that particular desorption event. The prompt in situ-emission of Au-adduct ions result from a single impact of a massive gold cluster which initiates the syntheses of Au-analyte adducts and their subsequent emission. Synthesis and emission are likely a two-step process. In the first step the primary ion impacts the surface and comes to rest in ~2 ps. At that stage, the Au residues have a great deal of vibrational energy and could act as a source of energy supporting adduct formation. The second step requires the emission of the Au-adducts from the surface. The fragments or molecules involved in Au-adduct synthesis must be localized in the close surrounding of the impact crater. One consequence of this observation would be that the volume of formation/emission of these adducts is smaller than the one involved in the emission of non-adduct secondary ions. We have shown that Au-adducts can be used to examine the homogeneity of surfaces down to the area of Au-adduct formation.

Structural differences between annealed oriented pyrolytic graphite and bulk graphite were examined using Au₄₀₀. Our data show that these two targets under bombardment of massive Au projectiles produce similar mass spectra. The major

difference between the two, is the secondary ion yield for carbon clusters are between 50 – 200% greater for the AOPG target versus the bulk graphite target. The enhanced secondary ion yield is a result of a “cluster-effect” brought about by the target. The secondary ion yield of Au^- , Au_2^- and Au_3^- are greater for the oriented target. This increase in Au_n^- yield may be attributed to the compression and subsequent relaxation of the graphite layers directly below the impact crater. The secondary ion emission of crystalline and amorphous αZrP under bombardment of Au_{400} was also studied. Intact secondary ion emission reveals structural information of αZrP . The emission of high mass secondary ions in the crystalline sample indicates their presence in the sample. The absence of these peaks in the amorphous sample is an indicator of the lack of an αZrP network. These results are consistent with previous studies. A notable deviation from the previous studies is the presence of secondary ions that are not representative of the sample’s stoichiometry. Secondary ions which are a product of recombination are composed from the target’s atoms, but have no memory of the target’s structure.

Au_{400} , within the energies described here, is an effective means to enhance both secondary ion yields and secondary ion multiplicities. For easily ionized targets such as CsI , the most probable desorption event will result in three analytically significant I^- being detected. While the secondary ion yield of $[\text{Phe-H}]^-$ is close to unity. The desorption volume, of a single ion impact, on average contains several thousand molecules, depending on molecule size and target density. Au_{400} , on average, desorbs one deprotonated molecule per $\sim 10^3$ phenylalanine molecules. To acquire a statistically

relevant spectrum, one may assume a secondary ion signal of ten counts is required for proper identification. How may this be achieved from a single massive cluster impact?

Clearly, the secondary ion detection scheme needs to be upgraded in a manner where the probability of detecting ten secondary ions of the same m/z per event is maximized. To accomplish this, the multi-anode detector needs to undergo three changes. First, the number of anodes needs to be increased so that more isobaric ions can be detected. To be 99% confident that all ten isobaric ions are detected, the number of anodes would need to be approximately six-times that number, ~60 separate anodes. As the confidence level decreases the required number of anodes decreases. If an 80% confidence level is sufficient, then only ~30 anodes would be needed. Next, the physical size of each anode should be reduced so that the probability of two ions striking the same anode is minimized. Lastly, the “dead” area between anodes needs to be minimized to decrease the probability of an ion going undetected. The combination of smaller anodes and “dead” area allows more individual anodes in the same area.

Increasing the energy of the primary ions is a likely way to enhance secondary ion yields. Extrapolating current secondary ion yield data, as a function of primary ion energy, indicates that raising the impact energy of Au_{400} by a factor of 5 should increase the secondary ion yield of $(\text{Phe-H})^-$ by a factor of 7, under current experimental conditions. In addition to increasing projectile energy, increasing projectile size may be an effective means to enhance secondary ion yields. The LMIS is capable of producing Au clusters with up to 1000 atoms. These projectiles have not been used in SIMS experiments but warrant further investigation.

Last but not least, as noted previously, post-source ionization is an effective method to enhance the secondary ion signal from neutrals desorbed from the surface. While lasers have been successfully employed, there are several other methods of ion formation which can be effective in enhancing secondary ion yield. One possible method for post-source ionization would be to bombard a surface with keV projectiles under atmospheric conditions and collect the ejecta with a nozzle-skimmer assembly, where they would be introduced into a vacuum system and ionized. The use of a differentially pumped nozzle-skimmer assembly would create a supersonic molecular beam (SMB) containing the desorbed analyte. Hyperthermal surface ionization (HSI) results when neutrals such as polyaromatic hydrocarbon and pharmaceuticals collide with a heated ReO surface. HSI has an ionization efficiency of near 0.10 for selected organics. As stated previously, secondary ion yields for phenylalanine are near unity. Therefore, only ~ 0.001 of the analyte in the desorption volume is ionized. Increasing the ionization efficiency to between 0.01 and 0.10 would increase the secondary ion count to between 10 and 100 per primary ion impact.

REFERENCES

- [1] F. Adams, L. Van Vaeck, R. Barrett, *Spectrochimica Acta Part B* 60 (2005) 13.
- [2] S. Chandra, D. R. Lorey, D. R. Smith, M. Miura, G. H. Morrison, SIMS XII Conference, Brussels, Belgium, September 5-10, 1999.
- [3] C. Rollion-Bard, M. Chaussidon, C. France-Lanord, E. Bard, SIMS XII Conference, Brussels, Belgium, September 5-10, 1999.
- [4] R. E. Peterson, B. J. Tyler, SIMS XII Conference, Brussels, Belgium, September 5-10, 1999.
- [5] A. P. Kovarsky, A. E. Nikolaev, M. A. Jagovkina, SIMS XII Conference, Brussels, Belgium, September 5-10, 1999.
- [6] R. D. English, M. J. Van Stipdonk, E. A. Schwekert, SIMS XII Conference, Brussels, Belgium, September 5-10, 1999.
- [7] D. Briggs, S. R. Bryan, SIMS XII Conference, Brussels, Belgium, September 5-10, 1999.
- [8] A. Benninghoven, F. G. Rudenauer, H. W. Werner, *Secondary Ion Mass Spectrometry – Basic Concepts, Instrumental Aspects, Applications and Trends*, John Wiley and Sons, New York, 1987.
- [9] R. D. Harris, Ph.D. Dissertation, Texas A&M University, College Station, 1998.
- [10] G. S. Hurst, M. G. Payne, *Resonance Ionization Spectroscopy*, Adam Hilger, Philadelphia, 1988.
- [11] C. H. Becker, K. T. Gillen, *Appl. Phys. Lett.* 45 (1984) 1063.
- [12] W. Szymczak and K. Wittmack, *Nucl. Instr. and Meth. in Phys. Res.* B88 (1994)149 .
- [13] M. G. Blain, S. Della-Negra, H. Joret, Y. Le Beyec, E. A. Schweikert, *Phys. Rev. Lett.* 63 (1989) 1625.
- [14] A. M. Kleinfeld, J. P. Kampf, C. Lechene, *J. Am. Soc. Mass. Spectrom.*,15 (2004) 1572.

- [15] R. Peteranderl, C. Lechene, *J. Am. Soc. Mass. Spectrom.* 15 (2004) 478.
- [16] P. Hallegot, R. Peteranderl, C. Lechene, *J. of Investigative Dermatology* 122 (2004) 381.
- [17] S. Parry, N. Winograd, *Anal. Chem.* 77 (2005) 7950.
- [18] S. G. Ostrowski, C. Szakal, J. Kozole, T. P. Roddy, J. Xu, A. G. Ewing, N. Winograd, *Anal. Chem.* 77 (2005) 6190.
- [19] A. G. Sostarecz, D. M. Cannon, C. M. McQuaw, S. Sun, A. G. Ewing, N. Winograd, *Langmuir* 20 (2004) 4926.
- [20] D. M. Cannon, S. G. Ostrowski, N. Winograd, A. G. Ewing, *Anal. Chem.* 74 (2002) 4020.
- [21] Z. Postawa, C. Bartlomiej, M. Szewczyk, E. J. Smiley, N. Winograd, B. J. Garrison, *Anal. Chem.* 75 (2003) 4402.
- [22] M. A. Park, K. A. Gibson, L. Quinones, E. A. Schweikert, *Science* 248 (1990) 988.
- [23] B. D. Cox, M. A. Park, R. G. Kaercher, E. A. Schweikert, *Anal. Chem.* 64 (1992) 843.
- [24] M. Benguerba, A. Brunelle, S. Della-Negra, J. Depauw, Y. Le Beyec, M. Blain, E. Schweikert, G. Assayag, G. Sudraud, *Nucl. Instr. and Meth. in Phys. Research, B62* (1991) 8.
- [25] R. D. Rickman, S. V. Verkhoturov, E. S. Parilis, E. A. Schweikert, *Phys. Rev. Lett.* 92 (2004) 047601-1.
- [26] M. J. Van Stipdonk, R. D. Harris, E. A. Schweikert, *Rapid Comm. Mass Spectrom.* 10 (1996) 1987.
- [27] A. Tempez, J. A. Schultz, S. Della-Negra, J. Depauw, D. Jacquet, A. Novikov, Y. Le Beyec, M. Pautrat, M. Caroff, M. Ugarov, H. Bensaoula, M. Gonin, K. Fuhrer, A. Woods, *Rapid Comm. Mass Spectrom.* 18 (2004) 371.
- [28] S. Bouneau, S. Della-Negra, D. Depauw, Y. Le Beyec, J. P. Mouffron, A. Novikov, M. Pautrat, *Nucl. Instr. and Meth. in Phys. Research, B 225* (2004) 579.

- [29] R. D. Rickman, S. V. Verkhoturov, G. J. Hager, E. A. Schweikert, *Int. J. Mass Spectrom.* 245 (2005) 48.
- [30] R. R. K. Herzog, F. Viehboeck, *Phys. Rev.* 76 (1949) 855.
- [31] A. Benninghoven, B. Hagenhoff, and E. Niehuis, *Anal. Chem.* 65 (1993) 630A.
- [32] N. Winnograd, *Anal. Chem.* 77 (2005) 142A.
- [33] R. Casting and G. Slodzian, *J. Microsc.* 1 (1962) 395.
- [34] C. J. Dedman, E. H. Roberts, S. T. Gibson, B. R. Lewis, *Rev. Sci. Instr.* 72 (2001) 2915.
- [35] S. V. Verkhoturov, E. A. Schweikert, N. M. Rizkalla, *Langmuir* 18 (2002) 8836.
- [36] P. Sigmund, *Phys. Rev.* 184 (1969) 383.
- [37] P. Sigmund, *Appl. Phys. Lett.* 25 (1974) 171.
- [38] H. H. Andersen and H. L. Bay, *J. Appl. Phys.* 45 (1974) 953.
- [39] H. H. Andersen and H. L. Bay, *J. Appl. Phys.* 46 (1975) 2416.
- [40] P. Sigmund, C. Claussen, *J. Appl. Phys.* 52 (1981) 990.
- [41] D. A. Thompson, S. S. Johar, *Appl. Phys. Lett.* 34 (1979) 342.
- [42] S. S. Johar, D. A. Thompson, *Surf. Sci.* 90 (1979) 319.
- [43] R. D. Rickman, Ph.D. Dissertation, Texas A&M University, College Station, 2004.
- [44] J. Eriksson, P. Demirev, P. Hakansson, M. Papaleo, B. U. R. Sundqvist, *Phys. Rev. B* 54 (1996) 1502554.
- [45] I. NoorBatcha, R. R. Lucchese, Y. J. Zeiri, *Chem. Phys.* 86 (1987) 5816.
- [46] R. R. Lucchese, *J. Chem. Phys.* 86 (1987) 443.
- [47] S. Bouneau, S. Della-Negra, D. Jacquet, Y. Le Beyec, M. Pautrat, M. H. Shapiro, T. A. Tombrello, *Phys. Rev. B* 71 (2005) 174110-1.
- [48] P. K. Rol, J. M. Fruit, J. Kistemaker, *Physica* 26 (1960) 1000.

- [49] F. Gronlund, W. J. Moore, *J. Chem. Phys.* 32 (1960) 1540.
- [50] A. D. Appelhans, J. E. Delmore, D. A. Dahl, *Anal. Chem.* 59 (1987) 1685.
- [51] A. D. Appelhans, J. E. Delmore, *Anal. Chem.* 61 (1989) 1087.
- [52] M. G. Blain, S. Della-Negra, H. Joret, Y. Le Beyec, E. A. Schweikert, *Physique* 50 (1989) 147.
- [53] W. Szmczak, K. Wittmaack, NATO ASI Series, Series B: Phys. 269 (1991) 123.
- [54] M. J. Van Stipdonk, R. D. Harris, E. A. Schweikert, *Rapid Comm. Mass Spectrom.* 10 (1996) 1987.
- [55] E. F. da Silveira, S. B. Duarte, E. A. Schweikert, *Surface Science* 408 (1998) 28.
- [56] R. A. Zubarev, I. S. Bitensky, P. A. Demirev, B. U. R. Sundqvist, *Nucl. Instr. and Methods in Phys. Res. B* 88 (1994) 143.
- [57] G. F. Knoll, *Radiation Detection and Measurement*, 2nd ed., John Wiley and Sons, New York, 1989.
- [58] M. A. Park, D. A. Gibson, L. Quinones, E. A. Schweikert, *Science* 248 (1990) 988.
- [59] J. H. Moore, C. C. Davis, M. A. Coplan, *Building Scientific Apparatus*, 2nd Ed., Perseus Books, Cambridge, MA, 1991.
- [60] A. Benninghoven, F. G. Rudenauer, H. W. Werner, *Secondary Ion Mass Spectrometry – Basic Concepts, Instrumental Aspects, Applications and Trends*, John Wiley and Sons, New York, 1987.
- [61] R. J. Cotter, *Time-of-Flight Mass Spectrometry*, ACS, Washington, DC, 1997.
- [62] I. S. Gilmore, M. P. Seah, *Int. J. Mass Spectrom.* 202 (2000) 217.
- [63] J. L. Wiza, *Nucl. Inst. and Meth.* 162 (1979) 587.
- [64] D. W. Koppenaal, C. J. Barinaga, M. B. Denton, R. P. Sperline, G. M. Hieftje, G. D. Schilling, F. J. Andrade, J. H. Barnes, *Anal. Chem.* 77 (2005) 418A.
- [65] R. D. Rickman, S. V. Verkhoturov, G. J. Hager, E. A. Schweikert, *Int. J. Mass Spectrom.* 245, (2005) 48.

- [66] R. D. Rickman, S. V. Verkhoturov, G. J. Hager, E. A. Schweikert, J. A. Bennett, *Int. J. Mass Spectrom.* 241 (2005) 57.
- [67] B. Deconihout, A. Bostel, M. Bouet, J. M. Sarrau, P. Bas, D. Blavette, *Appl. Surf. Sci.* 87/88 (1995) 428.
- [68] T. Chang, M. Zhao, W. Li, J. Wang, Q. Qian, *Int. J. Mass Spectrom.* 208 (2001) 113.
- [69] M. Gonin, V. Raznikov, K. Uhrer, J. A. Schultz, M. I. McCully, U.S. Pat. Appl. Publ. (2003) Application : 2001-25508 20011219.
- [70] D. C. Barbacci, D. H. Russell, J. A. Schultz, J. Holocek, S. Ulrich, W. Burton, M. J. Van Stipdonk, *J. Am. Soc. Mass Spectrom.* 9 (1998) 1328.
- [71] J. Mischler, N. Colombie, *Surf. Sci.* 40 (1973) 311.
- [72] S. Datz, C. Snoek, *Phys. Rev.* 134 (1964) A347.
- [73] H. Kerkow, M. Trapp, *Int. J. Mass Spectrom. and Ion Phys.* 13 (1974) 113.
- [74] A. G. J. De Wit, G. A. Van der Schootbrugge, J. M. Fluit, *Surf. Sci.* 47 (1975) 258.
- [75] J. Eriksson, P. Demirev, P. Hakansson, M. Papaleo, B. U. R. Sundqvist, *Phys. Rev. B* 54 (1996) 1502554.
- [76] Y. Lin, L. Smith, *Biomedical Mass Spec.* 5 (1978) 604.
- [77] K. Madhusudanan, B. Kumar, P. Tiwari, S. Madhusudan, A. Misra, *Rapid Comm. Mass Spec.* 19 (2005) 470.
- [78] J. Mathis, B. McCord, *Rapid Comm. Mass Spec.* 19 (2005) 99.
- [79] M. Ye, D. Guo, *Rapid Comm. Mass Spec.* 19 (2005) 818.
- [80] L. Adriaensen, F. Vangaever, J. Lenaerts, R. Gijbels, *Rapid Comm. Mass Spec.* 19 (2005) 1017.
- [81] T. Fujii, P. Selvin, M. Sablier, K. Iwase, *International Journal Mass Spec.* 209 (2001) 39.

- [82] K-H. Meiwes-Broer, *Metal Clusters at Surfaces: Structure, Quantum Properties*, Physical Chemistry, Springer-Verlag, New York, 2000.
- [83] H. H. Andersen, A. Brunelle, S. Della-Negra, S. J. Depauw, D. Jacquet Y. Le Beyec, J. Chaumont, J. H. Bernas, *Phys. Rev. Lett.* 80 (1998) 5433.
- [84] V. I. Shulga, P. Sigmund, *Nucl. Instrum. Methods Phys. Res. B* 62 (1991) 23.
- [85] T. Seki, T. Kaneko, D. Takeuchi, T. Aoki, J. Matsuo, Z. Insepov, I. Yamada, *Nucl. Instrum. Methods Phys. Res. B* 121 (1997) 498.
- [86] S.J. Carroll, P.D. Nellist, R.E. Palmer, S. Hobday, R. Smith, *Phys. Rev. Lett.* 84 (2000) 2654.
- [87] C. Anders, H. Urbassek, *Nucl. Instrum. Methods Phys. Res. Sec. B.* 228 (2005) 57.
- [88] S. Della-Negra, Private communication, Institut de Physique Nucleaire, Orsasy, (2006).
- [89] B. L. Holian, T. C. Germann, J. B. Maillet, C. T. White, *Phys. Rev. Lett.* 89 (2002) 285501/1.
- [90] D. Briggs, I. W. Fletcher, S. Reichlmaier, J. L. Agulo-Sanchez, R. D. Short, *Surf. Interface Anal.* 24 (1996) 419.
- [91] P. Brant, A. Karim, J. F. Douglas, F. S. Bates, *Macromolecules* 29 (1996) 5628.
- [92] Y. Lei, Z. Cheung, K. Ng, L. Li, L. Weng, C. Chan, *Polymer* 44 (2003) 3883.
- [93] L. Weng, T. L. Smith, J. Feng, C. Chan, *Macromolecules* 31 (1998) 928.
- [94] H. E. Smith, G. H. Morrison, D. T. Hodul, *Nucl. Instr. and Methods in Phys. Res. B* 21 (1987) 503.
- [95] M. V. Kosevich, O. A. Boryak, V. S. Shelkovsky, V. V. Orlov, *Low Temp. Phys.* 29 (2003) 805.
- [96] O. L. Blakslee, D. G. Proctor, E. J. Seldin, G. B. Spence, T. Weng, *J. Appl. Phys.* 41 (1970) 3373.
- [97] H. H. Andersen, H. L. Bay, *J. Appl. Phys.* 45 (1974) 953.
- [98] J. F. Ziegler, *Particle Interactions With Matter*, 2003 <http://www.srim.org/>.

- [99] V. I. Shulga, P. Sigmund, Nucl. Instr. and Meth B 47 (1990) 236.
- [100] V. I. Shulga, M. Vicanek, P. Sigmund, Phys. Rev. A 39 (1989) 3360.
- [101] Z. Pan, Nucl. Instr. and Meth B 66 (1992) 325.
- [102] M. Van Stipdonk, M. A. Park, E. A. Schweikert, P. Sylvester, A. Clearfield, Int. J. Mass Spectrom. Ion Processes 128 (1993) 133.
- [103] M. J. Van Stipdonk, Ph.D. Dissertation, Texas A&M University, College Station, 1994.
- [104] R. D. Rickman, S. V. Verkhoturov, S. Balderas, N. Bestaoui, A. Clearfield, E. A. Schweikert, Appl. Surf. Sci. 231-232 (2004) 106.
- [105] M. J. Van Stipdonk, V. Santiago, E. A. Schweikert, J. Mass Spectrom. 34 (1994) 554.

VITA

George Joseph Hager was born in Lancaster, Pennsylvania. He is the son of Ilene and James Bartlett. He graduated from Ephrata High School in Ephrata, Pennsylvania in June of 1985. Upon graduation he enlisted in the United States Navy and attained the rank of Petty Officer Second Class prior to being Honorably Discharged in 1992. He served as a maintenance technician from 1993 to 2000 while concurrently attending Millersville University where he earned his B.S. in chemistry. In August 2000 he enrolled in Texas A&M University to pursue a Ph.D. degree in analytical chemistry under the direction of Dr. Emile A. Schweikert and received his Ph.D. in May 2007.

His permanent address is that of his parents:

George Joseph Hager
c/o Ilene V. Bartlett
220 Jennifer Lane
Ephrata, PA 17522